GA–A23922

ITER-FEAT PHYSICS STUDY — ADVANCED TOKAMAK (AT) OPERATION CY01 IR&D PROJECT

by
V.S. CHAN, M.S. CHU, T.E. EVANS, D.A. HUMPHREYS, L.L. LAO, J.A. LEUER, T.E. PETRIE, G.M. STAEBLER, P.B. SNYDER, H.E. ST JOHN, and A.D. TURNBULL

MARCH 2002

GA–A23922

ITER-FEAT PHYSICS STUDY — ADVANCED TOKAMAK (AT) OPERATION CY01 IR&D PROJECT

by
V.S. CHAN, M.S. CHU, T.E. EVANS, D.A. HUMPHREYS, L.L. LAO, J.A. LEUER, T.E. PETRIE, G.M. STAEBLER, P.B. SNYDER, H.E. ST JOHN, and A.D. TURNBULL

GENERAL ATOMICS PROJECT 40010
MARCH 2002

TABLE OF CONTENTS

TABLE OF CONTENTS (Continued)

LIST OF FIGURES

LIST OF FIGURES (Continued)

LIST OF FIGURES (Continued)

LIST OF TABLES

1. SUMMARY

This study is a continuation of the CY00 study (GA-D23609) in which we carried out a physics evaluation of the ITER-FEAT reference design. The work reported here focused on evaluation of the ITER-FEAT advanced tokamak (AT) performance capabilities. Our strategy was to use the published ITER-FEAT magnet system constraints to explore AT equilibria using plasma profiles that were consistent with information from DIII-D. The stability, transport and heat handling properties of these equilibria were studied, and external control requirements to achieve optimum performance were quantified. Key findings in each area are summarized in this chapter and expounded in more details in subsequent chapters.

To perform the proposed physics validation, several AT plasma equilibrium configurations have been established for ITER-FEAT. The first equilibrium is based on the reference AT current profile, shape and plasma parameters specified by the ITER project. Additional equilibria were established based on scaling of internal profiles from DIII-D AT discharges. Several additional equilibria were established with increased upper triangularity. All equilibria can readily be produced using the ITER coil set. These equilbria were analyzed for vertical, ideal low n kink, peeling and ballooning mode, and resistive wall mode (RWM) stability.

The AT equilibrium developed for the ITER-FEAT configuration with pedestal profiles taken to be consistent with DIII-D experience has been analyzed for vertical stability growth rate and disruption halo currents. The growth rate for this case was found to be 4.5 rad/s, and the peak axisymmetric halo current amplitude which results from an unmitigated VDE (with post-thermal quench T_e = 18 eV and Z_{eff} = 1.0) was calculated to be 1.3 MA (corresponding to stress of about 0.18 MPa). When mitigated by an Ar gas puff, this configuration produces a peak halo current of 0.53 MA (corresponding to stress of about 0.07 MPa). For comparison, the growth rate for the reference ITER-FEAT equilibrium was calculated to be 6.2 rad/s. The peak axisymmetric halo current amplitude which results from an unmitigated VDE in the reference case (with post-thermal quench T_e = 20 eV and Z_{eff} = 1.0, values typical of DIII-D) was calculated to be 3.5 MA (corresponding to stress of about 0.47 MPa). When mitigated by an Ar gas puff, this configuration produces a peak halo current of 1.2 MA (corresponding to stress of about 0.16 MPa). A rough calculation based on disruption force loads reportedly expected by the ITER-FEAT design team suggests that 0.1 MPa is the corresponding peak stress level expected (and presumably designed for). The fact that this value is comparable to the

values found in *mitigated* scenarios in the present study suggests that reliable mitigation may be very important in ITER-FEAT.

Stability calculations were performed using the GATO code for the n=1, n=2 and n=3 ideal kink modes for the three AT equilibria with the H-mode pedestal and increasing triangularity. For the n=1 mode, all three equilibria were unstable without a wall but stabilized by the ITER-FEAT wall. The n=2 and n=3 modes also showed stability with the ITER-FEAT wall for all three triangularity values. This result suggests that feedback control of RWMs may be key for ITER-FEAT AT operation.

An equilibrium approximating one of the ITER-FEAT AT target equilibria produced for this study has been tested for its stability to the RWM and stabilization of the RWM by plasma rotation. It is found that a central rotation rate of 1% of the Alfvén rotation frequency is sufficient to stabilize the RWM. This rate is about a factor of 5 smaller than other equilibria proposed for the ITER-FEAT reference design and the ARIES-AT series. This could be traced to the behavior of the peaking of the displacement eigenfunction towards the plasma center and the presence of multiple singular surfaces in the equilibrium. Using a rotation profile scaled up from DIII-D to an ITER-FEAT AT equilibrium, it was found that 33 MW of negative ion (1 MeV) neutral beam injection is sufficient to maintain the central toroidal rotation speed at 2×10^4 rad/s using ion power balance diffusivity for the momentum diffusivity. The required central rotation speed for RWM stability according to MARS calculation is about 1×10^4 rad/s.

The stability to n=6–30 magnetohydrodynamic (MHD) modes, for three AT equilibria with different values of triangularity, were evaluated with the ELITE code. These modes are believe to place constraints on the achievable pedestal height, as well as driving edge localized modes (ELMs) which impose heat load constraints on the divertor. At the lowest value of $\delta = 0.375$, edged localized MHD modes were found to be unstable with significant growth rates. Increasing d was found to significantly stabilize these modes and thus allow higher stable pedestals.

We note that the stability limit on the edge pedestal temperature can be increased by decreasing the edge density, but this involves tradeoffs with divertor design and may impact overall performance if the core density is reduced as well. Hence, it is important to examine the compatibility of the AT equilbria with the divertor heat handling capability. We found that for the standard ITER-FEAT AT equilibria (with a pedestal edge current), the peak particle heat flux at the top of the vessel was ≤ 0.1 MW/m^2 and the total power flowing to the top of the vessel ≤ 1 MW. At an intermediate upper triangularity ($\delta_{UP,95} \approx 0.4$), roughly midway between standard $\delta_{UP,95}$ and estimated highest $\delta_{UP,95}$ for ITER-FEAT AT, power loading at the top of the vessel is still modest. These values can probably be handled without much engineering difficulty. However, at

the highest triangularity case ($\delta_{UP,SEP} \approx 0.55$), the peak heat flux (and power loading) is much more problematical.

Finally, motivated by recent gyrokinetic simulation results, which showed a significantly lower level of ion thermal transport than previous gyrofluid simulations, the GLF23 transport model was renormalized to get a better fit with data consistent with the gyrokinetic prediction. The ITER-FEAT reference design fusion performance was re-evaluated using this renormalized transport model. The pedestal temperature required to reach the 400 MW fusion power target was reduced by about 0.5 keV. The maximum fusion power obtained by optimizing the fueling level and evolving the density profile with GLF23 was investigated, keeping the pedestal density fixed. Too much fueling would lead to a temperature collapse. Allowing the density profile to peak reduces the pedestal temperature required to get to the 400 MW fusion power target even further. This result suggests that some means to control the particle transport and fuel the plasma core would be beneficial for ITER-FEAT.

2. ITER-FEAT AT EQUILIBRIA AND 0-D ANALYSIS

2.1. OVERVIEW

This report extends the previous study [1,2] designed to quantify the capabilities of the downsized ITER device (ITER-FEAT) [3]. In particular, the previous report explored the reference ITER-FEAT plasma configuration, while the present study focuses on Advanced Tokamak (AT) configurations associated with shapes and current profiles expected when running the ITER plasma in a weak reverse shear (WRS) configuration and with high non-inductive current drive. Figure 1 shows the difference between the Reference ITER plasma shape and the proposed ITER-WRS-AT configuration. Several different equilibria were studied. The first equilibrium uses Caltrans standard pedestal profile parameterization and was optimized to match plasma parameters as established by the ITER project for a "WRS-AT" discharge [4]. This is considered the Reference ITER AT configuration. The second and third equilibria use the same approximate shape of the reference AT plasma but scale the internal current density profile based on typical DIII-D WRS AT discharges. Specifically, DIII-D discharges 98549 and 106795, with $\beta_N H_{89} > 9$, are used as representative of DIII-D high performance AT discharges. The last discharge (106795), has a pronounced edge pedestal pressure profile and some of the highest AT performance parameters achieved for sustained periods in DIII-D. Finally, two additional equilibria are presented which use the DIII-D Shot 106795 profile parameterization but with an increase in the upper triangularity. These latter equilibria are being used in stability and divertor studies. The equilibria are studied using 0-D ITER scaling rules to predict ignition.

Section 2 presents the ITER reference WRS-AT configuration, Section 3 presents the configuration based on DIII-D shot 98549 AT profile. Section 4 presents the configuration based on DIII-D shot 106795 AT profile. Section 5 compares profiles between the different equilibria. Table I compares the plasma parameters for the three cases along with the Nominal ITER-FEAT equilibrium established earlier. Section 6 describes equilibria with increased upper triangularity. Section 7 shows the 0-D performance of the equilibria; Table II summarizes the results. Section 8 identifies some of the study limitations and Section 9 provides information on the project and file structure.

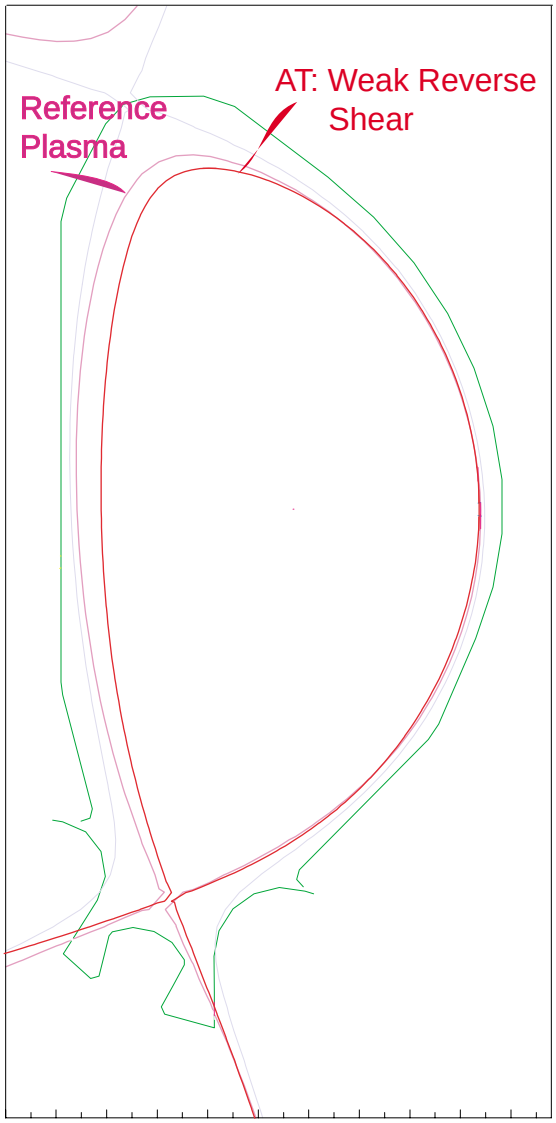

Fig. 1. Shape comparisons between the Reference ITER-FEAT plasma [3] and the WRS-AT plasma as defined by Scenario 4 from Gribov [4].

2.2. ITER-WRS-AT REFERENCE EQUILIBRIUM (ITER Scenario 4)

The ITER project has investigated several AT configurations [3]. The most advanced WRS AT configuration is Scenario 4 [4]. The main plasma parameters are shown in Column B of Table I. The Caltrans code was used to produce an equilibrium to approximately match the Scenario 4 parameters transmitted by Gribov. In particular, we used the “bump” profile parameterization in Caltrans to provide an edge pedestal in the current profile. This is a different pedestal profile parameterization than that used by Gribov [4] and, accordingly, the profile parameters were varied to obtain the best match to the Gribov reported plasma shape and major plasma parameters, internal inductance

(ℓ_i) and normalized beta (β_N). Column C shows a Caltrans equilibrium (wrs10a). For comparison, Column A of the table shows ITER-FEAT reference equilibrium parameters reported by Campbell with additional parameters added based on a Caltrans equilibrium [1].

TABLE I
COMPARISON OF ITER PLASMA PARAMETERS
REFERENCE AND AT WRS CONFIGURATIONS

	A	B	C	D	E
Reference	Campbell*	Gribov+.	Corsica	Corsica	Corsica
Case	FEAT Ref.	Scenario 4	Scenario 4	DIII-D 98549 $\beta_N H \sim 9$	DIII-D 106795 $\beta_N H \sim 12$
ID			wrs10a	Pedestal 2	DIII-D 106795
I_p (MA)	15	10	10	10	10
B_o (T)	5..3	5.3	5.3	5.3	5.3
R (m)	6.2	6.35	6.33	6.33	6.35
a (m)	2.0	1.85	1.87	1.87	1.86
κ_{95}	1.7	1.83	1.81	1.85	1.84
δ_{95}	0.33	0.40	0.36	0.40	0.49
κ_x	1.85	1.95	1.93	1.96	1.94
δ_x	0.49	0.56	0.62	0.66	0.66
R/a	3.1	3.43	3.39	3.39	3.41
I*B/R (MA T/m)	12.8	8.35	8.37	8.37	8.36
q_0	1.12	2.40	2.40	3.22	2.19
q_{min}	1.12	–	1.94	2.16	1.60
q_{95}	3.0	4.45	4.29	4.57	4.66
ℓ_i (3)	0.847	0.67	0.67	0.546	0.56
β_p (Vol)	0.65	1.80	1.75	1.80	1.90
β_N	1.8	3.19	3.19	3.19	3.43
β (T)	2.5	3.33	3.29	3.30	3.58

*From Campbell's 2000 APS talk [3]; black from Corsica Run [1].
+Reference 4.

TABLE II
ITER PERFORMANCE BASED ON 0-D ITER SCALING RULES

	A	**A1**	**B–C**	**D**	**E**
Reference	Campbell*	TokSim	TokSim	TokSim	TokSim
Profile source	FEAT Ref.	FEAT Ref. Simulated	ITER-AT Gribov	DIII-D 98549	DIII-D 106795
I_p (MA)	15	15	10	10	10
B_o (T)	5..3	5.3	5.3	5.3	5.3
R (m)	6.2	6.2	6.35	6.33	6.35
a (m)	2.0	2.0	1.85	1.87	1.86
κ_{95}	1.7	1.7	1.83	1.85	1.84
δ_{95}	0.33	0.33	0.40	0.40	0.49
R/a	3.1	3.11	3.43	3.39	3.41
I*B/R (MA T/m)	12.8	12.8	8.35	8.38	8.35
q_{95}	3.0	2.85	4.23	4.41	4.58
Troyon C		2.5	3.19	3.19	3.43
β_N	1.8	1.73	3.19	3.19	3.43
H-factor	2.0	2.0	2.82	2.82	3.5
$\beta_N H$	3.6	3.45	9.0	9.0	12.0
Z_{eff}	1.69	1.69	1.69	1.69	1.69
Volume (m^3)	828	828	785	808	798
P_{aux_0} (MW)	40	40.6	47	53	41
n_{20} ($10^{20}/m^3$)	1..01	0.86	0.79	0.77	0.67
T (keV)	8.8	10.9	15.8	16.0	19.8
P (MP)	0.28	0.27	0.36	0.36	0.39
τ (s)	3.6+	2.72	2.23	2.20	3.08
n τT ($10^{20}/m^3$skeV)	32.0	24.5	27.7	27.1	41.0
β (%)	2.5	2.44	3.25	3.22	3.48
n/n_{max} (%)	85	85	100	100	86
β/β_{max} (%)	72	69	100	100	100
Fusion power (MW)	400	448	735	736	762
Q_{wall} (MW/m^2)	0.47	0.56	0.94	0.93	0.97
Q	10.0	11.0	15.7	14.0	∞

*From Campbell's 2000 APS talk [3].
+Interpolated from plot in [3].

Figure 2 shows the overall equilibrium shape and parameters from the Caltrans output. As with most WRS plasmas, the plasma current is lower than the reference scenario value and leads to higher q operation of the device. This, and the edge pedestal in the current profile, leads to a much higher poloidal beta (β_p) and ultimately a higher value of normalized beta $\beta_N \sim 3.2$. Figure 3 shows the plasma shape relative to the shape specified by Gribov for Scenario 4 (+'s). Figure 4 shows the current profile variation with minor radius. For this case all pressure profile parameters (FF' and P') are zero at the edge (no edge current). This is consistent with the shape parameterization used by the ITER project.

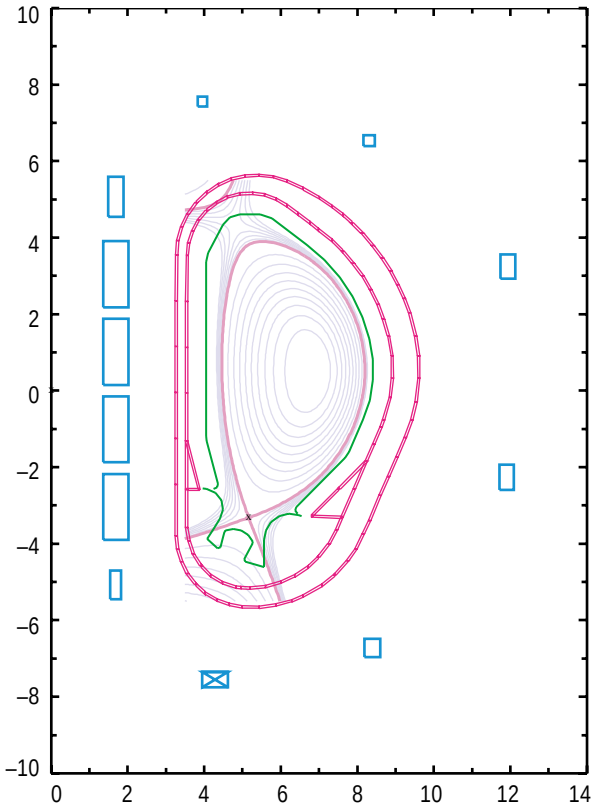

I_p, B_0, @ R	10.000	5.300	6.200
R_0, α, A	6.331	1.871	3.384
β_ϕ, β_N, β^*	3.288	3.191	4.461
$\beta_{p1,2,3}$	1.750	1.295	1.389
$l_{i1,2,3}$	.846	.625	.670
q_0, q_{95}, q^*	2.395	4.291	3.061
q_{min}, ρ_{qmin}	1.941	.492	
κ_{95}, κ_x	1.809	1.929	
δ_{95}, δ (U)	.344	.426	
δ_{95}, δ_x (L)	.379	.623	
$\Delta_{sep_{i,o}}$, ζ	.000	.000	–.001
R,Z_{axis}, ΔR	6.793	.517	.461
R,Z_{top}	5.533	3.899	
R,Z, ψ_{xpt} (L)	5.165	–3.320	–64.245
R,Z, Δl_{spt}	4.217	–3.647	1.003
R,Z, Δl_{spt}	5.565	–4.357	1.111
$\psi_{ext_{1,2,3}}$	–160.00	–165.82	–156.40
$L_{p_{n,a}}$ [μH], h_i	12.241	11.707	1.099
ψ_0, $\Delta\psi_p$, Φ	–20.510	–43.735	2.518
$W_{tot,\ c}$ [GJ]	6.355	7.343	3
alfa,betp (0)	4.911	1.000	3 0
epf, npf	.130	–3.500	
alfa,betp (1)	2.590	1.000	3
epp, npp	.100	–3.500	
betaj, β_{ps3}	2.036	1.366	
R,$Z_{Jcentroid}$	6.544	.493	
Vol., Sect.	784.255	20.265	

	PF1	PF2	PF3	PF4	PF5	PF6
NI_{coil} =	–1.331	–1.718	–4.935	–4.984	–3.972	5.410
	CS3L	**CS2L**	**CS1L**	**CS1U**	**CS2U**	**CS3U**
NI_{coil} =	–4.250	–22.456	–22.456	–22.456	–22.456	–8.286

Fig. 2. ITER-WRS-AT reference equilibrium (Caltrans) based on current profile, plasma shape and parameters for Scenario 4 from Gribov [4].

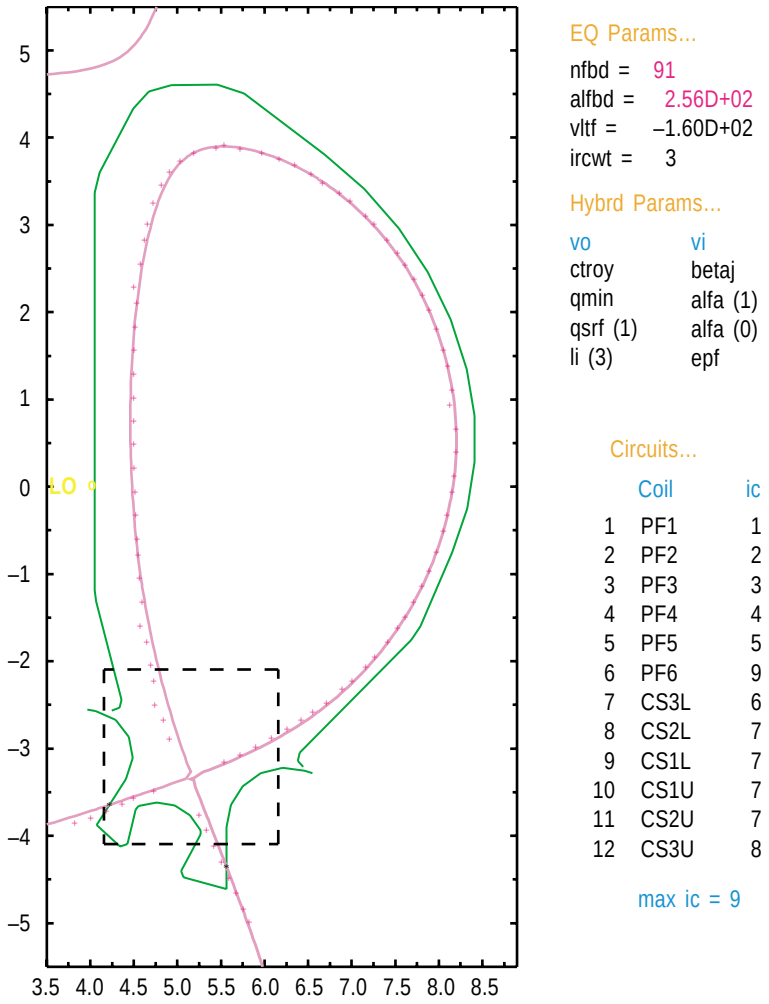

Fig. 3. ITER-WRS-AT Reference seperatrix location relative to the plasma shape (+'s) specified by Gribov [4] . The first wall boundary is shown in green.

2.3. ITER-AT-DIII-D EQUILIBRIUM (98549) BROAD EDGE PROFILE, FINITE EDGE CURRENT

DIII-D WRS-AT discharges typically have an edge pressure profile and finite edge current density [5]. These optimized discharges have shown high plasma performance (as defined by $\beta_N H_{89} \sim 9$) and non-inductive current drive of order 75%. In this section we take the internal profiles from one of DIII-D high performance AT discharge (98549) and scale it for use in the ITER device. Figure 5 shows the DIII-D EFIT equilibrium used in this analysis. The current profile parameters were extracted from this equilibrium and scaled using toroidal field for the *F* profile and normalized beta for the *P* profile:

Toroidal (*F*): $R \cdot B_\theta = \text{constant}$

Pressure (*P*: $R \cdot \beta_N = \text{constant} \Rightarrow I_p \cdot B_\theta/a = \text{constant}$.

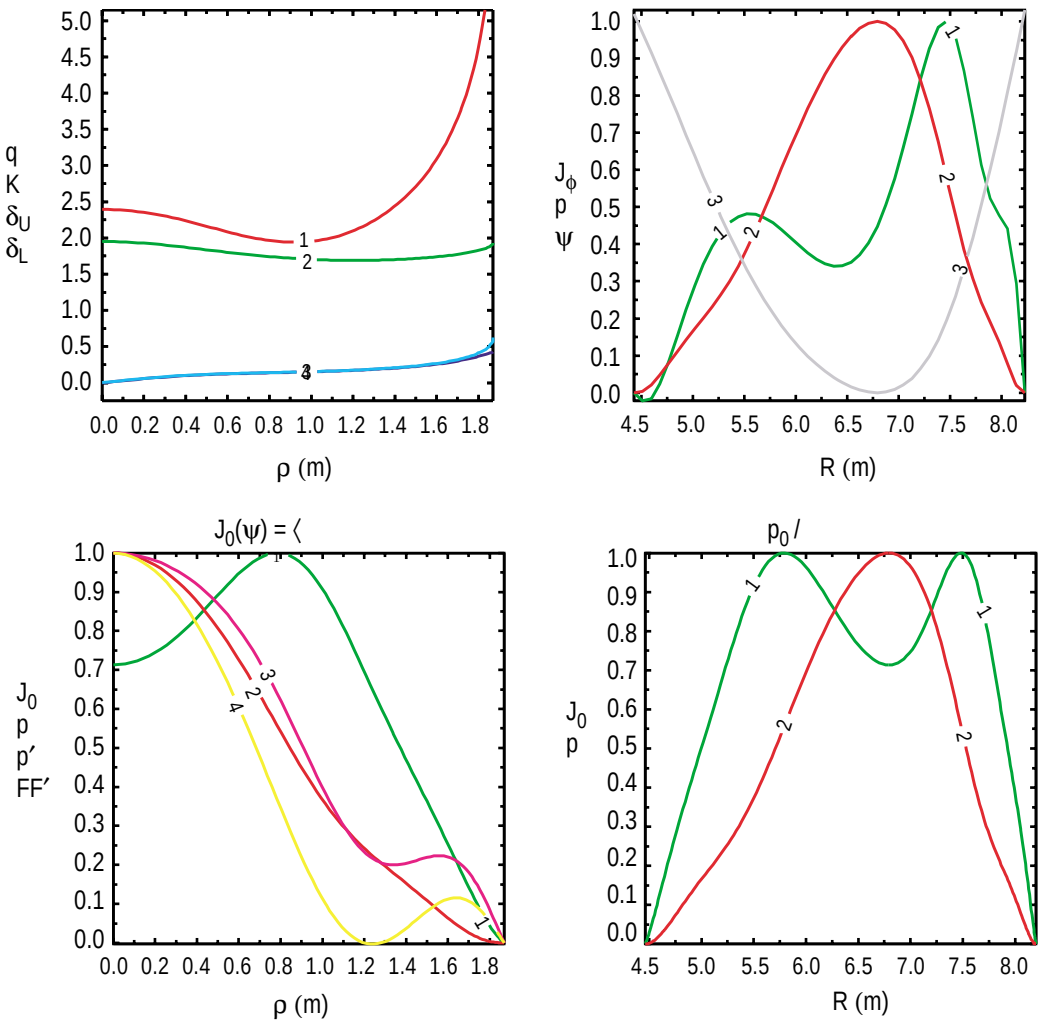

Fig. 4. ITER-WRS-AT Reference profile variation with minor radius from Corsica. Curve numbering corresponds to the symbol order shown in the Y-axis labels.

Figure 6 shows the overall equilibrium shape and parameters from the Caltrans output for ITER operating on the DIII-D optimized AT profiles from shot 98549. Column D of Table I summarize the parameters. Only a small difference is seen in most plasma parameters between the ITER-WRS-AT plasma (Column C) and the WRS-DIII-D profiles (Column D). The major difference is in the q parameters, with q from the DIII-D parameterization higher than the ITER-WRS-AT plasma. Figure 7 shows the plasma shape relative to the shape (+'s) specified by Gribov for Scenario 4. Figure 8 shows the current profile variation with minor radius. For this case, all pressure profile parameters (FF' and P') have finite value at the edge. This is the main difference between the ITER-WRS-AT design and the ITER-AT-DIII-D (98549) design.

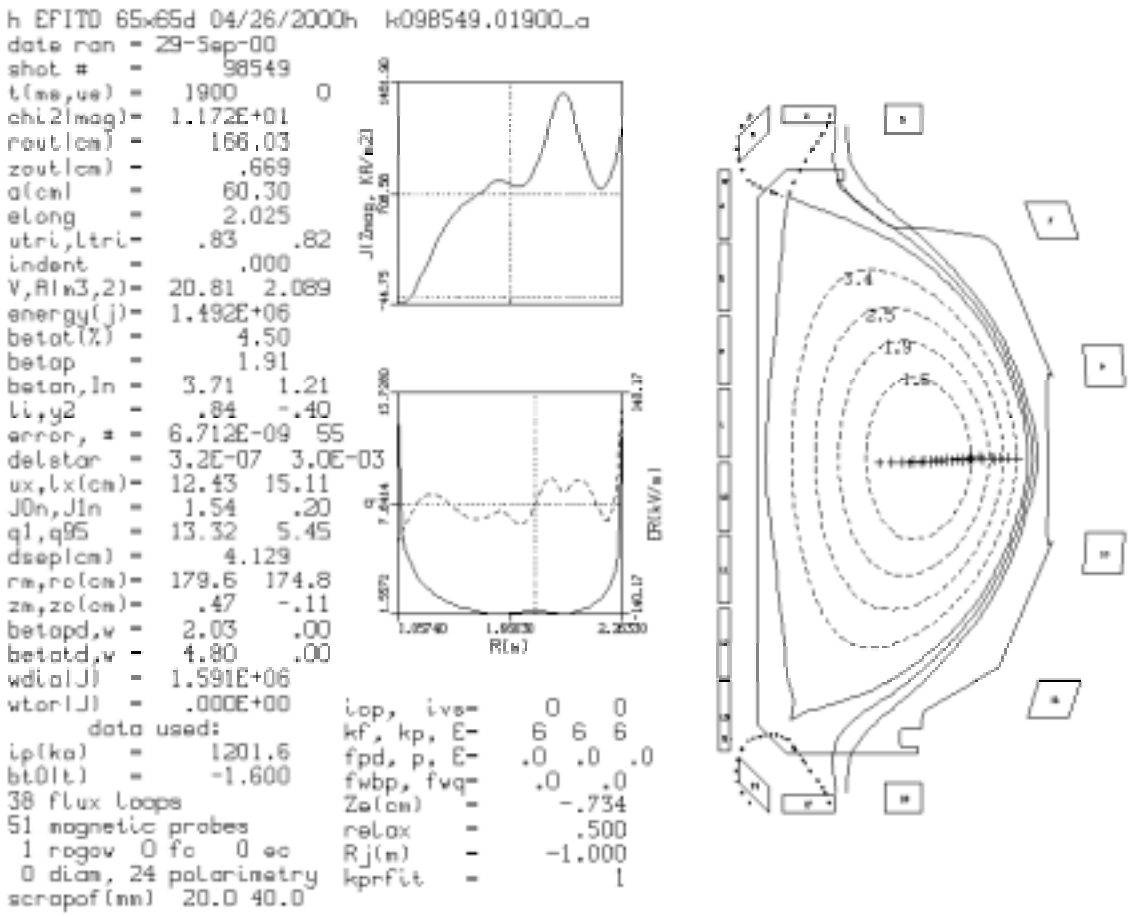

Fig. 5. High Performance DIII-D AT equilibrium from EFIT (98549), ($\beta_N H_{89} \sim 9$).

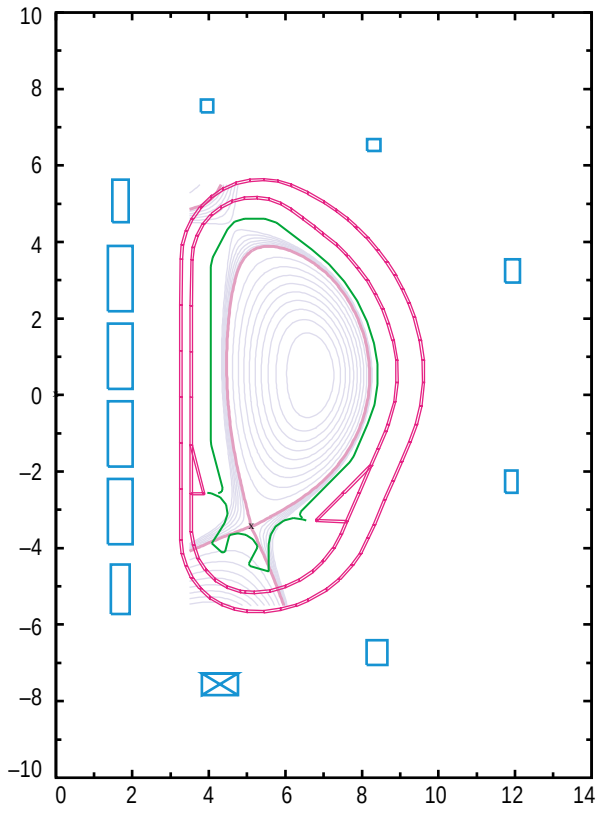

I_p, B_o, @ R	10.000	5.300	6.200
R_o, α, A	6.334	1.868	3.391
β_ϕ, β_N, β*	3.298	3.193	3.923
$\beta_{p1,2,3}$	1.804	1.307	1.392
$l_{i1,2,3}$	.706	.513	.546
q_0, q_{95}, q*	3.215	4.572	3.142
q_{min}, ρ_{qmin}	2.160	.448	
k_{95}, k_x	1.846	1.960	
δ_{95}, δ (U)	.361	.413	
δ_{95}, δ_x (L)	.448	.655	
$\Delta_{sep_{i,o}}$, ζ	.000	.000	.004
R,Z_{axis}, ΔR	6.747	.517	.411
R,Z_{top}	5.564	3.887	
R,Z, ψ_{xpt} (L)	5.111	–3.437	–67.107
R,Z, Δl_{spt}	4.107	–3.820	1.074
R,Z, Δl_{spt}	5.565	–4.483	1.141
$\psi_{ext_{1,2,3}}$	–160.00	–165.81	–157.77
$L_{p_{n,a}}$ [μH], h_i	11.463	11.142	.981
ψ_0, $\Delta\psi_p$, Φ	–28.042	–39.065	2.824
$W_{tot,\ c}$ [GJ]	7.143	8.170	3
alfa,betp (0)	4.911	1.000	999 0
epf, npf	.130	–3.500	
alfa,betp (1)	2.590	1.000	999
epp, npp	.100	–3.500	
betaj, β_{ps3}	.975	1.388	
R,$Z_{Jcentroid}$	6.511	.472	
Vol., Sect.	784.859	20.288	

	PF1	PF2	PF3	PF4	PF5	PF6
NI_{coil} =	–2.199	–2.144	–4.758	–3.789	–7.042	10.542
	CS3L	**CS2L**	**CS1L**	**CS1U**	**CS2U**	**CS3U**
NI_{coil} =	–12.680	–22.206	–22.206	–22.206	–22.206	–9.326

Fig. 6. ITER-AT WRS Corsica equilibrium based on DIII-D AT current density profile from Shot 98549.

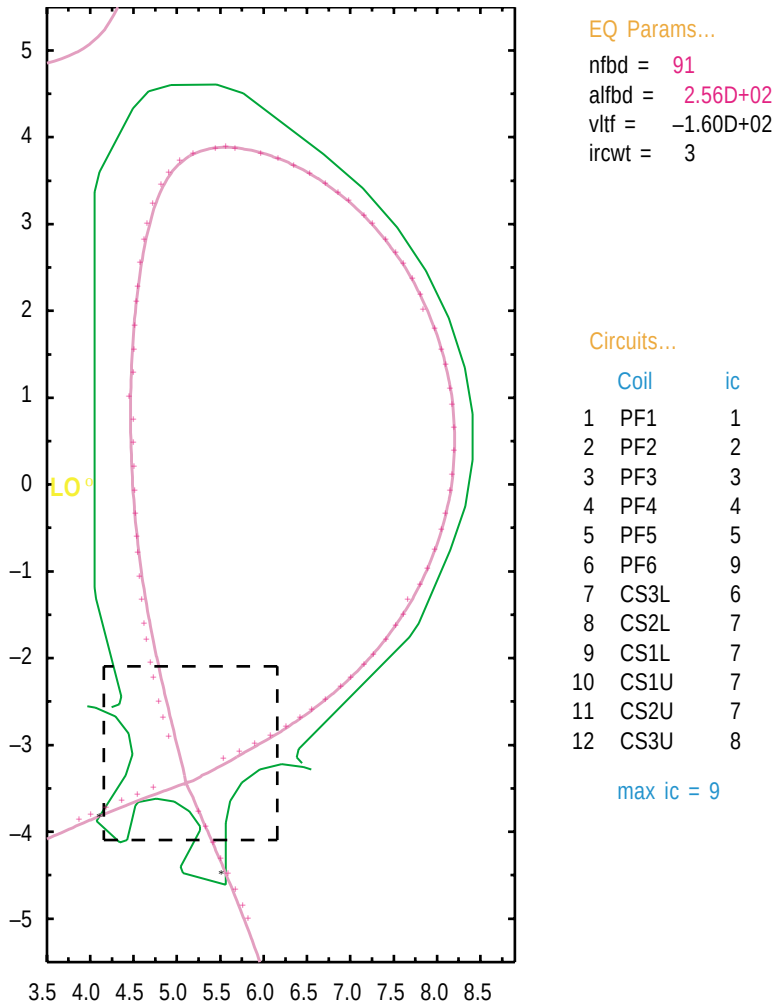

Fig. 7. ITER-AT seperatrix location for ITER WRS based on DIII-D 98549 profiles, relative to the plasma shape (+'s) specified by Gribov [4]. The first wall boundary is shown in green.

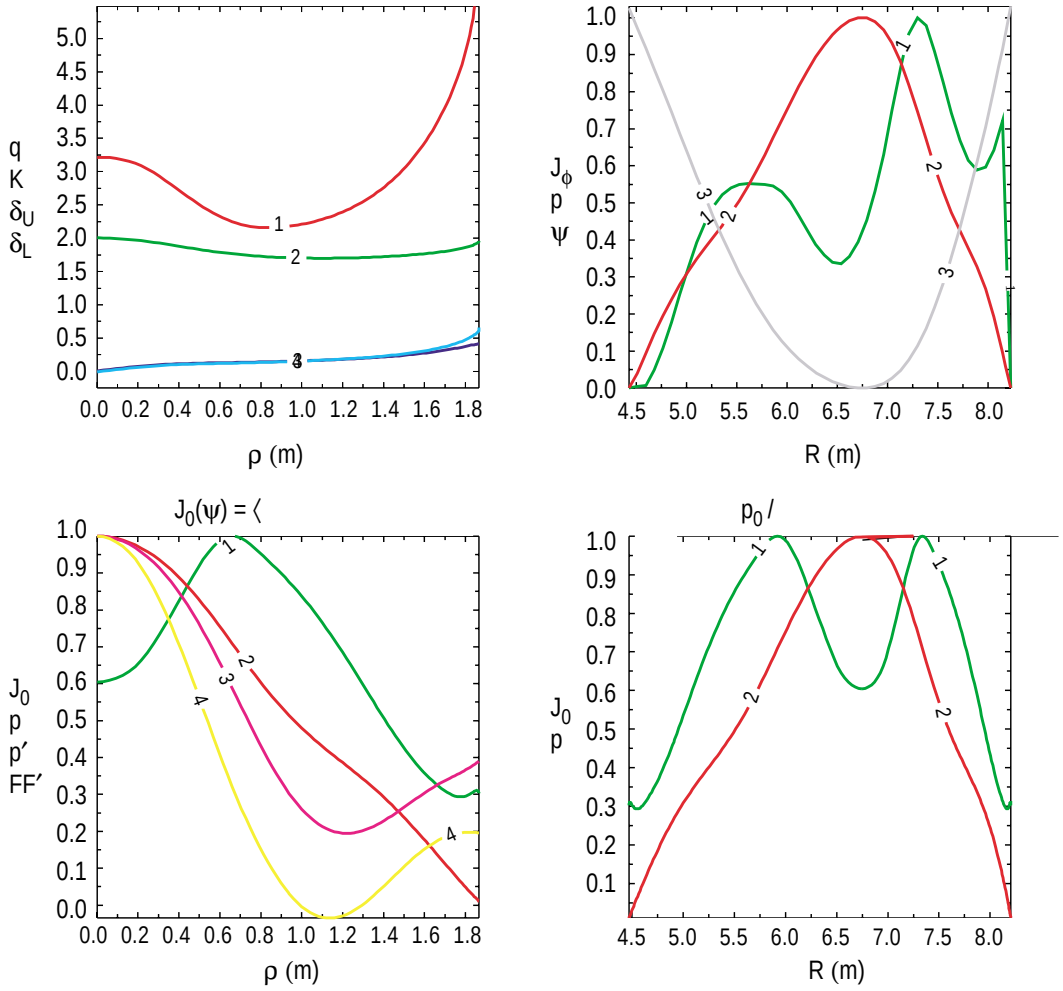

Fig. 8. ITER-WRS current profile variation with minor radius based on DIII-D's WRS current density profiles from Shot 98549. Curve numbering corresponds to the symbol order shown in the Y-axis labels.

2.4. ITER-AT-DIII-D EQUILIBRIUM (106795) NARROW EDGE PROFILE, FINITE EDGE CURRENT

A third equilibrium was generated based on profiles from one of DIII-D's best AT discharges: 106795. This discharge represents an upper single-null, WRS plasma with $\beta_N H_{89} = 12$, high β_T, $q_{min} > 1.5$, high boot strap fraction, and conditions sustained for of order 5 energy confinement times. This discharge has a well defined edge pressure pedestal occupying a small outer region of the discharge. Figure 9 shows the DIII-D EFIT equilibrium used in this analysis. The current profile parameter scaling is identical to that described in Section 3. Figure 10 shows the overall equilibrium shape and parameters from the Caltrans output for ITER operating on the DIII-D optimized AT profiles and with the ITER AT shape. Column E of Table I summarize the parameters. Like the previous equilibrium generated based on a DIII-D AT discharge, small differences are

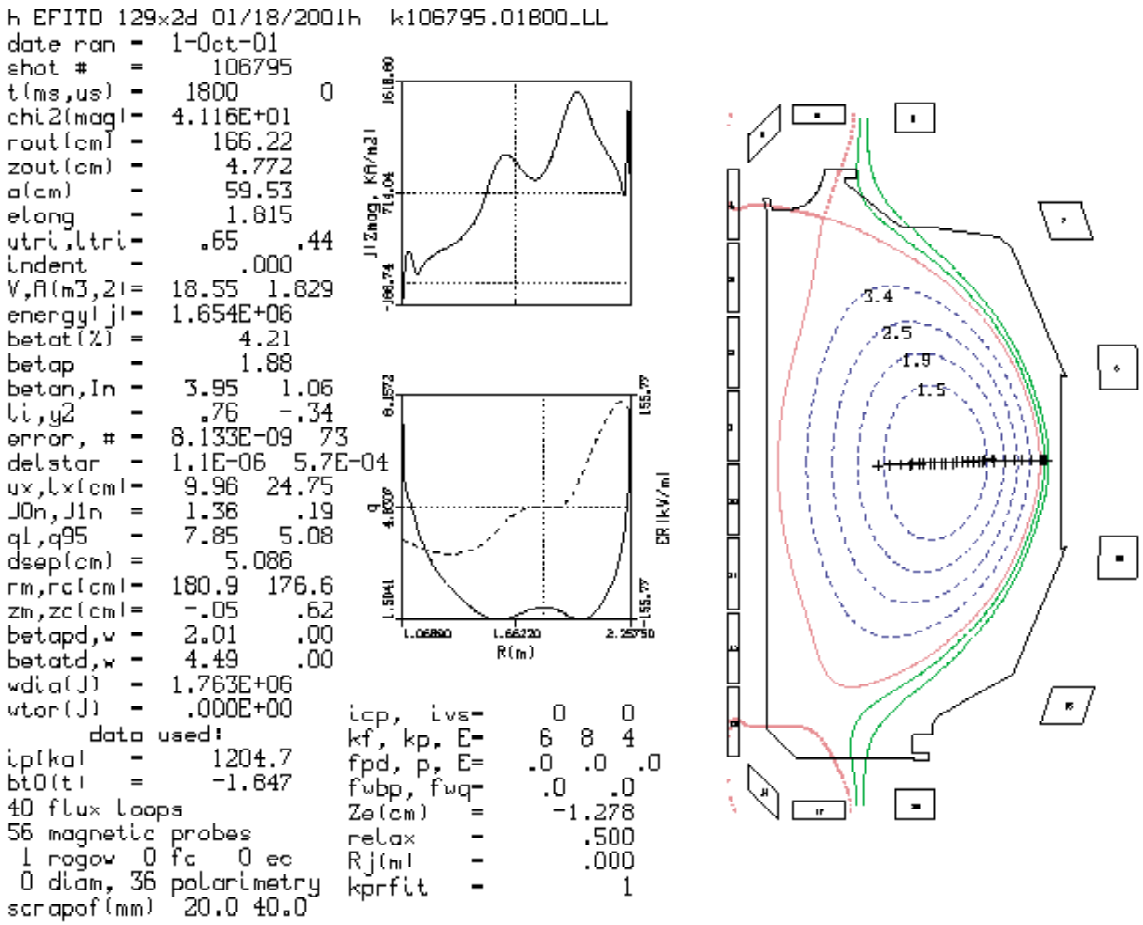

Fig. 9. High Performance DIII-D AT equilibrium from EFIT (106795), ($\beta_N H_{89} \sim 12$).

seen in all parameters except q-profile parameters. q values are lowest for this AT configuration. Figure 11 shows the shape relative to the ITER-AT shape and Figure 12 shows the main plasma profile variation with minor radius. As with the previous equilibrium this case has finite edge current.

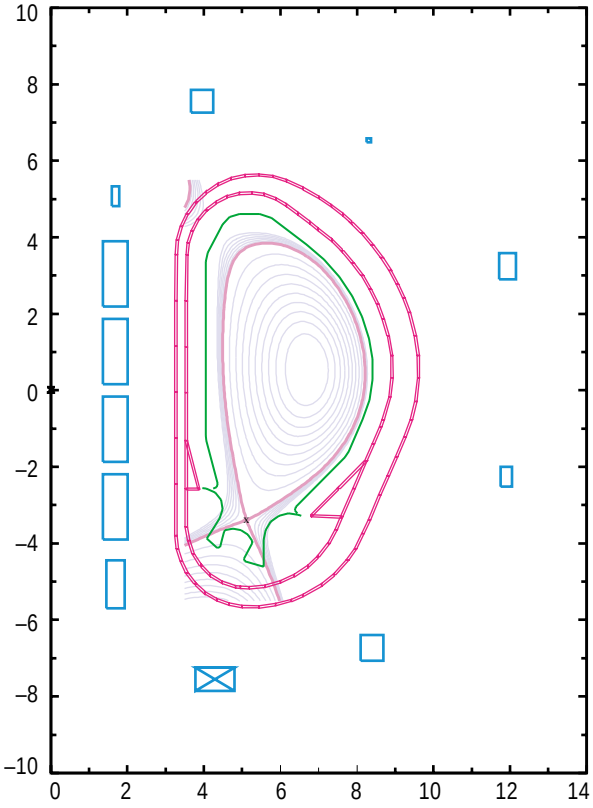

I_p, B_o, @ R	10.000	5.300	6.200
R_o, α, A	6.351	1.860	3.414
β_ϕ, β_N, β^*	3.602	3.452	4.474
$\beta_{p1,2,3}$	1.899	1.400	1.484
$l_{i1,2,3}$	0.724	0.530	0.562
q_0, q_{95}, q^*	2.191	4.639	3.058
q_{min}, ρ_{qmin}	1.599	0.359	
k_{95}, k_x	1.837	1.946	
δ_{95}, δ (U)	0.347	0.381	
δ_{95}, δ_x (L)	0.488	0.666	
$\Delta_{sep_{i,o}}$, ζ	0.000	0.000	0.025
R,Z_{axis}, ΔR	6.738	0.531	0.381
R,Z_{top}	5.641	3.850	
R,Z, ψ_{xpt} (L)	5.111	–3.390	–64.115
R,Z, Δl_{spt}	4.142	–3.765	1.039
R,Z, Δl_{spt}	5.565	–4.423	1.128
$\psi_{ext_{1,2,3}}$	–160.00	–164.28	–156.61
$L_{p_{n,a}}$ [μH], h_i	11.834	11.365	1.073
ψ_0, $\Delta\psi_p$, Φ	–21.269	–42.846	2.528
$W_{tot,c}$ [GJ]	7.476	8.484	3
alfa,betp (0)	4.911	1.000	999 0
epf, npf	0.130	–3.500	
alfa,betp (1)	2.590	1.000	999
epp, npp	0.100	–3.500	
betaj, β_{ps3}	.975	1.472	
R,$Z_{Jcentroid}$	6.529	0.494	
Vol., Sect.	773.880	19.974	

NI_{coil} =	PF1	PF2	PF3	PF4	PF5	PF6
	–7.042	–0.214	–5.987	–3.105	–7.969	12.402
	CS3L	**CS2L**	**CS1L**	**CS1U**	**CS2U**	**CS3U**
NI_{coil} =	–12.093	–22.076	–22.076	–22.076	–22.076	–2.055

Fig. 10. ITER-AT WRS Corsica equilibrium based on DIII-D AT current density profile and edge pedestal from DIII-D Shot 106795.

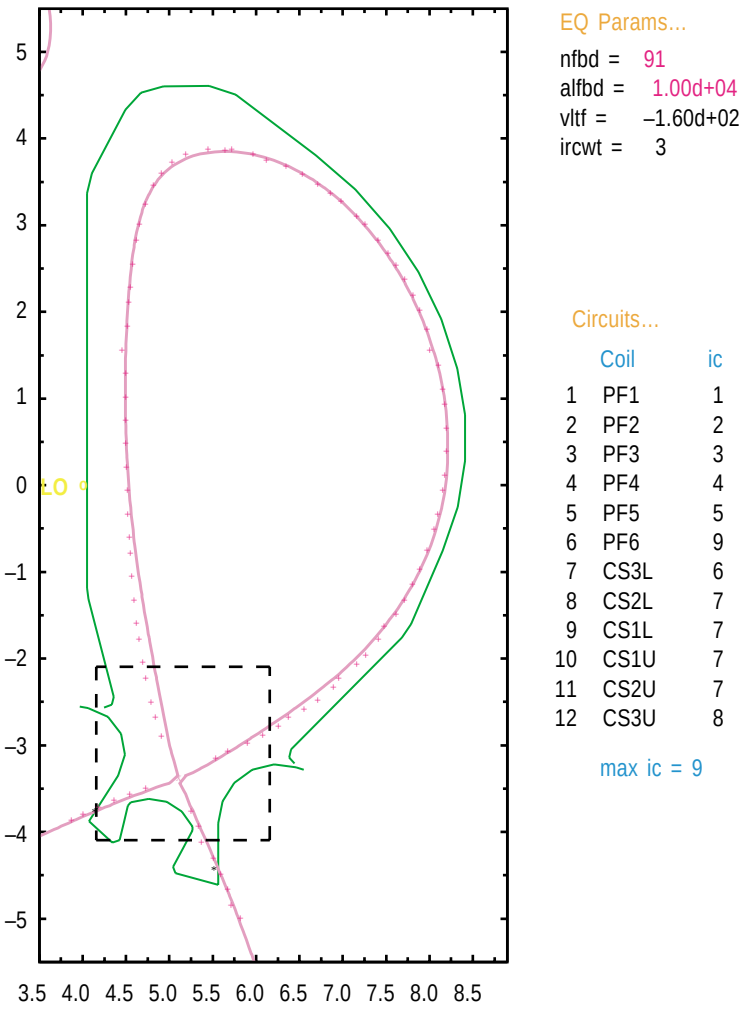

Fig. 11. ITER-AT separatrix location for ITER WRS based on DIII-D 106795 profiles, relative to the plasma shape (+'s) specified by Gribov [4] . The first wall boundary is shown in green.

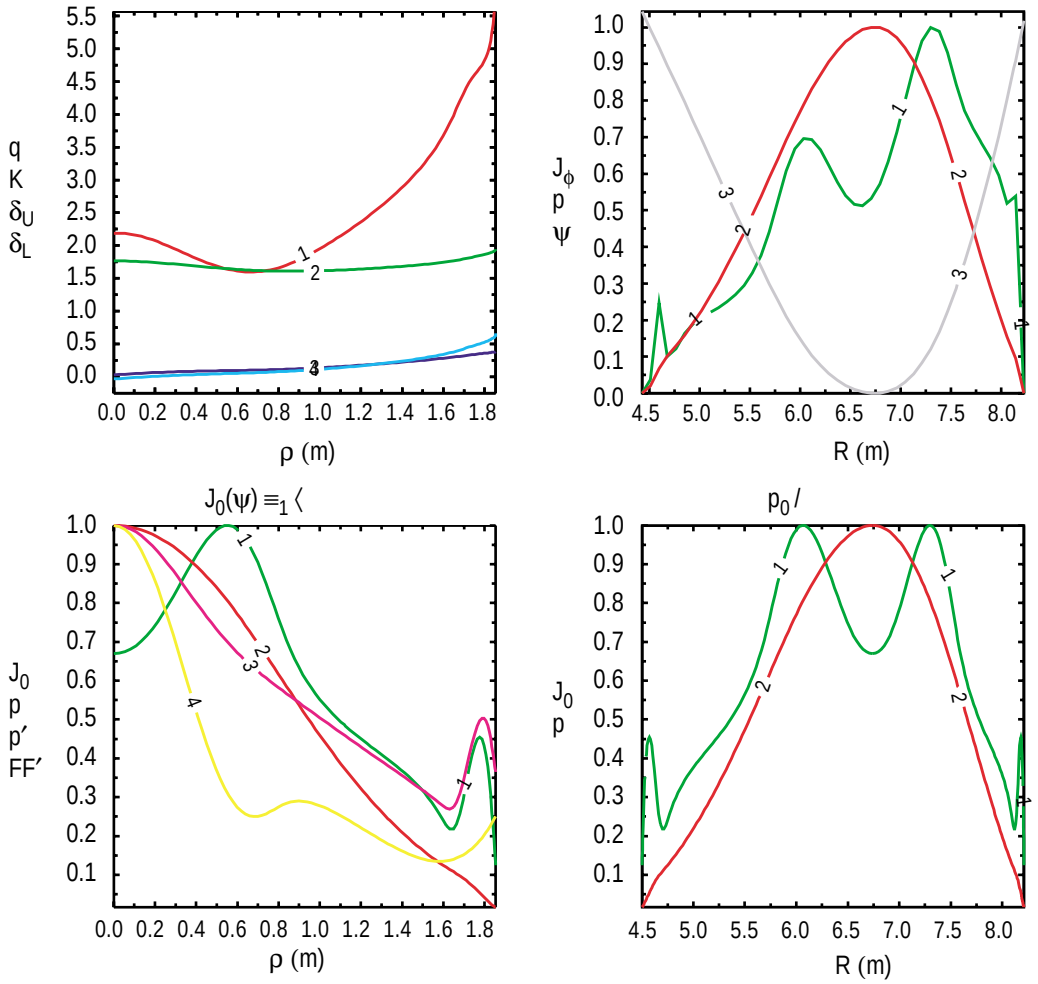

Fig. 12. ITER-WRS current profile variation with minor radius based on DIII-D's WRS current density profiles and pedestal from Shot 106795. Curve numbering corresponds to the symbol order shown in the Y-axis labels.

2.5. CURRENT PROFILE COMPARISONS

Figure 13 compares the current profile parameter, (f & p), variation with normalized flux for (1) ITER-FEAT reference, (2) ITER-AT reference, (3) ITER-AT with DIII-D 98549 profiles, and (4) ITER-AT with DIII-D 106795 profiles. Large differences between the ITER-FEAT reference equilibria and all the AT based configurations is evident. The pressure at the center is seen to peak in all AT configurations. Presumably this peaked center pressure improves the overall fusion rate. Further study is needed to determine if ITER has the current profile controls required to achieve this level of performance. Section 7 explores the overall performance of the device based on simple ITER scaling laws.

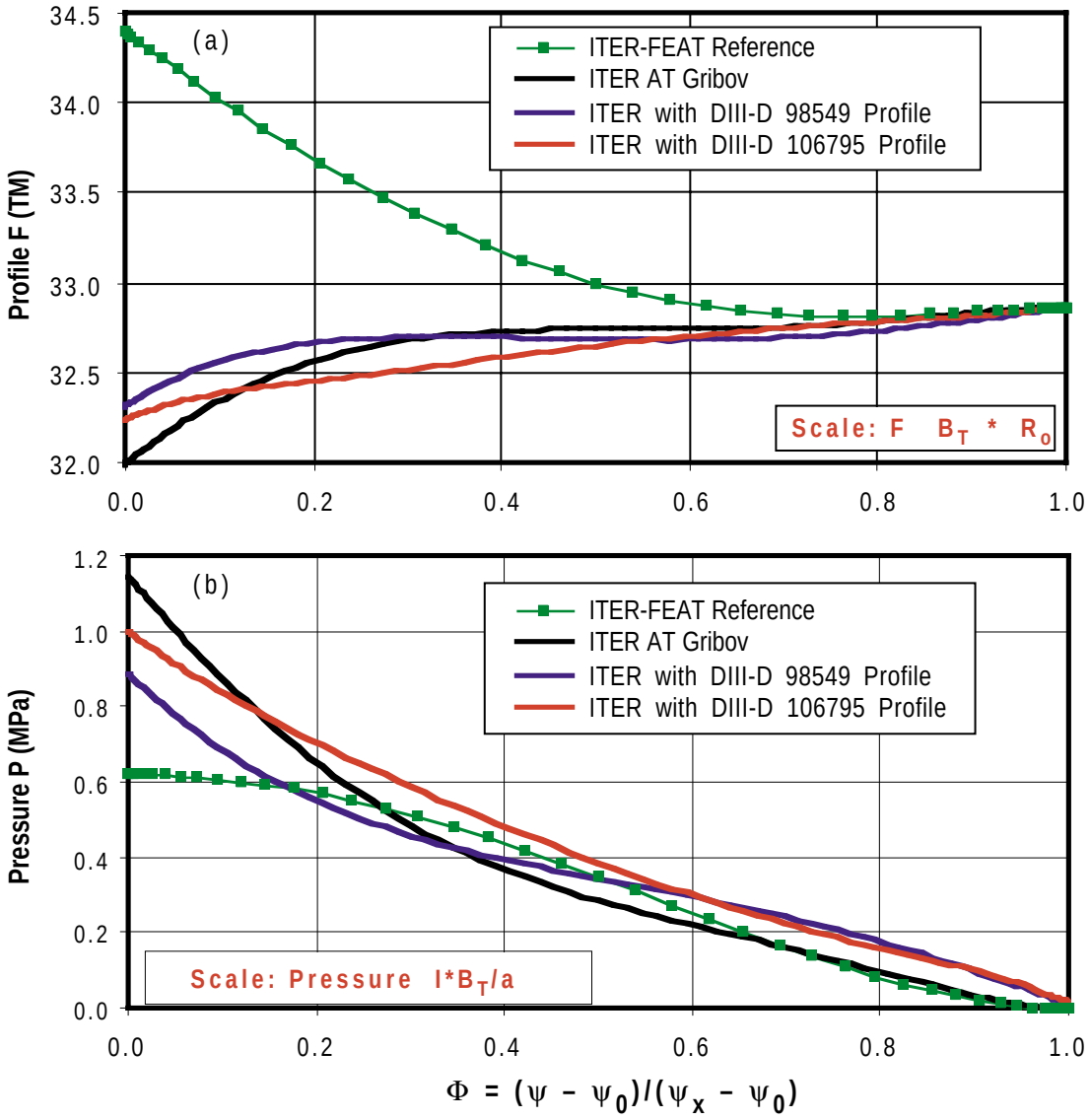

Fig. 13. Current profile variation with: (a) F(ϕ) and (b) P(ϕ) for 1) ITER-FEAT Reference, 2) ITER-AT WRS, 3) ITER based on DIII-D 98549 profiles, and 4) ITER based on DIII-D 106795 profiles,

Figure 14 show the normalized current profile parameter derivatives, (ff' and p') variation with normalized flux. The ITER-FEAT reference profiles are, again, very different from the AT profiles. The edge difference between AT pressure profiles are more evident in these figures. The edge pressure pedestal established based on DIII-D shot 106795 occupies the last 10% of the outer flux profile and represents a reasonably narrow pressure pedestal.

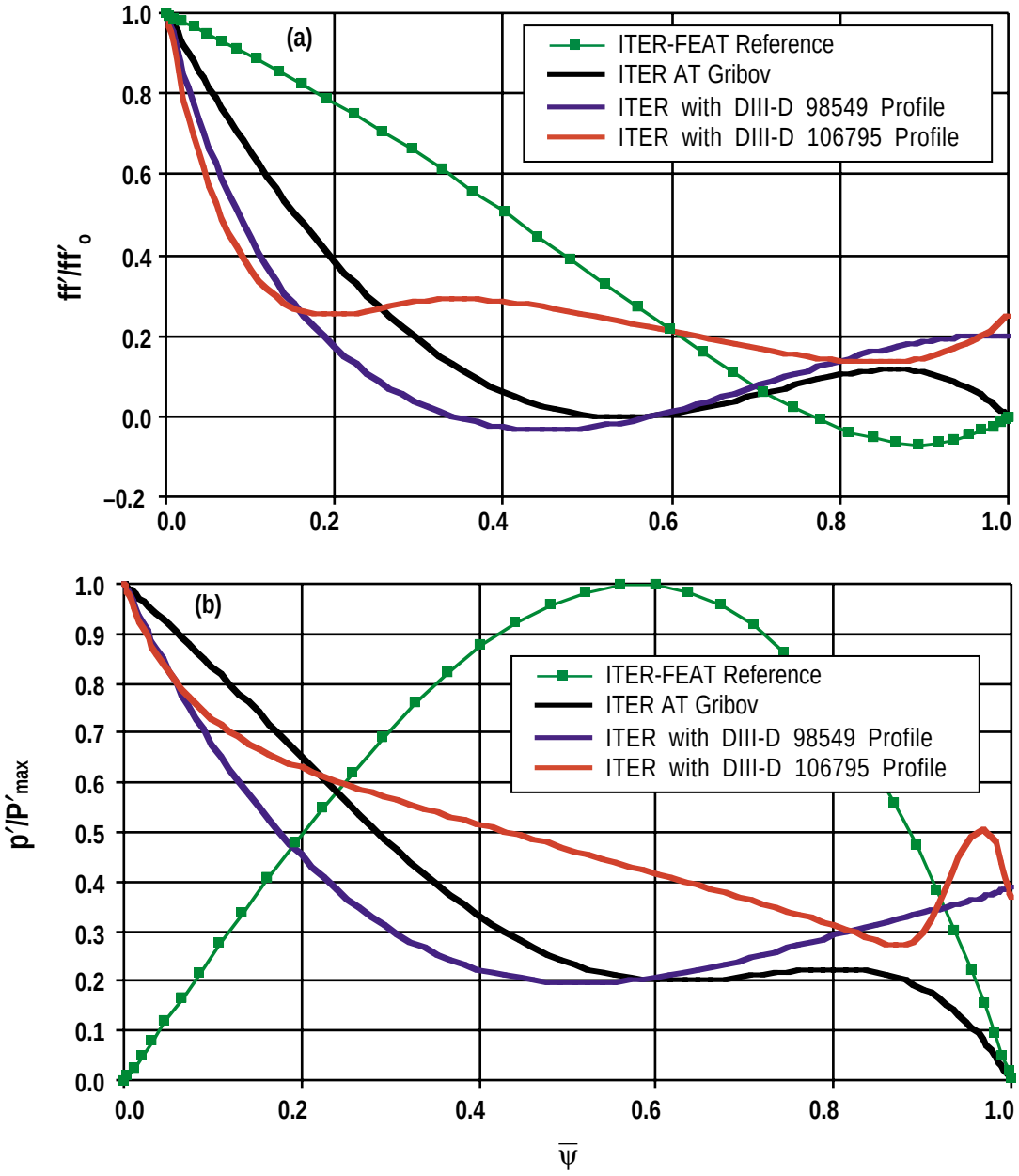

Fig. 14. Dimensionless current profile variation with: (a) ff' and (b) P' for 1) ITER-FEAT Reference, 2) ITER-AT WRS, 3) ITER based on DIII-D 98549 profiles, and 4) ITER based on DIII-D 106795 profiles.

2.6. INCREASED UPPER TRIANGULARITY

Experiments have shown that increased triangularity improves stability and can improve AT performance. Many DIII-D AT discharges are double-null configurations. Figures 15 and 16 show equilibria using the internal profiles from DIII-D Shot 106795 but with increased upper triangularity. The latter equilibrium is close to a double-null configuration with the upper X-point on the first wall surface. It is questionable if the upper divertor area can actually accommodate the high heat load expected from this configuration. Figures 17, 18 and 19 show the flux surfaces for the nominal triangularity and increased triangularity equilibria. The contours are in 1 cm increments measured at the midplane from the separatrix surface. This provides a method of evaluating the heat flux to the first wall surface.

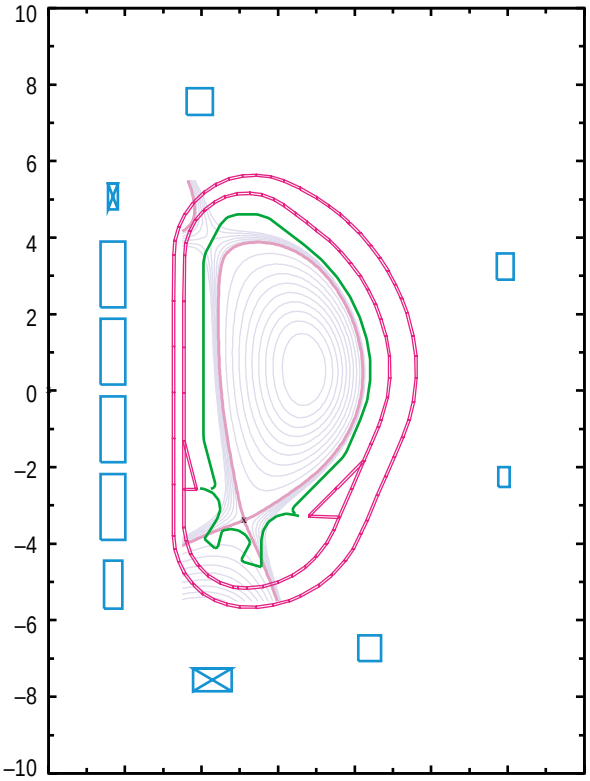

I_p, B_o, @ R	10.000	5.300	6.200
R_o, α, A	6.325	1.886	3.354
β_ϕ, β_N, β^*	3.532	3.418	4.391
$\beta_{p1,2,3}$	1.922	1.403	1.489
$l_{i1,2,3}$	0.730	0.530	0.562
q_0, q_{95}, q^*	2.236	4.887	3.080
q_{min}, ρ_{qmin}	1.628	0.357	
κ_{95}, κ_x	1.823	1.927	
δ_{95}, δ (U)	0.402	0.453	
δ_{95}, δ_x (L)	0.469	0.642	
$\Delta_{sep_{i,o}}$, ζ	0.000	0.000	0.035
R,Z_{axis}, ΔR	6.729	0.544	0.387
R,Z_{top}	5.471	3.878	
R,Z, ψ_{xpt} (L)	5.114	–3.391	–65.181
R,Z, Δl_{spt}	4.143	–3.765	1.041
R,Z, Δl_{spt}	5.565	–4.421	1.125
$\psi_{ext_{1,2,3}}$	–160.00	–164.45	–156.68
$L_{p_{n,a}}$ [μH], h_i	11.722	11.309	1.073
ψ_0, $\Delta\psi_p$, Φ	–22.437	–42.744	2.605
$W_{tot,c}$ [GJ]	7.634	8.648	3
alfa,betp (0)	4.911	1.000	999 0
epf, npf	0.130	–3.500	
alfa,betp (1)	2.590	1.000	999
epp, npp	0.100	–3.500	
betaj, β_{ps3}	0.975	1.478	
R,$Z_{Jcentroid}$	6.514	0.515	
Vol., Sect.	786.527	20.404	

	PF1	PF2	PF3	PF4	PF5	PF6
NI_{coil} =	–9.601	–0.020	–5.978	–3.079	–7.874	12.100
	CS3L	**CS2L**	**CS1L**	**CS1U**	**CS2U**	**CS3U**
NI_{coil} =	–11.985	–22.377	–22.377	–22.377	–22.377	–3.416

Fig. 15. ITER-AT with increased upper triangularity. Profiles based on DIII-D shot 106795.

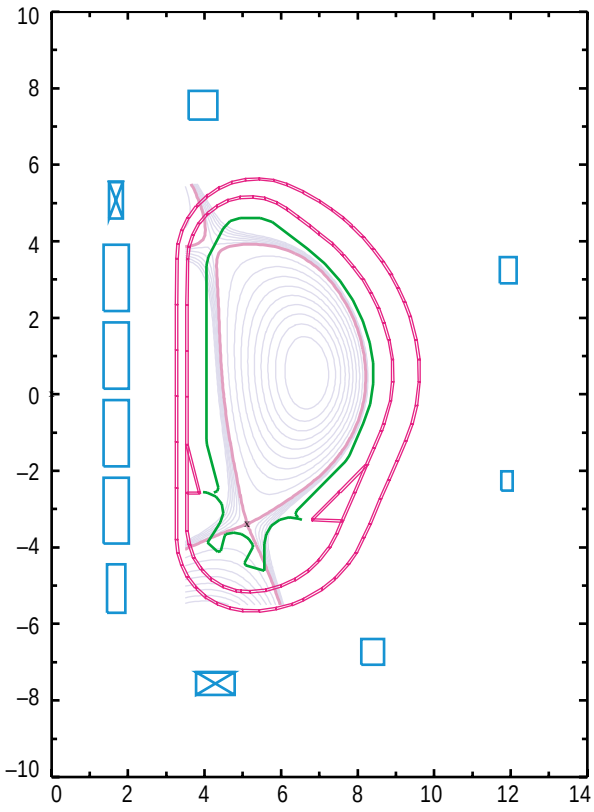

I_p, B_o, @ R	10.000	5.300	6.200
R_0, α, A	6.261	1.949	3.212
β_ϕ, β_N, β^*	3.466	3.381	4.319
$\beta_{p1,2,3}$	1.967	1.408	1.495
$l_{i1,2,3}$	.744	0.529	0.562
q_0, q_{95}, q^*	2.274	5.213	3.090
q_{min}, ρ_{qmin}	1.652	0.354	
κ_{95}, κ_x	1.808	1.876	
δ_{95}, δ (U)	0.459	0.534	
δ_{95}, δ_x (L)	0.450	0.589	
$\Delta_{sep_{i,o}}$, ζ	0.000	0.000	0.043
R,Z_{axis}, ΔR	6.722	0.554	0.392
R,Z_{top}	5.220	3.923	
R,Z, ψ_{xpt} (L)	5.114	–3.390	–65.888
R,Z, Δl_{spt}	4.143	–3.764	1.041
R,Z, Δl_{spt}	5.565	–4.420	1.125
$\psi_{ext_{1,2,3}}$	–160.00	–164.47	–156.62
$L_{p_{n,a}}$[μH], h_i	11.646	11.272	1.073
ψ_0, $\Delta\psi_p$, Φ	–23.222	–42.666	2.689
$W_{tot,\ c}$ [GJ]	7.825	8.843	3
alfa,betp (0)	4.911	1.000	999 0
epf, npf	0.130	–3.500	
alfa,betp (1)	2.590	1.000	999
epp, npp	0.100	–3.500	
betaj, β_{ps3}	0.975	1.485	
R,$Z_{Jcentroid}$	6.500	0.536	
Vol., Sect.	800.055	20.874	

	PF1	PF2	PF3	PF4	PF5	PF6
NI_{coil} =	–11.287	–0.175	–5.993	–3.019	–7.893	12.047
	CS3L	**CS2L**	**CS1L**	**CS1U**	**CS2U**	**CS3U**
NI_{coil} =	–12.149	–22.518	–22.518	–22.518	–22.518	–6.902

Fig. 16. ITER-AT with an extreme upper triangularity. Plasma is close to a double null configuration. Profiles based on DIII-D shot 106795.

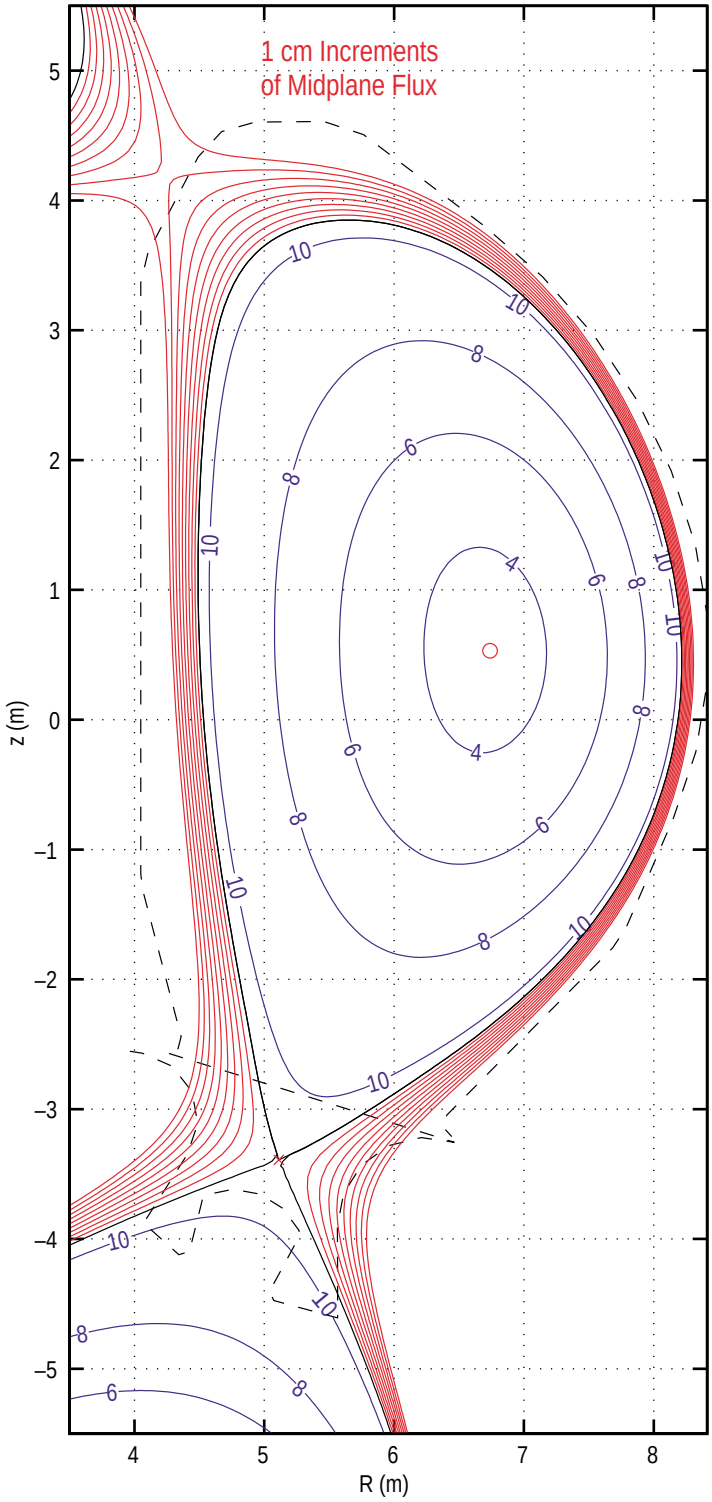

Fig. 17. ITER-AT Reference shape flux contours. Exterior contours are in increments of 1 cm measured from the separatrix at the midplane. Profiles based on DIII-D shot 106795.

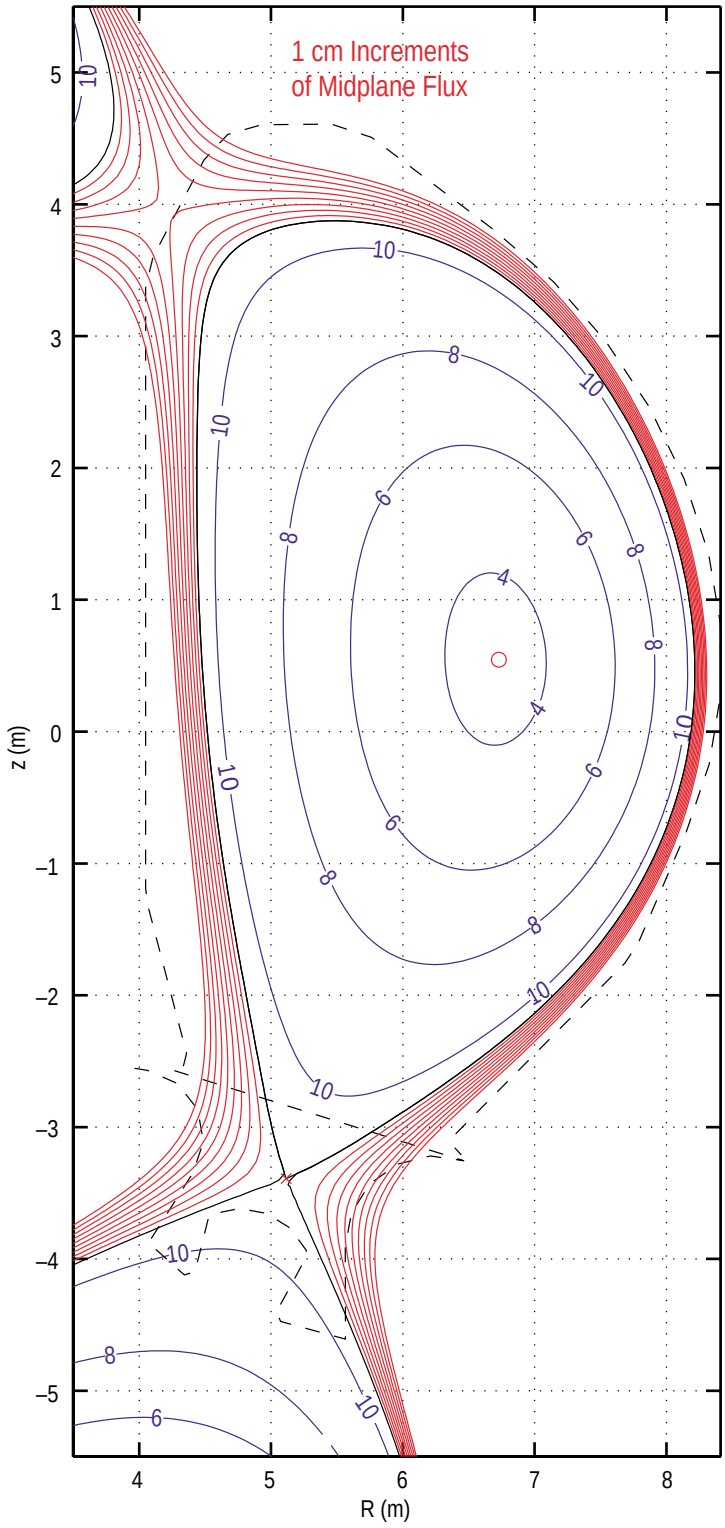

Fig. 18. ITER-AT Moderate Upper Triangularity flux contours. Exterior contours are in increments of 1 cm measured from the separatrix at the midplane. Profiles based on DIII-D shot 106795.

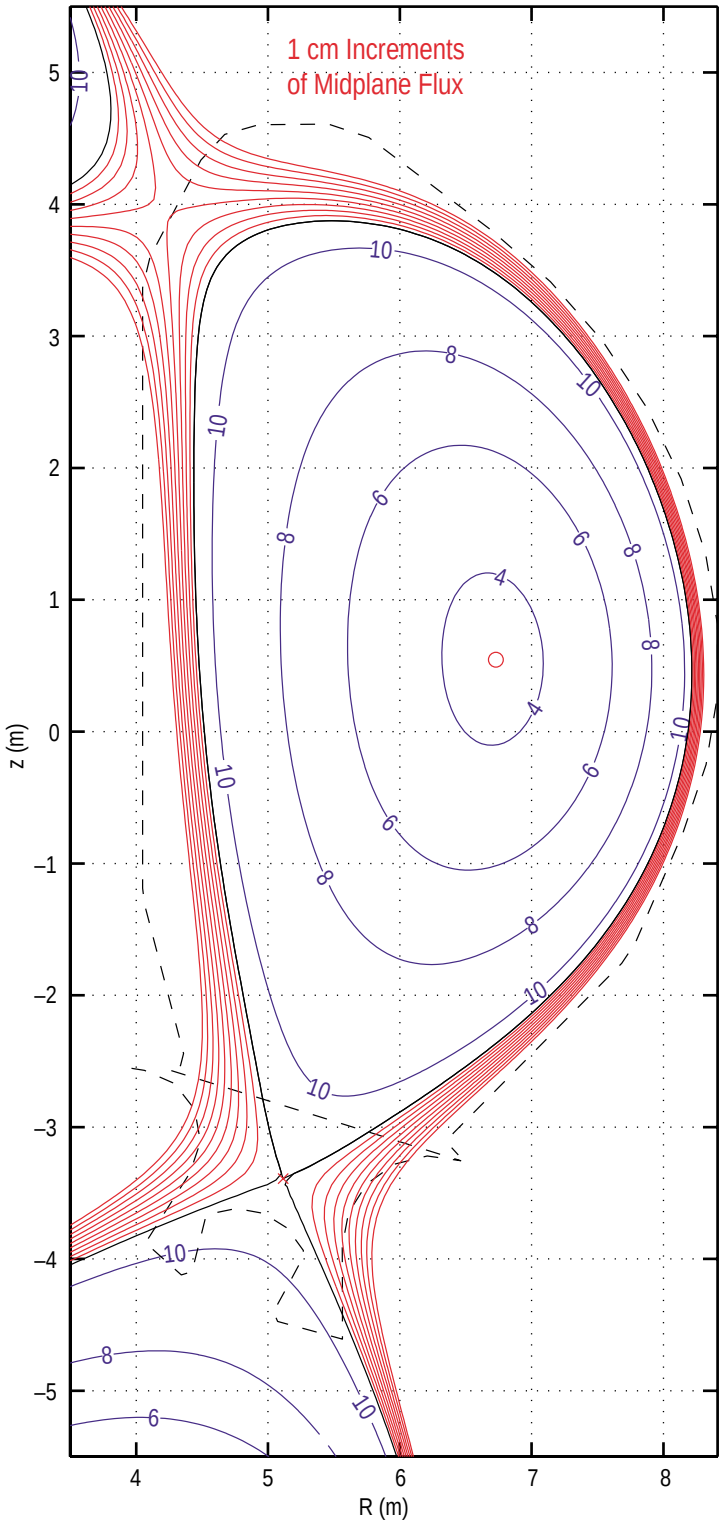

Fig. 19. ITER-AT High Upper Triangularity flux contours. Exterior contours are in increments of 1 cm measured from the separatrix at the midplane. Profiles based on DIII-D shot 106795.

2.7. ESTIMATE OF AT PERFORMANCE BASED ON 0-D ITER SCALING RULES (TokSim)

In our pervious study we used the 0-D ITER scaling rules published by the ITER project to estimate the performance of the baseline ITER configuration [1,2]. Here we use the same scaling rules, which are implemented in TokSim, to estimate the performance of the ITER-AT configurations developed above. Readers interested in the form of the equations should consult Ref. [1]. It should be noted that the scaling laws were developed primarily based on more conventional current profiles. The scaling rules very accurately predict the reference ITER performance as can be seen by comparing Table II Column A1 (ITER published performance) with Column A2, (SysTok predicted performance). The predictive capability of the simple formula for the more advanced current profiles used in this study is less certain. However, the main 0-D profile dependent parameters influencing performance, β_N and H_{89}, are included in the model and the solution should reasonably predict overall fusion performance.

Table II shows the overall predictions of the simple 0-D model. Comparisons with ITER published numbers can only be done for the Reference case (Columns A1 and A2); the ITER program predictions for the AT configuration used in this study are not available. Also, the actual $\beta_N H_{89}$ product for the Gribov equilibrium (Columns C and D) is unknown and assumed to be 9. In addition, the ITER reference performance (Columns A1 and A2) use conservative density and beta limit scaling (~85% and 72% respectively). For the AT performance numbers (Columns B through E), the fusion power was maximized within 100% of the density and beta limits without any degradation in confinement. In this sense, the AT solutions are much less conservative than the reference design. In any case, the bottom line performance, as defined by big Q, is comparable for the ITER Reference and the solutions for $\beta_N H_{89} \sim 9$ (Columns A through D). The performance of the ITER configuration based on the most advanced DIII-D AT discharge $\beta_N H_{89} \sim 12$ (Column E) indicates that the machine would actually ignite. This is remarkable in that the plasma current, at 10 MA, is well below the design value of 15 MA. This indicates the relative value of achieving large $\beta_N H$ product. Indeed, in the simple scaling rules, the $\beta_N H$ product is the most important performance knob next to toroidal field and plasma current. It remains to be seen if more detailed 1-D and 2-D analysis show the same performance.

2.8. STUDY LIMITATIONS

In developing the equilibria used in this study, no attempt was made to reconcile the flux state and poloidal field (PF) coil currents in the device with actual engineering limits. Coil currents ultimately constrain the flux swing capability of the device and can limit operation of certain equilibrium configurations. However, the reduced plasma current

requirements expected in the AT configuration (10 MA vs. 15 MA in the reference case), should be less demanding on the PF coil system. All equilibria found in this study are free boundary equilibria and currents are well within the capability of the machine. The AT configuration, with its higher Shafranov shift, is expected to yield improved global plasma shape control properties. However, this has not been investigated and all equilibria are assumed controllable with the ITER outer superconducting PF coils.

No attempt has been made to determine if the ITER design contains the current profile control equipment necessary to achieve the optimized profiles used in this study. It should be noted that negative central shear (NCS) type discharges were explored for steady state use in the full size ITER-EDA device [6]. Based on TSC analysis, 50 MW of ion cyclotron heating (ICH) (fast wave) and 50 MW of lower hybrid heating (LHH) power were needed to achieve the prescribed NCS discharges. In this report, simple scaling of DIII-D profiles is used to achieve the profiles in the ITER device. Profile variation with normalized flux is assumed similar and overall constants are modified to reflect the larger size and field of ITER. No attempt was made to reconcile the differences in shape between the optimum DIII-D discharges and the shape used for the ITER AT discharge.

2.9. PROJECT INFORMATION

Requester: V. Chan

Project: IR&D Project 4437

Document: ITER_AT_equilibria_01

Code area: GA-Unix: ITER-FEAT Caltrans area:

1) ITER-WRS-AT Area: /u/leuer/corsica/iter/wrs2/

iter_wrs10a.sav	corsica/caltrans save set
iter_wrs.001.ncgm	cgm meta plot file containing:
iter_wrs10a_129.cgfile	corsica generated eqdsk 129x129
iter_wrs10a_129.gfile	eqdsk converted for GATO use 129x129
iter_wrs10a_65.cgfile	corsica generated eqdsk 65x65
iter_wrs10a_65.gfile	eqdsk converted for GATO use 65x65

2) ITER-WRS-DIII-D (shot 98549) Area: /u/leuer/corsica/iter/wrs_ped/

iter_wrs_d3d_2.sav	corsica/caltrans save set
iter_wrs_d3d_2.001.ncgm	cgm meta plot file containing plots
iter_wrs_d3d_2.cgfile	corsica generated eqdsk 129x129
iter_wrs_d3d_2_129.gfile	eqdsk converted for GATO use 129x129
g098549.01900_a_65	DIII-D G-file used to extract profiles
iter_wrs_d3d.txt	Notes on equilibrium construction

3) ITER-WRS-DIII-D (shot 106795) Area: /u/leuer/corsica/iter/wrs_ped3/

iter_wrs_d3d_106795_5.sav	corsica/caltrans save set
iter_wrs_d3d_106795_.001.ncgm	cgm meta plot file containing plots
iter_wrs_d3d_106795_.cgfile	corsica generated eqdsk 129x129
iter_wrs_d3d_106795_5.gfile	eqdsk converted for GATO use 129x129
g106795.01800_LL	DIII-D G-file used to extract profiles (in /wrs_ped2/)
iter_wrs_d3d_106795_6.gfile	Moderate Triangularity eqdsk129x129
iter_wrs_d3d_106795_7.gfile	High Triangularity eqdsk129x129

The newest reference ITER-AT equilibrium is contained in eqdsk file:

/u/leuer/corsica/iter/wrs_ped3/iter_wrs_d3d_106795_5.gfile. This equilibrium is very similar to the old reference (_4) except the lower separatrix better fits the divertor.

3. STABILITY OF ITER-FEAT AT PLASMAS

3.1. ANALYSIS OF ITER-FEAT VERTICAL STABILITY AND DISRUPTION HALO CURRENTS

3.1.1. Introduction

The largest loads experienced by plasma facing components and vessel walls in tokamaks occur during vertical displacement events (VDE) and other types of disruptions. The vertical stability growth rate determines the amplitude and distribution of toroidal currents induced by VDE motion, and has also been demonstrated to be a key determinant of the peak halo current driven during the current quench of a VDE [7,8]. The vertical stability of a tokamak equilibrium is therefore an essential quantity to evaluate in determining the expected severity of such loads, as well as for analyzing the controllability and power supply constraints of a machine design.

In addition to the vertical growth rate, the post-thermal quench core and halo plasma resistivities are needed in order to calculate the expected halo current. A set of DIII–D AT disruptions has been studied in order to determine a reasonable choice for these values. The results have been used to guide the choice of post-thermal quench plasma conditions in performing halo current evolution simulations.

3.1.2. Vertical Stability Analysis

The vertical stability growth rate has been calculated for a recently developed ITER-FEAT AT equilibrium with pedestal profiles taken to be consistent with DIII–D experience [9]. The Caltrans code VST package was used for vertical stability assessment. This algorithm calculates the vertical stability eigenmodes and eigen values for a specified set of discrete resistive elements representing all toroidal conductors including the vacuum vessel, PF coils, and first wall, assuming an ideal (flux-conserving) fully deformable plasma. The resulting growth rate and corresponding stability factor are shown in Table III along with the growth rate and stability factor calculated for the reference case.

TABLE III
SUMMARY OF GROWTH RATES AND STABILITY FACTORS

Case	Growth Rate	Stability Factor
ITER-FEAT “DIII–D AT” (wrs4)	4.5 rad/s	1.74
ITER-FEAT Reference	6.2 rad/s	1.54

As is generally the case in present-day devices, the high β_N AT scenario produces a significantly lower growth rate than the reference case owing to the greater Shafranov shift which increases the coupling between the toroidal plasma current and the outboard conducting structure and coils.

Figure II-1 shows the ITER-FEAT "DIII-D AT" (wrs4) configuration used for the vertical stability analysis. The discretized vessel model consists of 115 elements representing both inner and outer layers of the ITER-FEAT vessel [10].

Figure 20 shows the displacement vectors corresponding to the unstable eigenmode for the AT case, and Fig. 21 shows the contours of perturbed flux for the same mode. Both figures demonstrate the global, largely vertical motion of the unstable mode. For comparison, Figures 22 through 24 show the configuration, displacement vectors, and perturbed flux contours respectively corresponding to the unstable mode for the reference case. The effect of the larger Shafranov shift is evident in comparing the reference and AT cases configurations and eigenmodes.

3.1.3. Disruption Halo Current Calculations

3.1.3.1. GA Analytic Halo Current Model. A halo current model was developed several years ago by the DIII-D Disruption Group in order to understand (axisymmetric) halo currents observed in present day experiments and allow development of scenarios to minimize the peak halo current experienced during a disruption [10]. Experimental studies on DIII-D and other devices demonstrated that the largest halo currents tend to occur in VDE disruptions rather than major disruptions. The model and subsequent validation against several different tokamaks (Alcator C-Mod, JT-60SU, and DIII-D [11]) demonstrated that peak disruption halo current is minimized by high plasma resistivity in core and halo, and by low vertical stability growth rate. In order to simulate the disruption process relevant to halo current production and calculate the peak halo current expected in a device, the vertical growth rate and expected post-thermal quench plasma resistivities must be specified. The analysis of Section 2 describes determination of the vertical growth rate. In the absence of a complete theory to predict post-thermal quench plasma resistivity, a study has been done to provide some guidance based on DIII-D AT disruption data. The section following describes this study. One caveat concerning this use of DIII-D data is that if the post-thermal quench plasma conditions are heavily influenced by wall material (graphite in DIII-D), the results would not extrapolate to a non-graphite device such as ITER-FEAT.

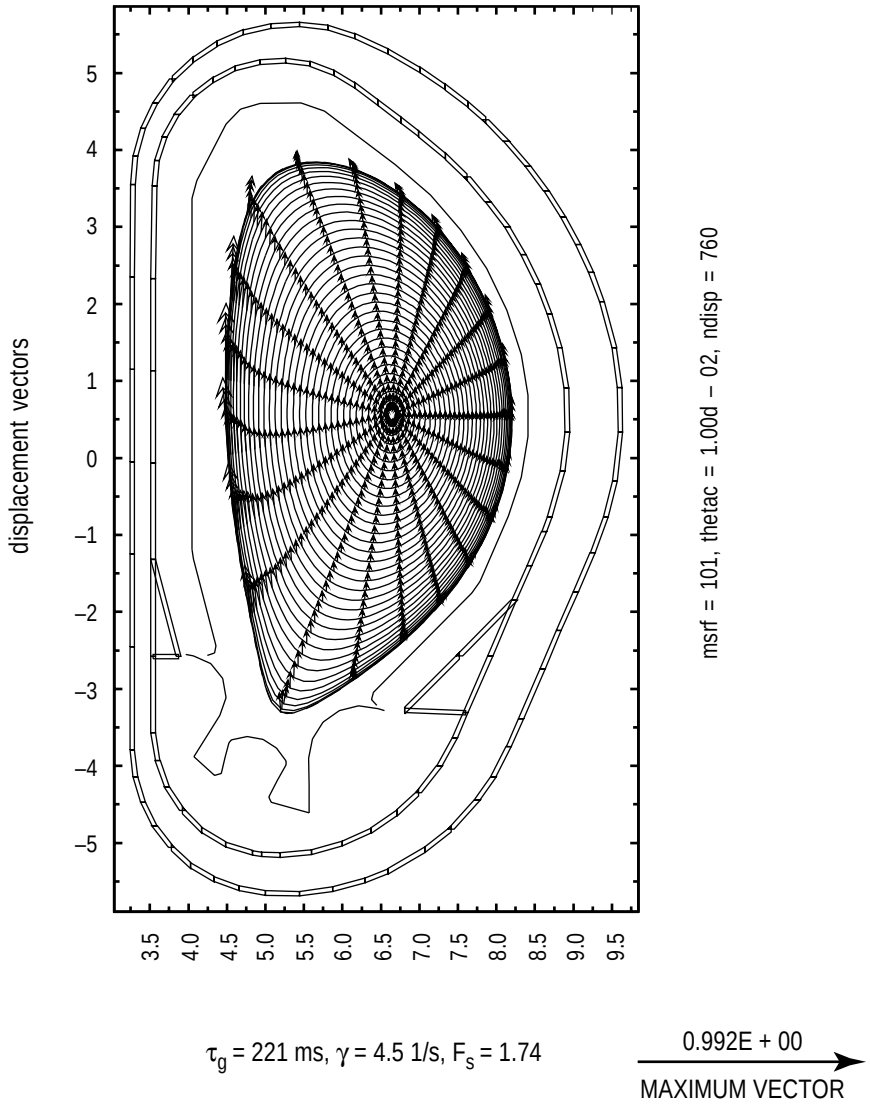

Fig. 20. Displacement vectors corresponding to the unstable eigenmode of the AT case.

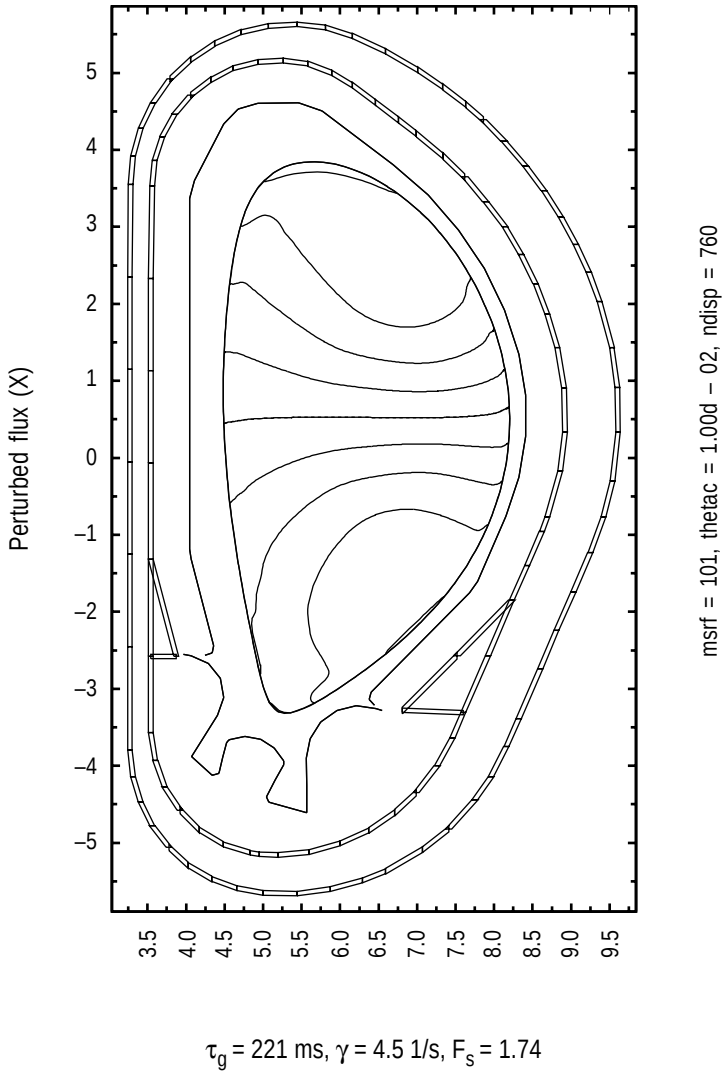

Fig. 21. Contours of perturbed flux for the unstable eigenmode of the AT case.

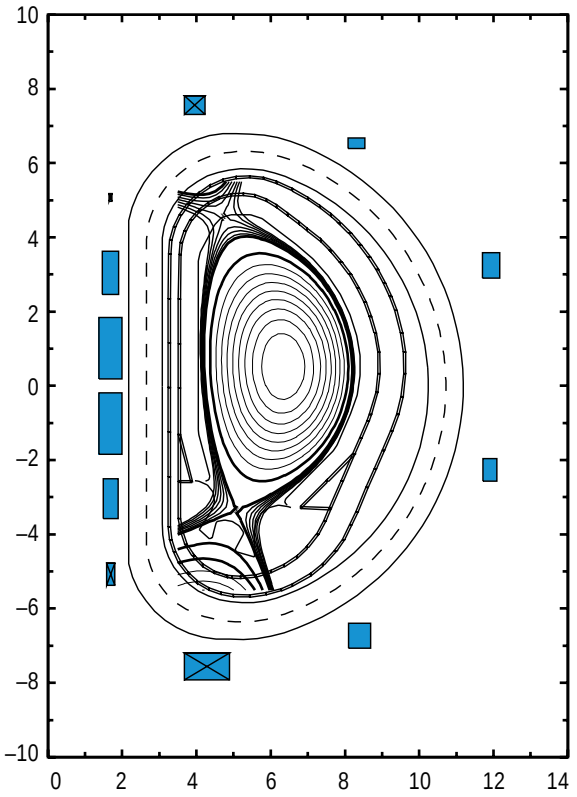

I_p, B_o, @ R	15.000	5.300	6.200
R_o, α, A	6.200	2.000	3.100
β_ϕ, β_N, β^*	2.492	1.756	3.198
$\beta_{p1,2,3}$	0.651	0.515	0.527
$l_{i1,2,3}$	1.054	0.832	0.851
q0, q95, q*	1.115	2.969	2.199
k_{95}, k_x	1.698	1.845	
δ_{95}, δ (U)	0.334	0.433	
δ_{95}, δ_x (L)	0.318	0.559	
$\Delta_{sep_{i,o}}$, ζ	0.062	0.040	0.033
R,Z_{axis}, ΔR	6.345	0.522	0.141
R,Z_{top}	5.333	4.025	
R,Z, ψ_{xpt} (U)	4.727	4.550	–5.499
R,Z, ψ_{xpt} (L)	5.082	–3.355	–2.618
R,Z, Δl_{spt}	4.160	–3.737	0.997
R,Z, Δl_{spt}	5.565	–4.458	1.204
$\psi_{ext_{1,2,3}}$	–127.16	–130.41	–127.19
ψ_{init}, C_{Ejima}	99.752	0.450	
$L_{p_{n,a}}$ [μH], h_i	11.620	11.483	1.355
ψ_0, $\Delta\psi_p$, Φ	76.599	–79.216	1.563
$W_{tot,\ c}$ [GJ]	6.408	7.008	3
alfa,betp (0)	2.000	2.637	3 2
alfa,betp (1)	2.000	2.000	3
betaj, β_{ps3}	0.224	0.526	
R,$Z_{Jcentroid}$	6.228	0.520	
Vol., Sect.	830.776	21.0924	

	PF1	PF2	PF3	PF4	PF5	PF6
NI_{coil} =	5.610	–2.563	–6.289	–4.671	–7.874	17.611
	CS3L	**CS2L**	**CS1L**	**CS1U**	**CS2U**	**CS3U**
NI_{coil} =	2.680	–8.758	–20.653	–20.653	–10.050	0.307

Fig. 22. ITER-FEAT reference configuration used for vertical stability calculation.

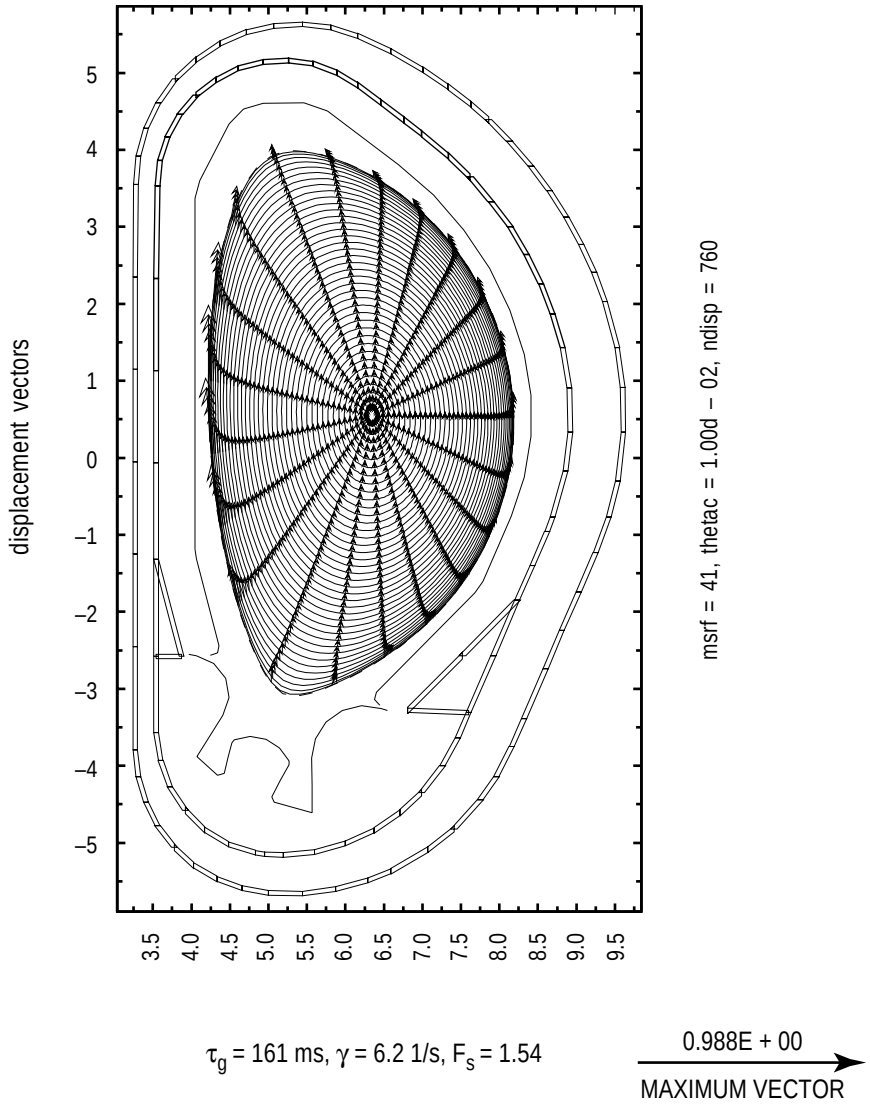

Fig. 23. Displacement vectors corresponding to the unstable mode for the reference case.

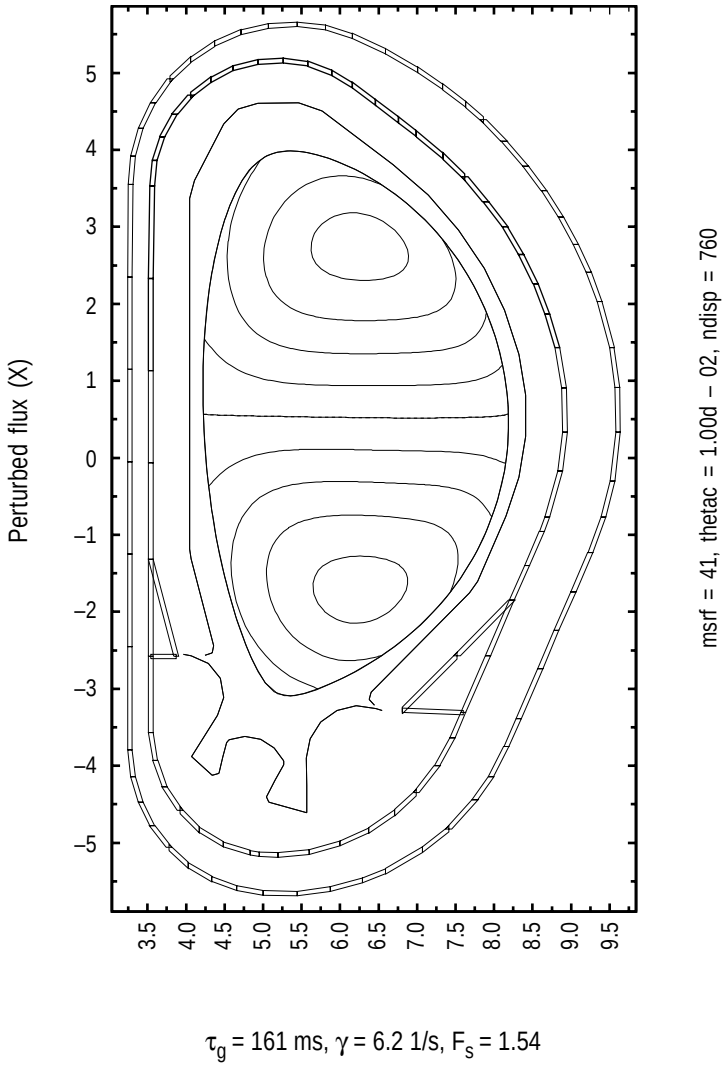

Fig. 24. Perturbed flux contours corresponding to the unstable mode for the reference case.

3.1.3.2. AT Disruptions in DIII–D. The behavior of plasma current quenches during disruptions in high performance DIII-D plasmas has been studied as a function of β_N. Our goal was to determine a simple relationship for the scaling of the peak current quench rate as a function of β_N that could be used to predict the properties of quenches during disruptions in high performance tokamak reactors. A database of over 1000 discharges was assembled from the DIII-D 2001 experimental run year. Approximately 85 naturally-occurring (not intentionally triggered) major disruptions were found in the database. Of these 67 were suitable for the β_N scaling study.

During uncontrolled plasma current terminations in tokamaks the rate at which the energy stored in the poloidal magnetic field is dissipated depends on the plasma resistivity (R) and its total inductance (L) or γ_N = R/L (1/s) assuming classical dissipation mechanisms dominate the process. The plasma current (I_p) quench phase can be

characterized by a time dependent normalized quench rate γ_N (t) = $dI_p/dt/I_{p0}$ (1/s) where I_{p0} is the pre-disruptive plasma current. Comparisons of non-AT high β_P and ohmic plasma disruptions show that γ_N increases with increasing β_P. If a similar scaling holds in AT plasmas, then halo currents driven by dI_p/dt and their associated forces on plasma facing and vacuum vessel components will also be reduced in high performance, high β_N, AT plasmas.

In general the time dependent behavior of γ_N is not well described by a simple analytic function. Thus, in the study outlined here we are primarily interested in the amplitude of the γ_N peak and will not discuss the complex properties of the more general γ_N curve or the relative position of the γ_N peak compared to the initiation time of the current quench phase. Studies of the detailed properties of γ_N(t) should be done in connection with the development of a general model for the current quench process at some point in the future.

The primary results obtained during this study are shown in Fig. III-1. Here the variation in the peak γ_N amplitudes seen during our 2001 DIII-D disruptions are plotted against the pre-disruptive β_N determined at the onset of the current quench phase. It should be noted that this analysis is somewhat fuzzy because it is not completely clear if the most appropriate β_N to be used is that just prior to the onset of the current quench or the peak value of β_N obtained during an earlier phase of the discharge. These can sometimes differ by 40%–50% in high β_N plasmas and thus would shift some of the points in the $2.5 < \beta_N < 3.0$ region of Fig. 1 above 3.5. If the decay in β_N seen prior to some disruptions in high performance plasmas is due primarily to a loss of edge confinement then it would be reasonable to use the higher β_N instead of those used in to construct Fig. 25. At this point we have no evidence that this is the case so we believe the method used here is appropriate although this question should be examined in more detail during a future study.

In general, Fig. 25 suggests that there isn't a strong correlation between γ_N and β_N. At best it implies that there may be a very weak trend toward increasing γ_N with β_N which if confirmed with additional data would imply slightly reduced halo current amplitude with increasing β_N. Clearly, more data is needed for cases with $\beta_N > 2.5$ to fully verify the existence of this trend.

Based on the limited data shown in Fig. 25 we are drawn to the conclusion that our reference high performance ITER-FEAT plasmas with $\beta_N = 3.4$ will have a maximum disruptive quench rate, during the most severe cases, that is roughly comparable to that of the low β_N discharges. In DIII-D the least severe AT cases have peak current quench rates of about 0.305 ms^{-1} regardless of the value of β_N. Thus, disruption halo currents should not increase in severity with increasing plasma performance. On the other hand,

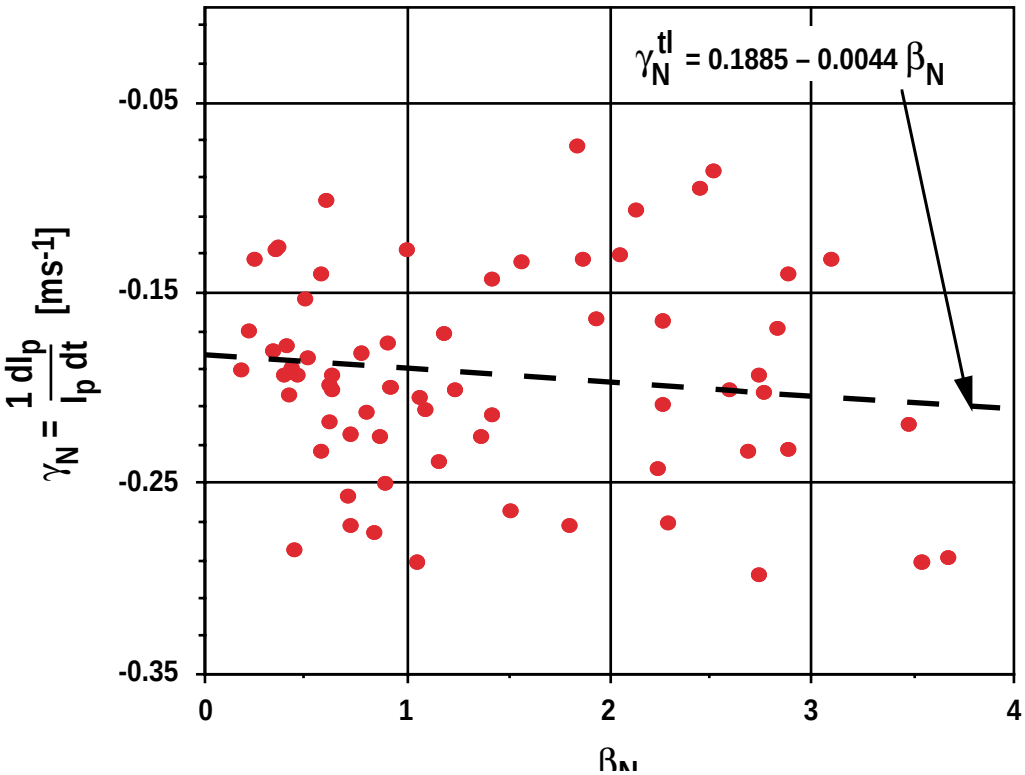

Fig. 25. Peak normalized plasma current quench rates in DIII–D disruptions with various pre-disruptive β_Ns.

the quench rates during average events appear to increase approximately 12% from β_N = 1.0 to β_N = 3.4 although the relative scarcity of data at β_N = 3.4 makes the uncertainty in this estimate rather large. Another interesting observation is that the lower limit on γ_N appears to be increasing as β_N crosses the region from 3.1 to 3.4. If this is found to be the case as more data is added to the database, it implies that the quench rate increases with β_N and thus the number of disruptions that can be tolerated during high performance plasma operations increases near and beyond the β_N where we would like to operate high performance ITER-FEAT plasmas. Note that the smallest quench rate found in DIII-D above β_N = 3.1 is 0.225 ms^{-1} or about a factor of 2 above the lowest quench rates seen with β_N < 3.0.

We also find that for plasmas with β_N > 3.5 the peak in the current quench rate typically occurs between 1–3 ms after the initiation of the I_p quench phase and the widths of the quench rate curves varies between 4 ms FWHM and 6.5 ms FWHM. The broader curves correspond to the smallest quench rates. The data suggests that either there is an anomalous processes involved in establishing the resistivity or the thermal evolution of the current quench plasma is essentially independent of the pre-disruptive plasma properties. The scatter in the data seems to indicate the existence of a highly nonlinear physics mechanism which has yet to be identified.

3.1.3.3. Axisymmetric Halo Currents Expected in ITER-FEAT Disruptions. The GA analytic halo current model has been applied to an ITER-FEAT "DIII-D AT" (wrs4) configuration using the growth rate of γ_N = 4.5 rad/s from Section 2 and core and halo resistivity inferred from the scaled current quench rate found in the DIII-D AT disruptions studied in the previous section (Section 3.2). Table IV shows the resulting peak poloidal halo current amplitudes for several choices of halo/core temperature. In all cases shown the halo and core were taken to have the same temperature and Z_{eff} = 1.0. Taking the core and halo plasmas to have the same temperature corresponds to a worst case assumption: a core hotter than the halo produces a reduced halo current. Halo current fraction (halo current divided by equilibrium plasma current) is also shown, along with the local stress which would be produced at the equilibrium value of major radius assuming a peaking factor of 1.0 (i.e., an axisymmetric halo current distribution). Peaking factors in DIII-D at the time of the peak halo current are typically less than 2.0, although other devices (notable Alcator C-Mod and ASDEX-U) have reported values as high as 4.0 [12]. The local stress is simply the product of the axisymmetric halo current amplitude and the peaking factor, so a peaking factor of two would double the values given in the table.

Table IV shows that the halo current expected in an unmitigated AT scenario disruption (with similar post-thermal quench characteristics to DIII-D AT disruptions) is relatively small. Such disruptions produce roughly 0.15–0.2 MPa of local stress with no toroidal peaking. Two different temperatures were used to produce this range, based on the range observed in DIII-D AT disruptions (Section 3.2).

An impurity gas puff mitigated disruption scenario is evaluated in the the third line of Table IV. In the case of Ar gas puff mitigation, the post-thermal quench electron temperature is estimated to be 1.3 eV with Z_{eff} of 1. In this case the halo current amplitude is reduced by approximately a factor of two or more from the unmitigated value (based on 15–18 eV).

TABLE IV
SUMMARY OF HALO CURRENTS EXPECTED IN ITER-FEAT "DIII–D AT" (wrs4) CONFIGURATION (Vertical Growth Rate = 4.5 rad/s, Z_{eff} = 1, I_p = 10 MA; peaking factor = 1.0)

Post-Thermal Quench T_e	Poloidal Halo Current	Halo Current Fraction (I_h/I_p)	Local Stress Due to $I_h \times B_T$
18 eV (γ_N = 14 rad/s, worst case)	1.3 MA	13%	0.18 MPa
15 eV (γ_N = 19 rad/s)	1.0 MA	10%	0.14 MPa
1.3 eV (= Ar mitigation)	0.53 MA	5.3%	0.07 MPa

Figures 26 through 28 show simulations of these VDE disruption cases in the ITER-FEAT AT configuration using the GA halo model. Note that in all cases the safety factor rises during the disruption, producing a small poloidal halo current relative to toroidal halo current through the relation

$$I_{\text{halo}}^{\text{poloidal}} = \frac{I_{\text{halo}}^{\text{toroidal}}}{q_{\text{halo}}} \quad .$$

The safety factor is artificially pinned at $q_{halo} = 5$ after it reaches that point in the simulations (if the peak halo current occurs before that point).

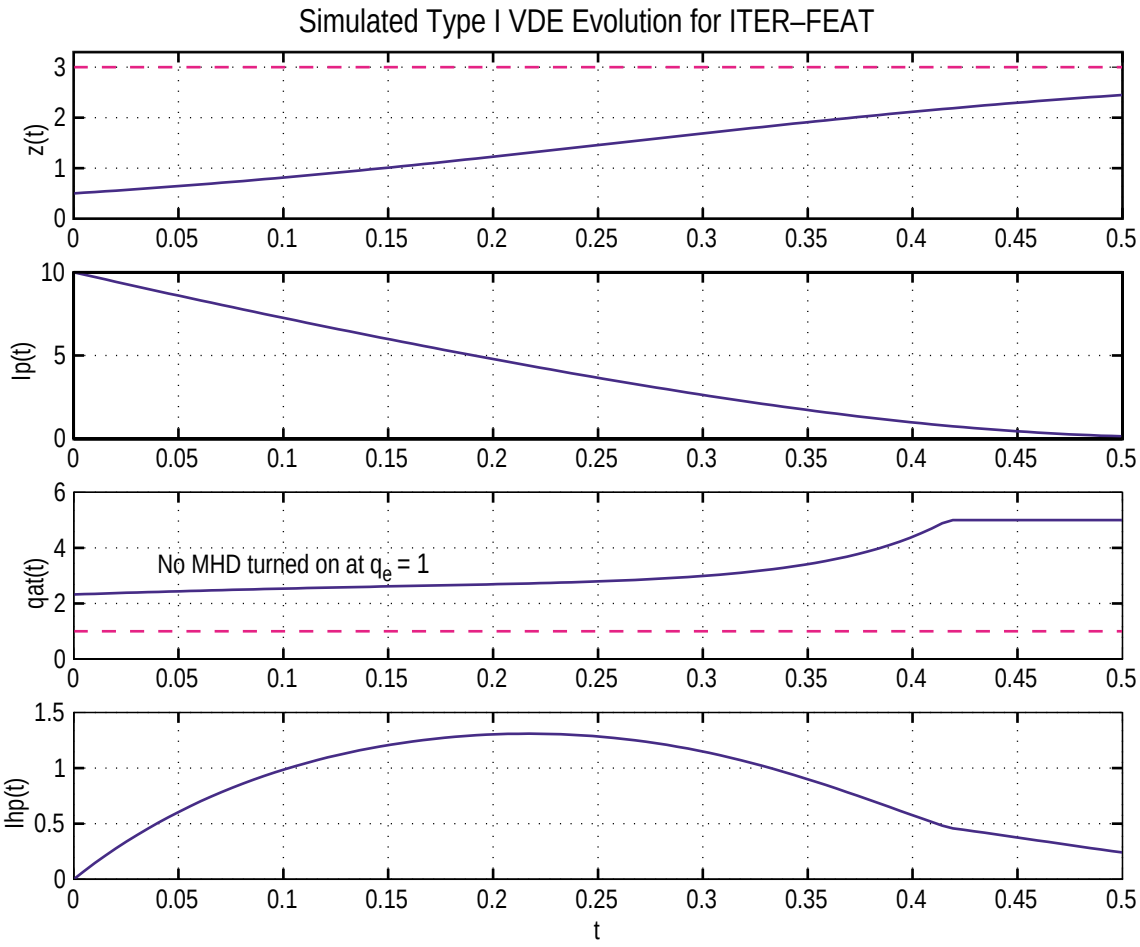

Fig. 26. Halo current history for ITER-FEAT AT case (wrs4) $T_e = 18$.

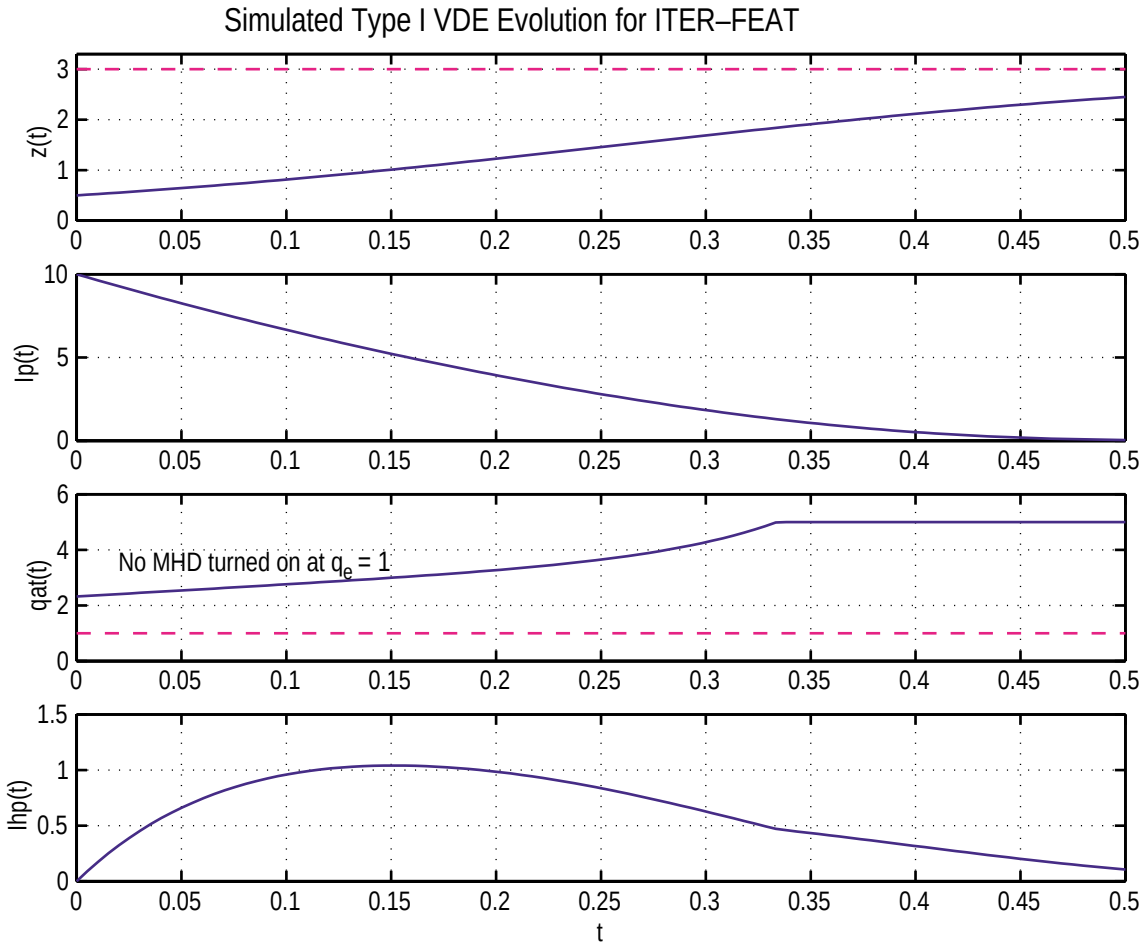

Fig. 27. Halo current history for ITER-FEAT AT case (wrs4) $T_e = 15$.

VDE disruptions in which the halo safety factor rises throughout are termed “Type I” in the classification system identified in [7]. Disruptions of the contrasting category, “Type II”, produce a reduction in halo safety factor to unity, at which point large amplitude MHD activity tends to increase the resistivity and cause the safety factor to rise thereafter. Type II VDE’s therefore tend to produce the largest poloidal halo currents.

Table V shows the same quantities calculated for the ITER-FEAT reference configuration, with 50% higher growth rate than the AT case, and with higher plasma current (but using the same resistivity as in the AT case). Higher plasma current and vertical growth rate result in both higher induced toroidal halo current (for the same core/halo decay rates) as well as lower edge safety factor at the time of peak halo current [7,8]. The lower safety factor then produces a higher poloidal halo current. The net result is that the reference configuration is expected to produce substantially greater halo current amplitudes, as confirmed by the disruption simulations summarized in Table V.

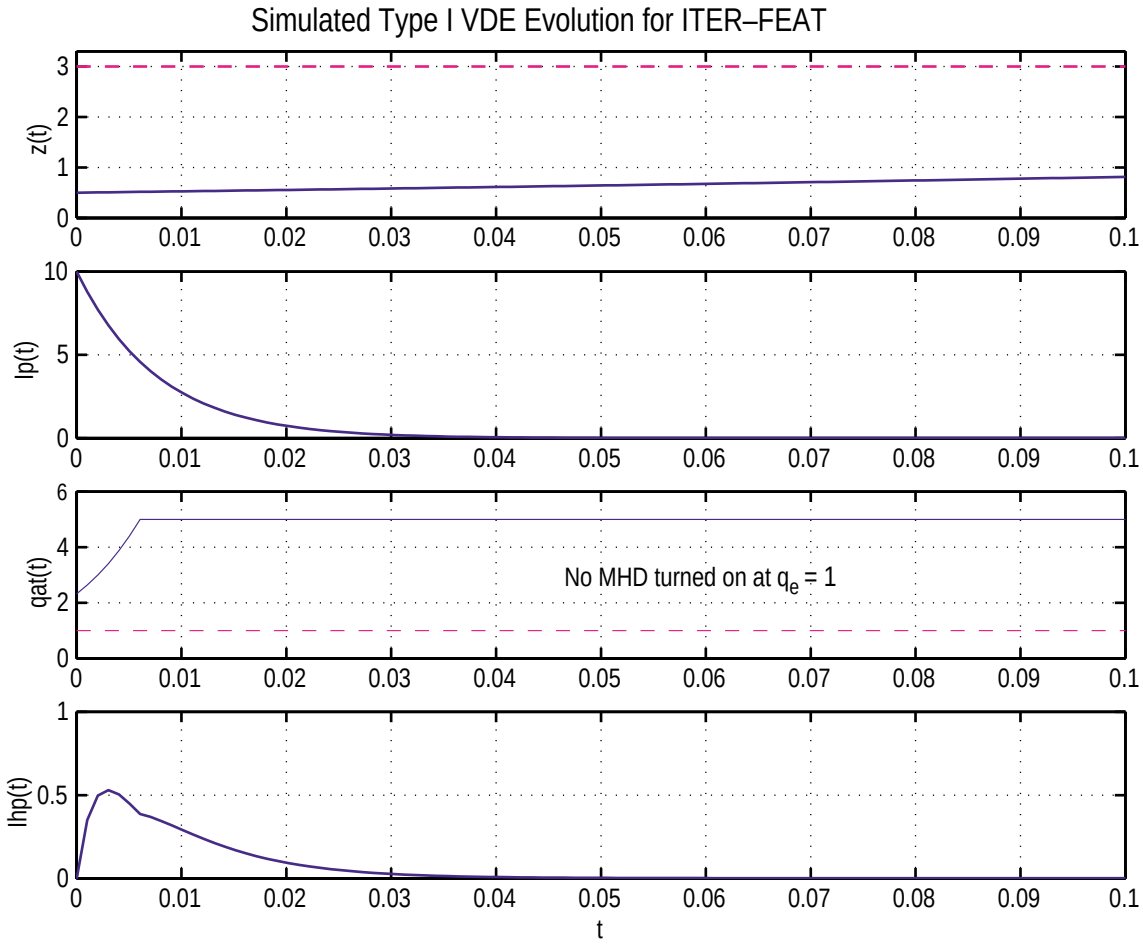

Fig. 28. Halo current history for ITER-FEAT AT case (wrs4) T_e = 1.3 (ar gas puff-mitigated disruption).

TABLE V
SUMMARY OF HALO CURRENTS EXPECTED IN ITER-FEAT REFEREBCE CONFIGURATION
(Vertical Growth Rate = 6.2 rad/s, Z_{eff} = 1, I_p = 15 MA; peaking factor = 1.0)

Post-Thermal Quench T_e	Poloidal Halo Current	Halo Current Fraction (I_h/I_p)	Local Stress Due to $I_h \times B_T$
20 eV	3.5 MA	23%	0.47 MPa
1.3 eV (- Ar mitigation)	1.2 MA	8%	0.16 MPa

Figures 29 and 30 show simulations of these VDE disruption cases in the ITER-FEAT reference configuration using the GA halo model. Note that in these cases also the safety factor rises during the disruption (although not as dramatically as in the AT cases). The reference configuration therefore produces Type I VDEs also (despite the higher growth rate), which is consistent with the low halo current fraction. Type I VDEs in

DIII-D tend to produce halo current fractions up to approximately 20%, while Type II VDEs can produce fractions as high as 35% [7,13].

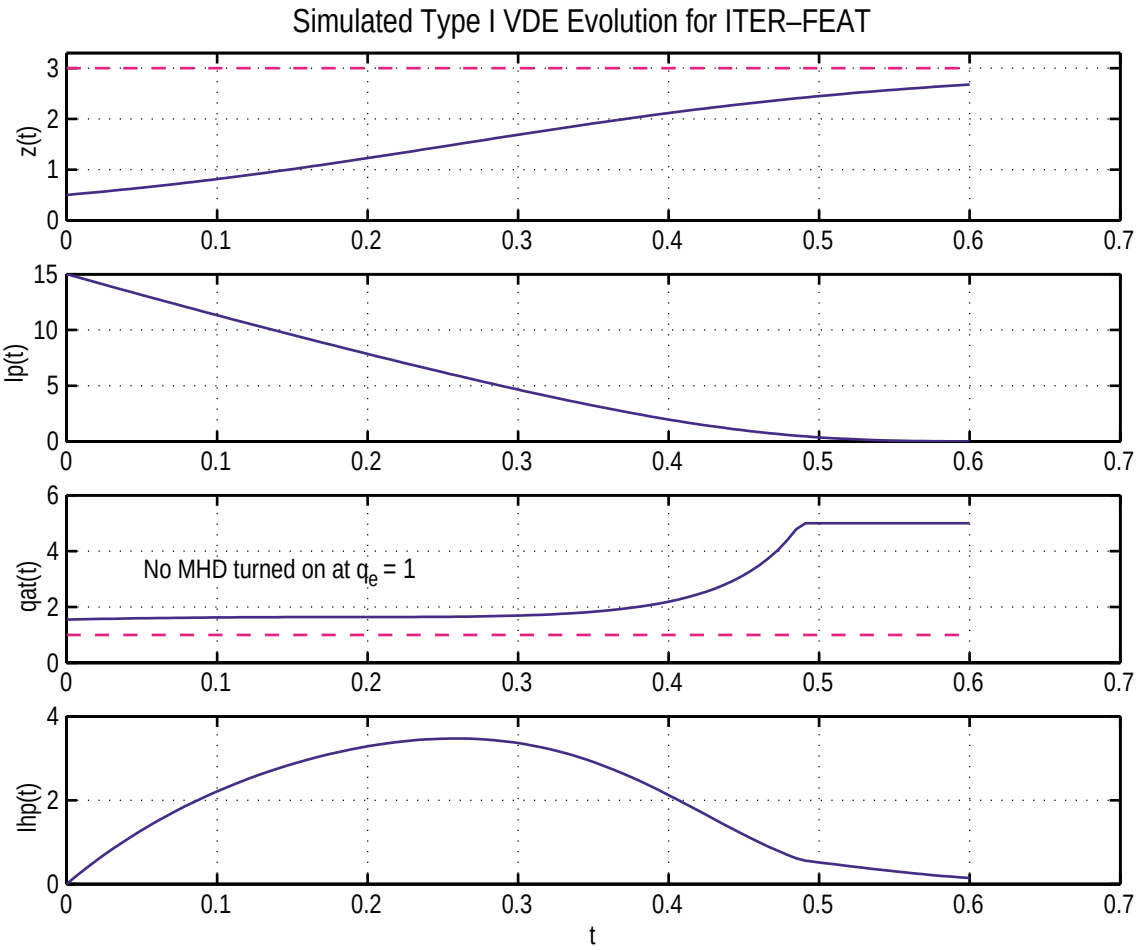

Fig. 29. Halo current history for ITER-FEAT reference case, T_e = 20.

3.1.4. SUMMARY AND CONCLUSIONS

Disruption halo currents expected in ITER-FEAT have been calculated using the GA analytic halo model and assumptions of post-thermal quench core and halo plasma characteristics based on DIII-D AT disruption experience. Because of the relatively low vertical growth rate calculated for the ITER-FEAT AT equilibrium and the low halo temperatures derived from DIII-D AT disruptions, the unmitigated peak (axisymmetric) poloidal halo current expected in ITER-FEAT AT disruptions corresponds to only 10%–13% of the plasma current. This in turn corresponds to approximately 0.2 MPa of local stress due to $I_{halo} \times B_{tor}$ forces. A toroidal peaking factor of two would double this local stress. Mitigation by Ar gas puff can reduce the halo current fraction to 5% of the plasma current, with a corresponding reduction in local stress. Impurity mitigation of disruptions

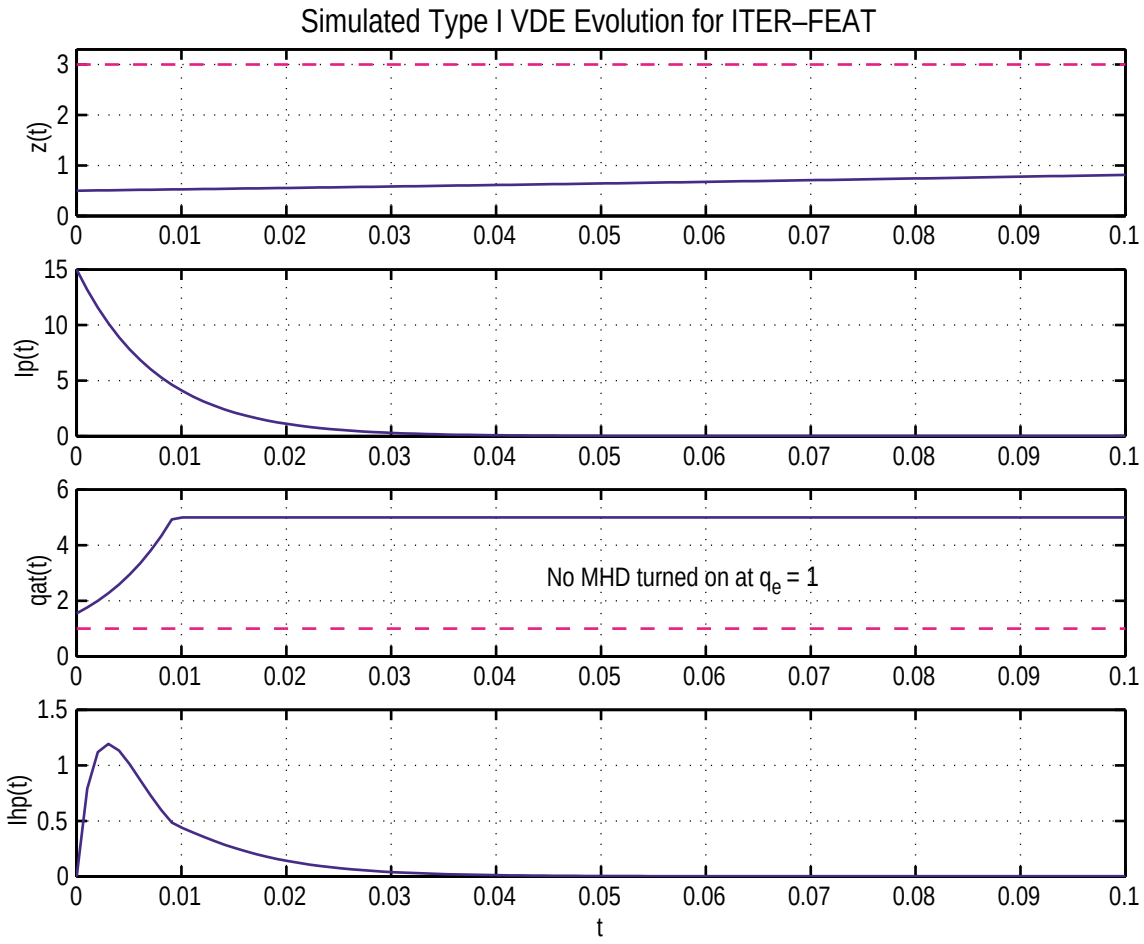

Fig. 30. Halo current history for ITER-FEAT reference case, T_e = 1.3 (Ar gas puff-mitigated disruption).

tends to reduce the peaking factor to near unity [13]. For comparison, the unmitigated peak poloidal halo current expected in ITER-FEAT reference equilibrium VDEs (for the same post-thermal quench resistivity) is approximately 23%, corresponding to approximately 0.5 MPa of local stress. Ar gas puff mitigation of these scenarios can reduce this halo current fraction to approximately 8%.

It is not clear from outside the project what the ITER-FEAT design team has concluded regarding tolerable halo current and eddy current loads. However, several point design presentations (e.g. [14]) report "eddy current and halo current" loads up to "10^4 tonnes", suggesting total forces on the order of 100 MN. This is roughly consistent with total VDE loads calculated in the ITER FDR device, but it is not entirely clear if this refers to the combined forces of eddy currents and halo currents, and how this force is distributed about the conducting structure. If this force were evenly distributed around the (inner) vacuum vessel and taken to be normal to the wall everywhere (not quite relevant to VDE or halo current forces, but useful as a reference choice), the resulting stress would

be approximately (100 MN)/(1100 m^2), or roughly 0.1 MPa. This value is comparable to the values found in *mitigated* scenarios in the present study, suggesting that reliable mitigation may be extremely important in ITER-FEAT.

3.1.5. APPENDIX 1: PROJECT INFORMATION

Requestor: V. Chan

Shots: See Reference [9].

Codes: uscws9:/users/humphrys/matlab/halo/general_halosim.m
nitron:/u/humphrys/corsica/iter/*.bas
nitron:/u/humphrys/corsica/iter/wrs1201/*.bas

3.2. LOW n KINK STABILITY FOR AT EQUILIBRIA

Stability calculations were performed for the n=1, n=2, and n=3 ideal kink modes for the three Advanced Tokamak equilibria with the H-mode pedestal and increasing triangularity. For the n=1 mode, all three equilibria were unstable without a wall but stabilized by the ITER FEAT wall. The instabilities in the case of no wall were global pressure-driven kink modes typical of equilibria exceeding the n=1 kink β limit. Figure 31 shows the mode structure for the standard triangularity equilibrium; the others are similar.

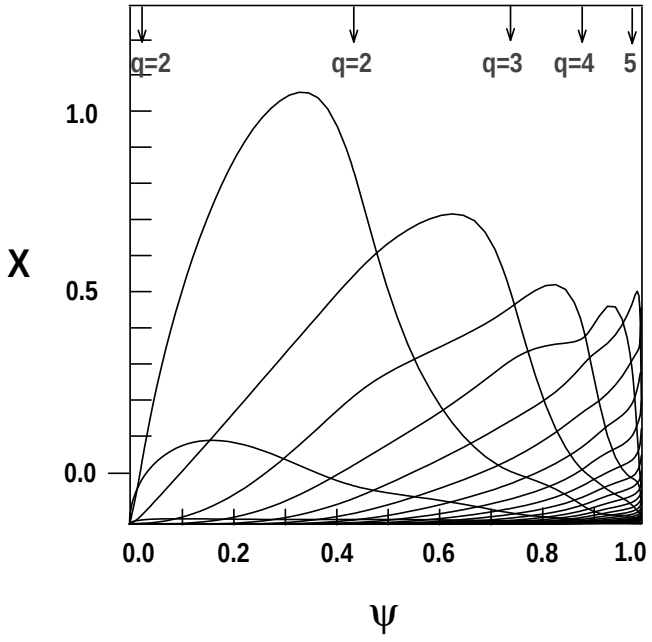

Fig. 31. Mode structure for n=1 standard equilibrium (without wall).

Scans were performed in which the wall was expanded uniformly to determine the margin of stability. The results are shown in Fig. 32. This shows there is a margin of at least 20% in the wall position (i.e. the wall could be expanded by 20% while maintaining stability) and that the margin increases with increasing triangularity, though this increase is quite moderate.

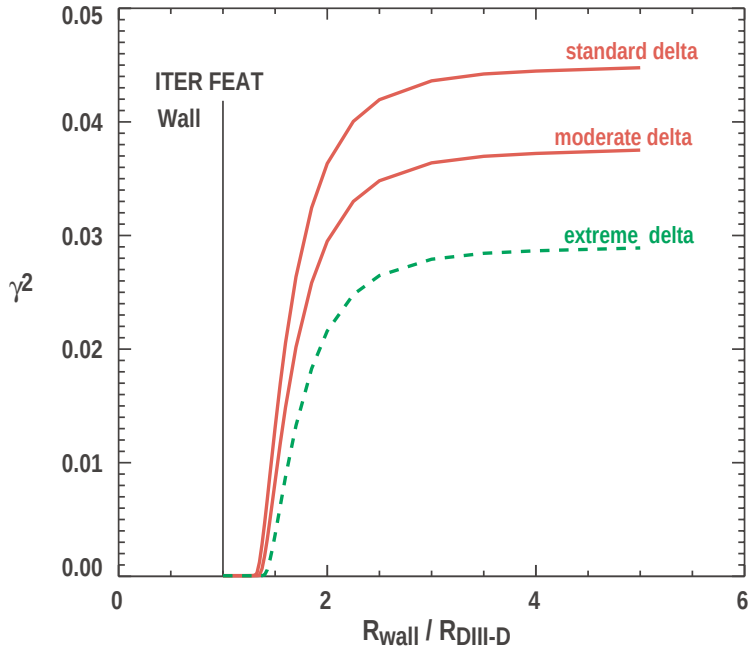

Fig. 32. Growth rate vs. wall distance — ITER-FEAT: δ scan n=1.

The stability calculations for the n=2 and n=3 modes also show stability with the ITER-FEAT wall for all three triangularity values. For the standard triangularity, the n=2 mode is unstable with no wall but initial indications are that the n=2 modes for the two higher triangularity equilibria are stable even without a wall. This is still being confirmed by mesh convergence studies. Also, the initial indications are that the n=3 modes in all three cases are either stable or close to being stable without a wall.

3.3. EDGE STABILITY AND PEDESTAL CONSTRAINTS

The MHD stability of H-mode ITER-FEAT equilibria has been evaluated using the ELITE code [15,16]. ELITE is a new, highly efficient numerical tool for calculating MHD stability thresholds, mode structures and growth rates of modes with intermediate to high toroidal mode number ($n \gtrsim 5$). ELITE has been successfully benchmarked against the GATO and MISHKA codes, and has been used to explore tokamak edge stability, and

to develop models of ELMs and constraints on the H-mode pedestal, as described in Refs. [15,16].

As discussed in the transport section of this report, the temperature at the top of the H-mode pedestal ("pedestal height") plays a very important role in determining the quality of core plasma confinement and overall fusion performance. MHD instabilities can be driven by the sharp pressure gradients and consequent large bootstrap currents in the pedestal region. These instabilities place constraints on the achievable pedestal height, as well as driving edge localized modes (ELMs) which place important heat load constraints on the divertor.

The reference ITER-FEAT equilibrium has smooth edge profiles without an edge pedestal, hence a pedestal must be added in order to assess edge stability in the H-mode regime. In order to assess edge stability constraints on the ITER-FEAT pedestal we have constructed a set of equilibria in which hyperbolic tangent shaped density and temperature pedestals of varying width are added to the reference equilibrium. The collisional bootstrap current driven by these profiles is calculated self-consistently using the Sauter model. The stability of these equilibria to n=10,20,30 modes is then assessed with the ELITE code. Figure 33 shows the maximum stable pedestal temperature as a function of the width of the pedestal (the density and temperature widths are taken to be equal for this study). The diamonds show the T_{ped} limit with the prescribed edge temperature/density ratio from the ITER-FEAT design. Note that the T_{ped} limit as a function of width is not a straight line. This is because the finite-n peeling-ballooning modes which limit pedestal stability are sensitive to both the local p' and to the pedestal width (unlike infinite-n ballooning modes which feel only the local gradient). Note that in the range of pedestal width (~5%) expected from empirical scalings, the allowed pedestal height (~4 keV) is sufficient for good performance, and note also that if the width is in fact narrower than expected, the reduction in the T_{ped} limit is sub-linear. Furthermore, the stability limit on T_{ped} can be increased by decreasing the edge density, but this involves tradeoffs with divertor design and may impact overall performance if the core density is reduced as well.

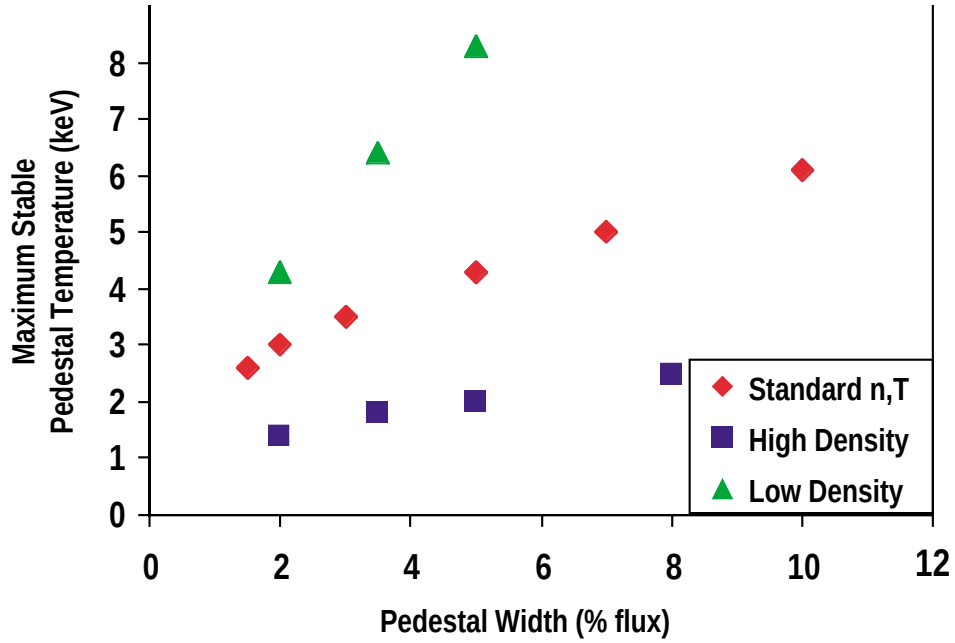

Fig. 33. The maximum pedestal temperature stable to n=10, 20, 30 modes calculated by ELITE is plotted as a function of the pedestal width. Diamonds show equilibria with the edge density specified in the standard ITER-FEAT equilibria. Higher stable T_{ped} can be achieved at lower density, as shown by the triangles.

Advanced Tokamak (AT) equilibria have also been constructed for this study, with three different values of the plasma triangularity (δ). These equilibria include an H-mode pedestal, and their stability to n=6–30 MHD modes has been assessed with ELITE. Normalized growth rates as a function of n are shown in Fig. 34. At the lowest value of $\delta = 0.375$, edge localized MHD modes are found to unstable with significant growth rates, with the largest growth rate for n~10. Increasing δ is found to significantly stabilize these modes and thus allow higher stable pedestals.

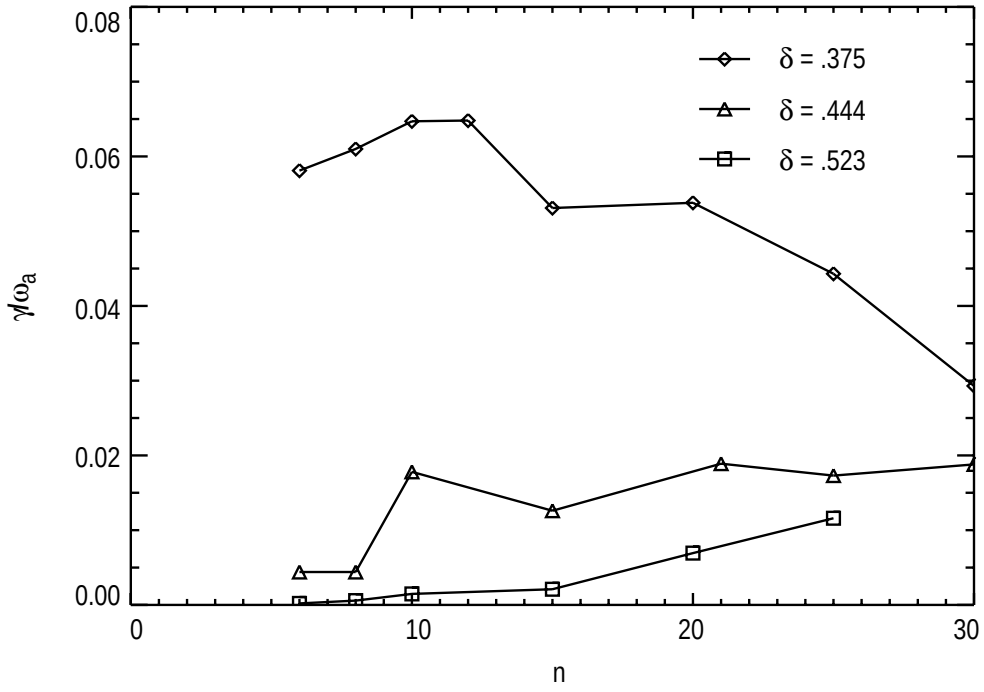

Fig. 34. The normalized ideal MHD growth rate as function of toroidal mode number (n) is shown for the AT equilibria at three values of the plasma traingularity (δ).

3.4. STABILITY TO THE RESISTIVE WALL MODE AND ITS STABILIZATION BY PLASMA ROTATION

An equilibrium approximating that proposed for the ITER-AT target equilibrium *iter.wrs.d3d.4.129.gfile* has been tested for its stability to the RWM and stabilization of the RWM by plasma rotation by using the MARS stability code. The equilibrium is obtained from *iter.wrs.d3d.4.129.gfile* first by up-down symmetrization so that it becomes a double-null configuration. Its beta value is then adjusted with fixed $\langle j \cdot B \rangle$ profile so that the ideal external wall stability location for the external kink mode is at r_w/plasma radius = 1.5. Consequences of this modification of the equilibrium are: the q profile has its minimum slightly above 2; and the q value increases relatively quickly to a large value near the plasma edge. The increasing q region covers a relatively large portion of the plasma volume.

MARS code is a linear eigenvalue code, which solves for the full MHD perturbation equations with the MHD mode frequency as the eigenvalue and the perturbed MHD quantities (plasma velocity, magnetic field and pressure) as eigenfunctions. One of the most important input quantities in the present study is the plasma rotation profile. Because there is a lack of information on the expected rotation profile, we assume the rotation profile is similar to one of the discharges in DIII-D RWM experiments, i.e. shot 106029 at 1500 ms.

The model for the damping of the toroidal momentum used is the sound wave damping model. In this model, there is a force, which damps the perturbed toroidal motion of the mode according to the formula

$$F_{\mathrm{SD}} = -\kappa_{\|}\sqrt{\pi}\left|k_{\|}v_{\mathrm{th}}\right|\rho\vec{v}\bullet\hat{b}\hat{b} \quad .$$

Here $\kappa_{\|}$ is a numerical coefficient with a value of 0.89 to model the ion Landau damping process, $k_{\|}$ is the parallel wave number $(m-nq)/R$, v_{th_i} is the ion thermal velocity, ρ is the mass density, $\vec{v}$ is the perturbed plasma velocity and $\hat{b}$ is the unit vector of the equilibrium magnetic field. This value of $\kappa_{\|}$ is adopted because it has been tested in a previous analysis of experimental results in DIII-D to best fit the experimental data.

Major results from the numerical investigation indicates that the critical rotation velocity required for the stabilization of the resistive wall mode for this equilibrium is smaller than that computed previously for ARIES *g099728.00270*. The detailed reason is not completely understood. But by comparing the present RWM eigenfunction with those obtained previously, we could attribute this to the fact that:

1. There are more rational surfaces participating in damping the sound wave.

2. The eigenfucntion is also more concentrated at the plasma central region rather than at the plasma edge —near the plasma center, the beta is higher, and the same singular surface will be able to more strongly damp the RWM via sound wave damping.

As noted before both of these two points are related to the q profile and the β_N value of the equilibrium. The critical rotation frequency at the plasma center for stabilization of the RWM in this equilibrium is found to be between 0.008 to 0.012 of the Alfvén transit frequency. No stability window is found for rotation frequency below 0.008. The stability window for the location of the resistive wall is between 1.2 and 1.5 times the plasma radius when the central plasma rotation frequency is at 0.012 of Alfvén frequency. This window widens to between 1.0 to 1.5 times the plasma radius when the central rotation frequency is increased to 0.016 of the Alfvén frequency. In here, the Alfvén frequency is defined as

$$f_{\mathrm{av}} = \frac{v_{\mathrm{A}}}{R} \quad ,$$

R is the plasma major radius, taken to be 6.34 meter and the Alfvén velocity is

$$v_A = \frac{B_{vac}}{\sqrt{\mu_0 \rho_0}} \quad ,$$

and B_{vac} is 5.3 T. The resistive wall time has been taken to be 4000 τ_a.

These results are also shown in the following figures. Shown in Fig. 35 is the mode amplitude of the various poloidal Fourier harmonics of the radial magnetic perturbations of the resistive wall mode in this equilibrium as a function of $\sqrt{\psi}$, with ψ being the fraction of the total amount of poloidal flux enclosed by the flux surface. It is observed that this mode has quite a global structure. Shown in Fig. 36 is the growth rate of the resistive wall mode as a function of the location of the resistive wall. Each curve has a different plasma central rotation frequency relative to the resistive wall. The same equilibrium is used here as in Fig. 35.

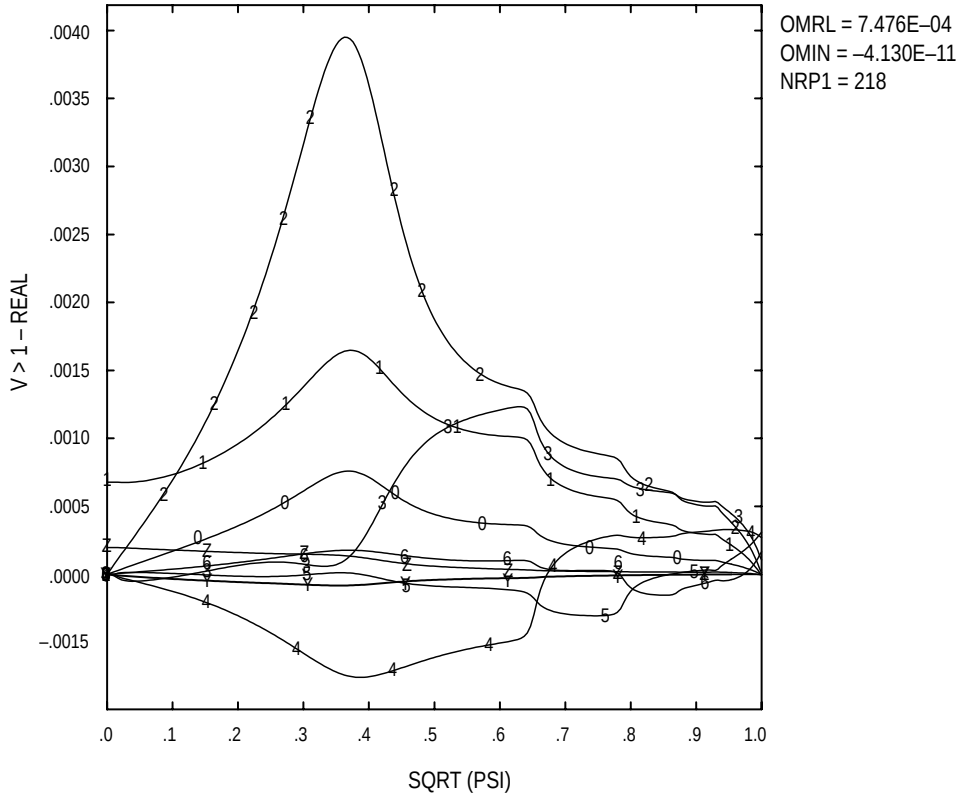

Fig. 35. Amplitudes of the poloidal harmonics of the perturbed magnetic field ξ_ψ of an un-stabilized resistive wall mode. Here ξ_ψ is plotted as a function of $\sqrt{\psi}$ for the equilibrium.

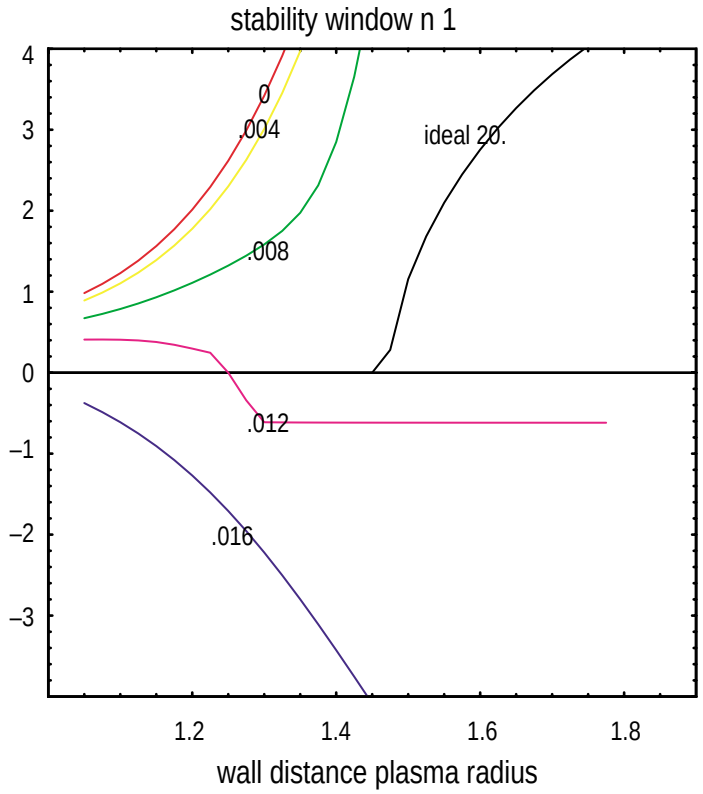

Fig. 36. Stability window of RWM vs. wall Location. Rotation profile from DIII-D experiment Shot 106029 at 1500 ms is used. Plotted are growth rates of the ideal and resistive wall modes vs. r_w. The curve labeled ideal is the growth rate of the ideal external kink with the scales multiplied by 200. Other curves are labeled by the rotation frequency of the plasma center measured in units of the toroidal Alfven transit frequency. The growth rates of the resistive wall modes are multiplied by τ_w.

To understand the results in Fig. 35 better, we also performed the stability analysis for the case of a rigid plasma rotation. This is a viable scenario, because recently there was research activity on the possible utilization of a rotating (flowing) liquid wall.

Shown in Fig. 37 (reswall.rig.ps) are the results for rigid plasma rotation.

Comparing Fig. 37 with the non-uniform rotation case of Fig. 36, we note that the required rotations at the plasma center do not differ by a large factor. This confirmed our hypothesis that the rotation requirement for stabilization is related to the structure of the eigenfucntion, i.e., the eigenfunction is peaked towards the central part of the plasma, where the damping is strong. Nevertheless, the uniform rotation model is still more effective than a profiled rotation, indicating that the sum of the effect of the higher q surfaces still carry a larger portion of the weight in damping the RWM.

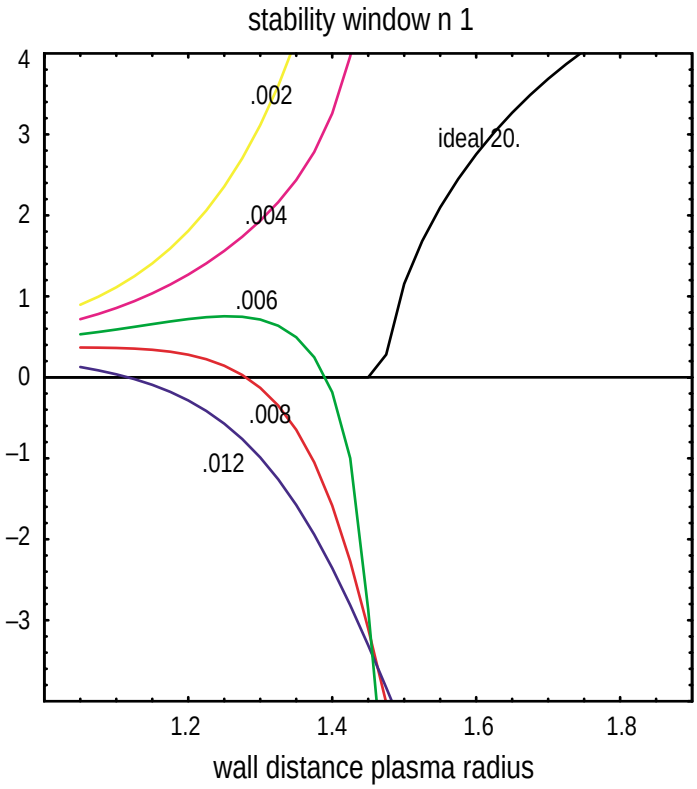

Fig. 37. Stability window of RWM vs. wall location. Rigid rotation profile. Plotted are growth rates of the ideal and resistive wall modes vs. r_w. The curve labeled ideal is the growth rate of the ideal external kink with the scales multiplied by 200. Other curves are labeled by the rotation frequency of the rigid plasma rotation measured in units of the toroidal Alfven transit frequency. The growth rates of the resistive wall modes are multiplied by τ_w.

4. TRANSPORT MODELING AND CONFINEMENT REQUIREMENTS

4.1. NEUTRAL BEAM REQUIREMENT FOR ROTATION CONTROL

4.1.1. Summary

An AT type ITER-FEAT discharge scaled up from DIII-D shot 106029 was analyzed for RWM stability. The scaled up discharge has density $\approx n_{GW}$, with $\beta_N H(89p) = 8.46$, $Q_{DT} = 20.3$, with 33 MW of 1 MeV negative neutral beam injection. Primary and impurity ion densities and (electron and ion temperature profiles were determined in such a way as to be consistent with the MHD equilibrium pressure and the fast alpha and neutral beam stored energy densities. It is shown that 33MW of neutral beam injection is sufficient to maintain the central toroidal rotation speed at 2×10^4 rad/s using ion power balance diffusivity for the momentum diffusivity. According to Ref. [17] the required central rotation speed for RWM stability is about 1.52×10^4 rad/s.

4.1.2. Generating Profiles Consistent With MHD Equilibrium Pressure Profiles

In evaluating the application of neutral beam injection for rotation control of ITER-FEAT, DIII-D H mode shot 106029 was used to determine an equilibrium which could be used as a basis for further studies. This work is described in Ref. [18].

For transport analysis we would like to maintain the pressure profile in this scaled up equilibrium, identified by ¢*iter_wrs_d3d*_4_129.*gfile*¢. Thus we have to find densities and temperatures which are consistent with the assumed equilibrium pressure profile and which yield sufficiently attractive performance parameters. In the present work this was accomplished by assuming an electron density profile, see Fig. 38, at approximately 1.0 times the Greenwald limit. To determine the primary ion and impurity densities and the electron and ion temperatures (assumed equal for this study) we consider the equations for charge neutrality, z_{eff}, and equilibrium pressure together with auxiliary information necessary to solve the following set of equations:

$$n_e - Z_{p1}n_{p1} - Z_{p2}n_{p2} - Z_{impl}n_{impl} - Z_{imp2}n_{imp2} = Z_b n_b + Z_\alpha n_\alpha \quad , \tag{1}$$

$$Z_{eff}n_e - \left\langle Z_{pl}^2 \right\rangle n_{p1} - \left\langle Z_{p2}^2 \right\rangle n_{p2} - \left\langle Z_{impl}^2 \right\rangle n_{impl} - \left\langle Z_{imp2}^2 \right\rangle n_{imp2} = Z_b^2 n_b + Z_\alpha^2 n_\alpha \quad , \tag{2}$$

$$n_e C_e T_e + n_{p1} C_i T_i + n_{p2} C_i T_i + n_{impl} C_i T_i + n_{imp2} C_i T_i = P - \frac{2}{3}\left(w_{beam} + w_\alpha\right) \quad , \tag{3}$$

$$Z_{\mathrm{frac}} n_{\mathrm{p1}} - n_{\mathrm{p2}} = 0 \quad , \tag{4}$$

$$Z_{\mathrm{impfrac}} n_{\mathrm{p1}} - n_{\mathrm{imp2}} = 0\,\mathrm{P} - \frac{2}{3}\left(w_{\mathrm{beam}} + w_{\alpha}\right) \quad . \tag{5}$$

Here we assume two primary (i.e., hydrogenic) ions and two impurities with the last two equations specifying the amounts of the second species in each case. We further assume that the beam and a densities and stored energy densities are given. This implies that an iterative process is required to solve the linear set of equations since beam deposition and fusion rates depend on the unknown densities and temperatures. *P* is the known pressure profile from the equilibrium calculations. We take the electron density profile is known which eliminates the first of the equations Eq. (1). The above set of equations applies at each value of the minor radius grid ρ. The parameters multiplying the electron and ion temperatures, C_{e},C_{i} are set to unity if the electron density is solved for as part of the above equation set. Otherwise C_{e},C_{i} are automatically adjusted at each radius in such a way that the error in Eq (1) is minimized. Typically we want to fix the electron density at a specified value so the later case is generally the one that arises.

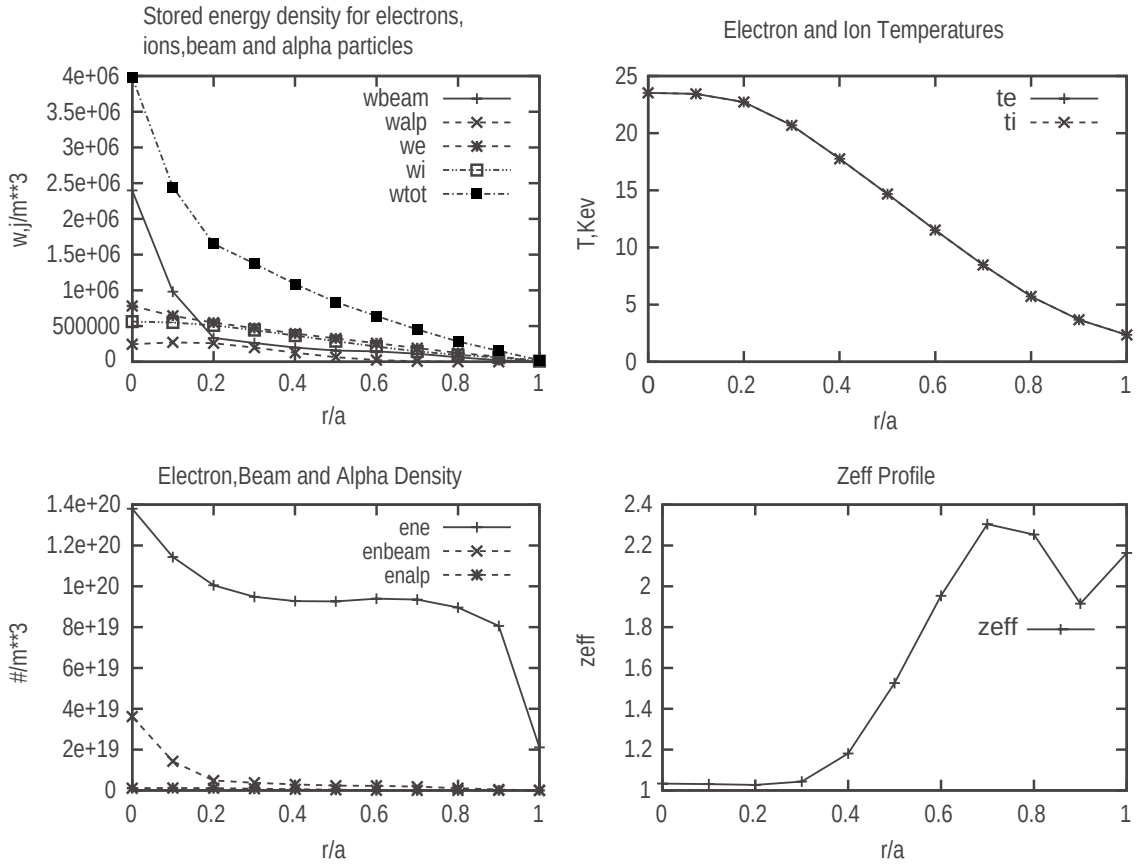

Fig. 38. The profiles used to deduce the electron temperature and primary and impurity ion densities as described in the text.

4.1.3. Neutral Beam Injection

Due to the large densities involved, sufficient penetration for neutral beam heating and current drive requires a high energy beam. We have assumed a 1 MeV (negative ion) D-T beam with injected power of 33 MW. The deposition profile for the beam is given in Fig. 39. A visual indication of the fast ion birth points in the plasma in cross section and top views is given in Figs. 40 and 41 respectively. For the tangential injection shown shine through is essentially zero.

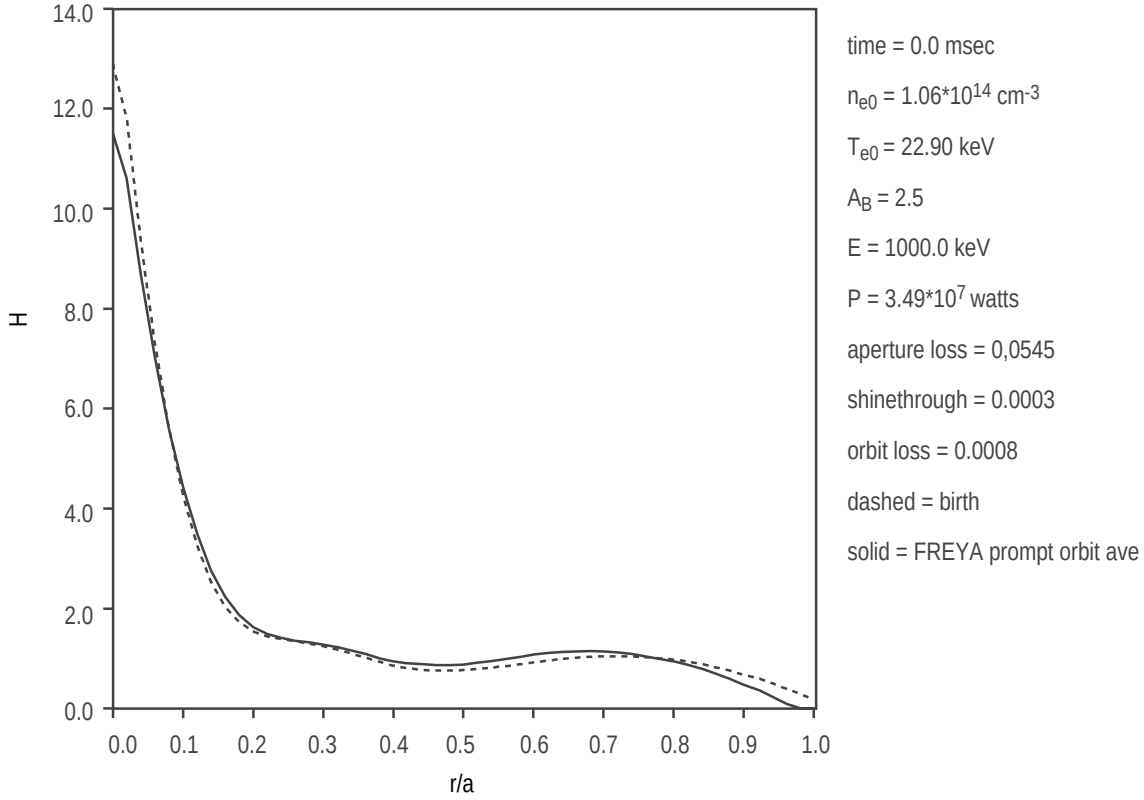

Fig. 39. The fast ion birth profile for 1 MeV negative ion injection. The dashed line represents the birth profile and the solid line, which was used in the calculations, represents a prompt orbit average result. Due to co-injection the prompt orbit average results is shifted inward at the plasma edge. Near the magnetic axis the decrease in H is due to finite banana width effects.

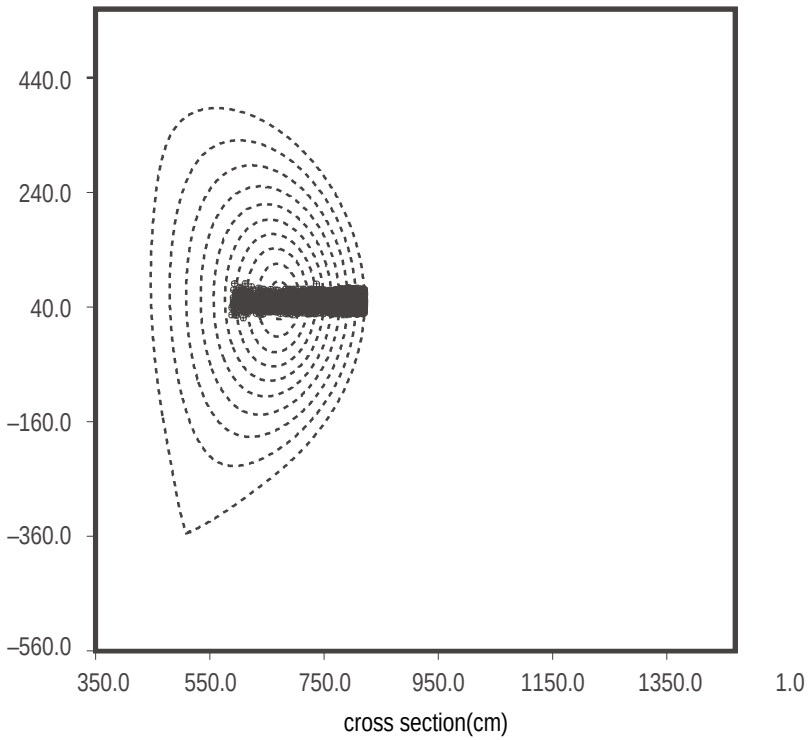

Fig. 40. Illustration of fast ion deposition in cross sectional view. The beam was focused for approximately 60 cm injection width at the magnetic axis.

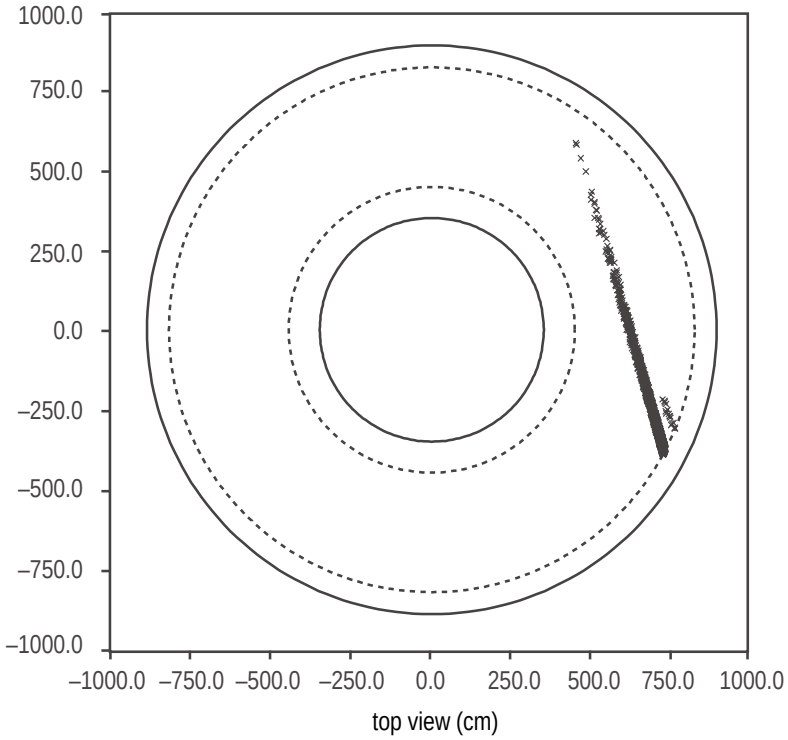

Fig. 41. Top view of approximately tangential injection. Some optimization with respect to current drive could be done but was not attempted here since the results are preliminary in nature at best

4.1.4. Transport Analysis

The primary question to be addressed here is the stabilization of resistive wall modes. To accomplish this stabilization we need to ensure that the plasma is spinning sufficiently rapidly. Analyses done by M.S Chu, Ref. [17], indicated that a value of 15% of the observed central toroidal rotation speed value in DIII-D shot 106029 was sufficient to stabilize the largest mode amplitude which occurred at the magnetic axis. The DIII-D rotation speed profile was scaled up by maintaining the same fractional central Alfvén speed in the scaled up discharge. This leads to a toroidal rotation speed profile shown as the solid line in Fig. 42.

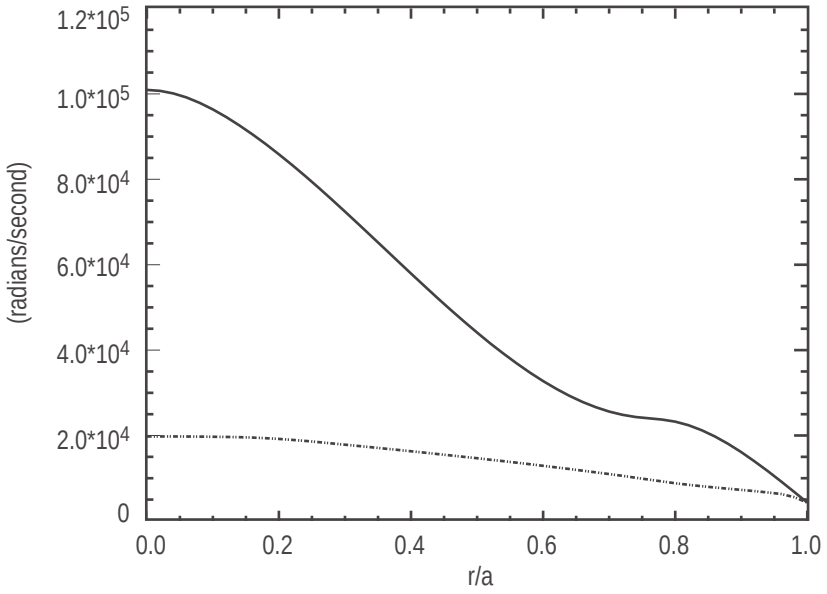

Fig. 42. The initial (solid line) and steady state (dashed line) rotation speed profile. A central value greater than about 1.5×10^4 is required for RWM stability according to Ref. 2t

To determine the balance between neutral beam torque input and drag and momentum diffusion we have to solve the toroidal momentum balance equation. This equation requires that we specify a momentum diffusivity. Since the determination of the plasma kinematic viscosity from theoretical principles does not match experimental results we are forced to use alternative means to determine the momentum diffusivity. An often used criterion is to assume that the toroidal momentum diffusivity is equal to the ion diffusivity. We have adopted this method as well and further simplified the problem by using a power balance diffusivity for the ions. With the electron and ion temperatures determined consistently with the equilibrium pressure as described in Section 1, we obtain the power balance diffusivity given in Fig. 43. For orientation the ion neoclassical diffusivity is also indicated.

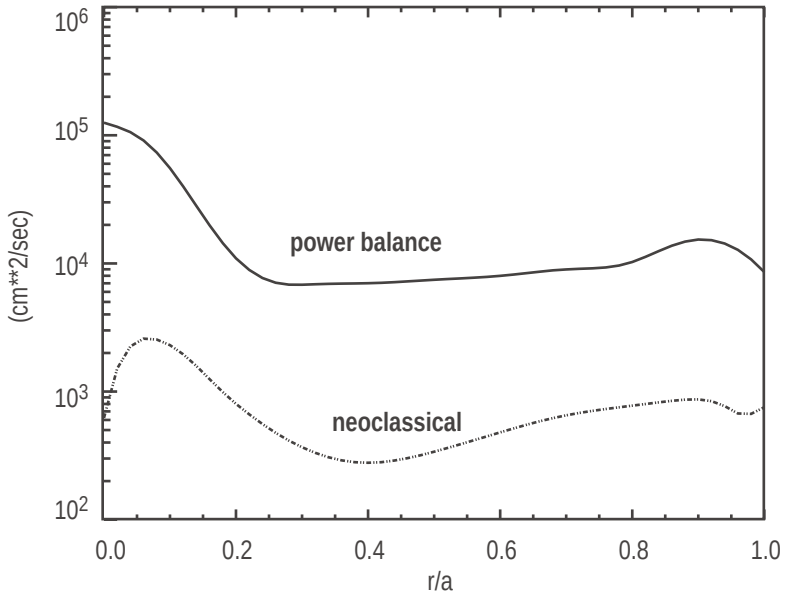

Fig. 43. The power balance ion diffusivity as a function of normalized minor radius. This profile (fixed in time and space) was used as the momentum diffusivity in the toroidal rotation speed calculations as well. Also shown (for purposes of orientation) is the ion neoclassical diffusivity.

With the given (fixed in time and space) power balance diffusivity we find that the toroidal rotation speed profile can be maintained at a level higher than required for resistive wall mode stabilization which, in accordance with Ref. [17],is assumed to be 15% of the central value. In Fig. 42 we show the rotation speed profile for a neutral beam injected power of 33 MW. The rotation speed profile is in steady state at the time shown. The central value of 2.0×10^4 is higher than the required value of about 15% $(1.0\times10^5) = 1.5\times10^4$ rad/s for stability.

Table VI represents a summary of the transport results. It should be noted that beam-beam fusion reactions were not included in the analysis.

4.2. TRANSPORT MODELING WITH GLF23

The GLF23 transport model is similar in design to the Weiland transport model. The GLF23 model computes approximate driftwave eigenfunctions for ion temperature gradient modes (ITG), trapped electron modes (TEM) and electron temperature gradient modes (ETG). The eigenfunctions are found using the gyrofluid equations and trial wavefunctions chosen to give a good fit to the growth rates computed with an exact gyrokinetic linear stabilty code. The transport due to these driftwaves is modeled by summing up the quasilinear fluxes for a spectrum of unstable modes weighted by a

TABLE VI
TRANSPORT ANALYSIS SUMMARY ITER-FEAT H–MODE (106029 Extrapolation)

Minor radius a (cm)	187.0	b/a:	1.98	
Nominal R major (cm)	620.0	R at geom. cent. (cm)	634.1	
R at mag. axis (cm)	672.9	Z at mag. axis (cm)	51.9	
Volume (cm^3)	7.88×10^{8}	Pol. circum. (cm)	1804.9	
Surface area (cm^2)	6.89×10^{6}	Cross section area	2.04×10^{5}	
B_T (G)	5.30×10^{4}	I_p (a)	1.00×10^{7}	
B_T at R_{geom} (G)	5.18×10^{4}	R (q=1)/a	0 00	
Line-avg den ($1/cm^3$)	9.09×10^{13}	τ-particle-dt (s)	0.20-	
$n_{GW} = 1x10^{14}$				
Profiles	Ucenter	Uedge	Ucen/Uav	
Elec. den ($1/cm^3$)	1.06×10^{14}	2.11×10^{13}	1.25	
Elec. temp (keV)	23.53	2.34	2.20	
Ion temp (keV)	23.53	2.34	2.20	
Current (A/cm^2)	52.08	51.34	1.05	
Z_{eff}	1.05	2.16	0.58	
q	2.52	9.34		
q* at edge		4.92		
Ang. speed (1/s)	1.98×10^{4} exp	14.30×10^{3} code	1.66×10	
Surface voltage (V)	0.00	0.00		
Average voltage (V)	0.00	0.01		
Ohmic power (W)	0.0×10	9.27×10^{4}		
Beam power-torus (W)	3.30×10^{7}	3.30×10^{7}		
Neutron rate (#/s)	0.0×10	7.05×10^{17}		
Computed quantities				
Beam power elec. (W)	$2.0x10^{7}$	ke at a/2 (1/cm-s)	1.15×10^{18}	
Beam power ions (W)	1.27×10^{7}	ki at a/2 (1/cm-s)	5.66×10^{17}	
Beam power cx loss (W)	$3.8x10^{3}$	ki/kineo at a/2	20.72	
Shinethrough (%)	0.02	χ electrons at a/2	1.27×10^{4}	
Rf power absorbed	0.0×10	χ ions at a/2	7.07×10^{4}	
Radiated power (W)	2.0×10^{7}	$R^*/a\ T_e = [T_e(0) + T_e(a)]/2$	0.56	
Poloidal B field (G)	6.96×10^{3}	β-poloidal	1.868	
Beam torque (nt-m)	4.45×10^{1}	Total torque (nt-m)	-3.25×10^{2}	
Stored ang mtm ($kg*m^2/s$)	3.18×10^{2}	Momt inertia ($kg*m^2$)	1.10×10^{-2}	
	Electrons	Ions	Thermal	Total
Stored energy (J)	1.837×10^{8}	1.644×10^{8}	3.480×10^{8}	4.08×10^{8}
DE/dt (W)	1.238×10^{4}	3.576×10^{6}	1.238×10^{4}	1.238×10^{4}
Input power (W)	1.178×10^{8}		1.661×10^{8}	1.661×10^{8}
Energy conf. time (s)	1.5589		2.0950	2.4561
Ang. momentum confinement time (s)			2.4356	
b-toroidal	Volume-avg	Center		
Electrons	1.451×10^{-2}	3.742×10^{-2}		
Ions	1.299×10^{-2}	$3.498v10^{-2}$		
Beam	$1.101x10^{-3}$	$1.780v10^{-2}$		
Alphas	3.638×10^{-3}	1.866×10^{-2}		
Total	3.224×10^{-2}	1.089×10^{-1}	H(89p) =	2.81
β_N*H(89p)	8.46			
Total power input (MW)	3.30×10^{7}	Time =	1.20×10	
I_{tot} =	1.0×10^{6}	I_{ohm} =	3.19×10^{6}	
I_{boot} =	4.88×10^{6}	I_{beam} =	1.93×10^{6}	
I_{ref} =	0.0			
Q_{DD} =	0.023998	Q_{DT} =	20.320179	
Q_{TT} =	0.037929			
Beam-beam fusion rate neglected !				

fluctuation amplitude function chosen to approximate the transport computed with a full 3D non-linear simulation of the turbulence. The original model was fit only to more exact theory without reference to experiment (1996). The non-linear simulations used in the fitting were based on the gyrofliud approximation. Since the original model was published, it has been discovered that the gyrofluid simulations gave a higher level of transport than the more exact gyrokinetic simulations of the same turbulence. This discrepancy is thought to be due to the treatment of zonal flow damping which is an important saturation mechanism for the ITG modes. For the standard parameter set used to norm the GLF23 model, the more accurate gyrokinetic simulations give a factor of about four lower ion thermal transport than the original gyrofluid simulations. Recent simulations of ETG modes have also show that these modes have a much higher level of transport than would be expected from simple scaling from ITG mode results by the square root of the electron to ion mass ratio. This is also due in part to the zonal flows. Since there are no non-linear simulations with fully kinetic electron and ion dynamics to use for fitting the model, it was decided to renormalize the model to get a best fit to data. The normalization for the ITG/TEM modes (which share the same wavenumber region) and the ETG modes were treated as independent coefficients. A set of 51 lower single null ELMing H-mode discharges from DIII-D, JET and ALCATOR C-Mod were used. The coefficients of the ITG/TEM modes and of the ETG modes were adjusted to obtain a minimum standard deviation in the predicted stored energy and a zero offset in the mean stored energy over the data set. This procedure yielded a reduction of the ITG/TEM mode coefficient by a factor of 1/3.70 and an increase in the ETG mode coefficient by a factor of 4.8 over the original model. These trends agree with the recent theory. The ITG mode renormalization is close to what would have been adopted if the model had been renormed to gyrokinetic ITG mode simulations. Note that the renormalized ETG mode fluctuation level is still smaller than the ITG mode level for the same parameters.

The impact of the renormalization of the GLF23 model is shown in Fig. 44. The predicted fusion power for the base design of ITER-FEAT as a function of pedestal temperature is shown for the original and renormed models with a flat density profile. The density was taken to be $1.0\times10^{20}/m^3$ and the plasma was assumed to be a 50% mix of deuterium and tritium diluted with carbon to a Z_{eff} of 1.69. The GLF23 model is still quite stiff even after renormalization so the improvement in energy confinement is smaller than the reduction of the local transport coefficients. The temperature profile is still close to the marginally stable profile for ITG/TEM modes. The renormalization does reduce the pedestal temperature required to reach the 400 MW design target by about 0.5 keV. There is 40 MW of negative ion neutral beam heating included in the calculations. Note that Q=fusion power/auxillary heating power is not a meaningful

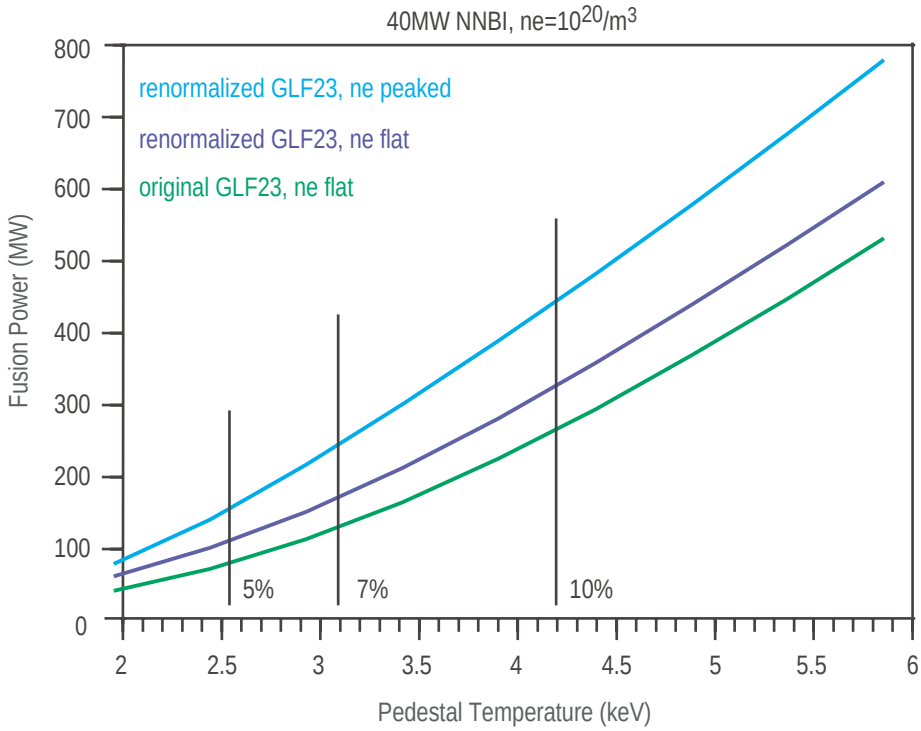

Fig. 44. Predicted fusion power for ITER-FEAT reference case as a function of pedestal temperature for different GLF23 models and different density profiles at 5.7% and 10% flux pedestal widths.

concept here since the pedestal temperature is being held fixed and not determined by the heating power. The amount of heating power needed to reach a particular pedestal temperature is unknown so the fraction of auxillary power required is also unknown.

In Fig. 44 is also shown the maximum fusion power obtained by optimizing the fueling level and evolving the density profile with GLF23. The pedestal density is the same as for the flat density case but the density obtains a peaking factor of about 1.5. The fueling due to the neutral beam was multiplied by a factor adjusted to give the maximum fusion power. Too much fueling results in a temperature collapse. Allowing the density profile to peak reduces the pedestal temperature required to get to the 400 MW fusion power target even further.

The maximum pressure computed to be stable to edge pealing-ballooning modes for various assumed pedestal widths (as a percentage of poloidal flux) are indicated by the black vertical lines in Fig. 44. In order to reach 400 MW a rather larger pedestal width of 9% is needed. This calculation of the maximum pedestal pressure is sensitive to detailed magnetic flux surface shaping and to assumptions about the density profile. The pedestal density and temperatures used in the edge stability calculation are not the same as in Fig. 44 but the pedestal pressure is the same. Tests of the predictive power of the pealing-

balloning stabilty boundary for the pedestal pressure in present tokamak experiments are in progress. The strong dependence of the predicted performance of ITER-FEAT on the pedestal pressure motivates an intensive research effort to develop a predictive theory of the pedestal pressure and width.

A scan of the density for flat density profiles is shown in Fig. 45. All cases are with the renormalized GLF23 model. The fusion power increases with the density quadratically. The empirical Greenwald density limit is $1.18\times10^{20}/m^3$. Normalizing the fusion power by the pedestal density squared gives an almost universal pedestal temperature dependence for all of these cases as shown in Fig. 46. This demonstrates the fact that the temperature profile is close to the marginal stability profile for all cases due to the stiff transport. The fusion power divided by the pedestal electron pressure squared is almost constant for these scans as shown in Fig. 47. Thus, there is little advantage to trading off density for temperature, a target fusion power will require reaching a target pedestal pressure. There is a fall off at low temperature due to the fusion reaction rate decay but over the range 3–6 keV the fusion power is proportional to the pedestal pressure squared. A scan of the fusion power for various pedestal densities for cases with the density evolved by GLF23 and the fueling adjusted to give the maximum fusion power is shown in Fig. 48. There is still roughly a pedestal pressure squared dependence for these cases but with a larger coefficient due to the density peaking as shown in Fig. 47. Some of the variation in going from low to high pedestal density is due to the shift off axis in the negative neutral beam fueling profile. Recall that this particle source was simply multiplied in finding the optimum fueling rate.

The renormalization of GLF23 and the inclusion of density peaking has considerably increased the predicted performance of ITER-FEAT over the original GLF23 model with flat density profiles. Further improvement is possible if the critical gradient for ITG/TEM modes can be increased or the turbulence otherwise suppressed. The advanced tokamak toolbox in present machines includes hot ions, strong toroidal rotation and fast ion dilution which are not applicable to ITER-FEAT. The most promising route to improved performance is current profile control to give reversed magnetic shear. This mechanism will be explored in detail in future work. Clearly more work is needed on the calculation of the pedestal pressure and width in order to improve the confidence of the predicted performance.

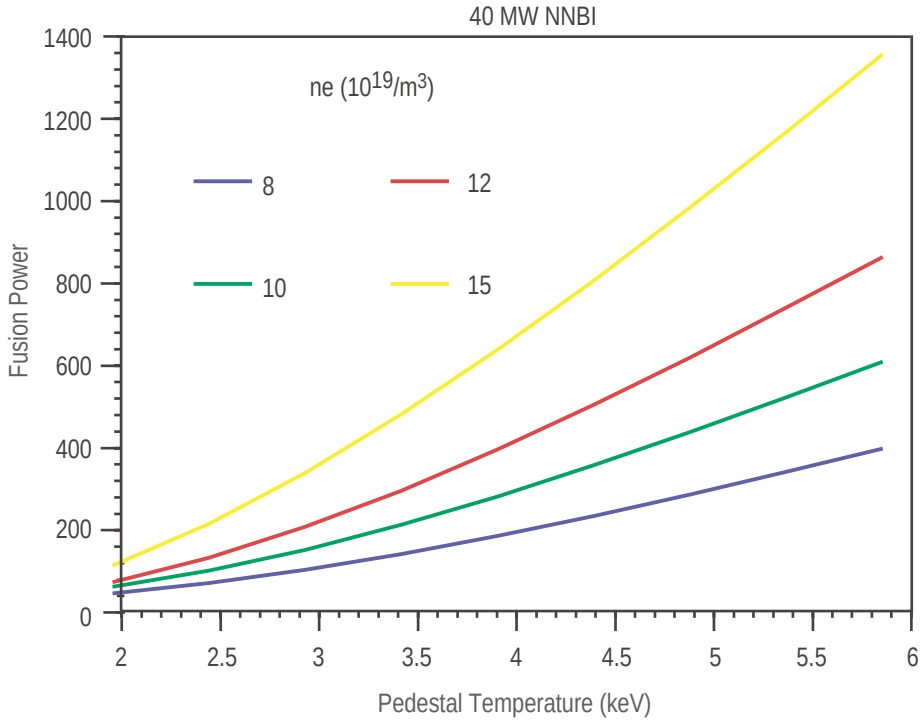

Fig. 45. Density scan of fusion power vs. pedestal temperature for flat density profile.

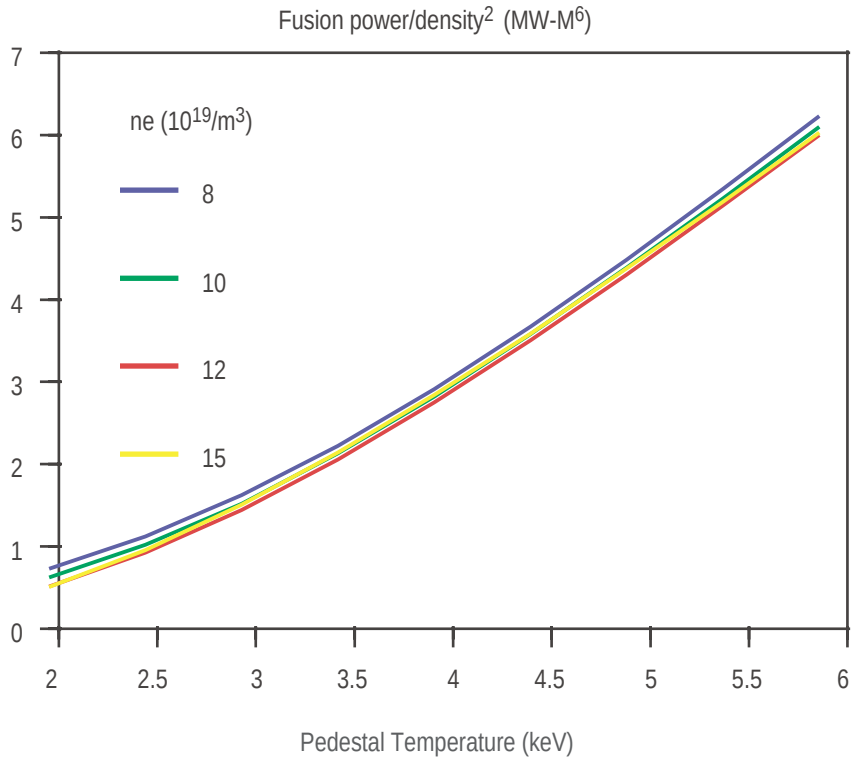

Fig. 46. Density scan of fusion power/(pedestal density)^2 shows uniform pedestal temperature dependence.

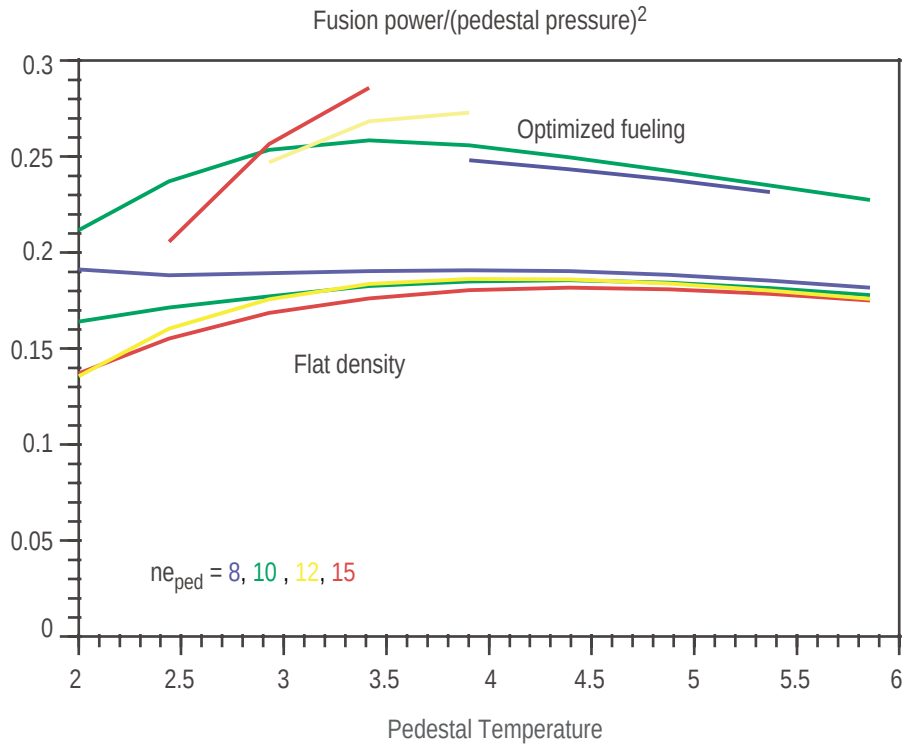

Fig. 47. Fusion power/(pedestal pressure)^2 is almost constant vs. pedestal temperature for all densities with similar profiles.

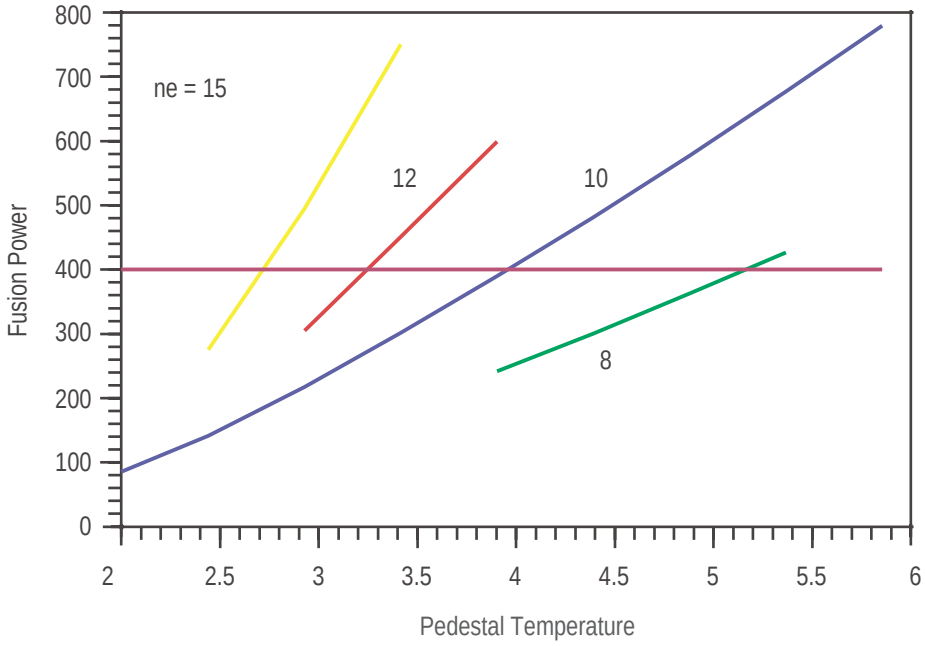

Fig. 48. Fusion power with optimized fueling.

5. EDGE AND DIVERTOR ISSUES FOR AT PLASMAS

In the following sections we investigate edge and divertor issues related to the ITER-FEAT advanced tokamak (AT) operaton. Typically, AT scenarios are characterized by high-energy confinement and significant bootstrap current, such as, for example, the AT case [19] (Table VI) examined in the following discussion. This case is characterized by a substantial bootstrap fraction (≈0.53) and β_N (≈3.17). The volume-averaged density of this AT plasma is significantly less than the nominal ITER-FEAT parameters for inductive operation (i.e., 0.78×10^{20} m^{-3} versus 1.0×10^{20} m^{-3}, respectively).

In achieving this favorable performance, the plasma density is maintained at relatively low levels compared with the reference ITER-FEAT scenarios. In turn, this may result in more concentrated power loading (with potentially more damage) at the divertor targets. In the following, we evaluate the prospects of reducing this power loading.

A significant amount of analysis has already been done on the divertor design for the reference ITER FEAT using the detached radiative divertor approach in order to reduce heat loading at the divertor targets to acceptable levels (≈5 MW/m^2). We first review reducing divertor heat loading by enhancing the radiated power inside the main plasma operating under the "AT" scenario [19]. We next look at the "radiative divertor" solution which may offer better prospects for reduced heat loading at the targets, but may also degrade some of the positive aspects of "AT" operation (e.g., high bootstrap current). Finally, we examine the problem of excessive power loading at non-divertor vessel locations, specifically the effect that the variation in the upper triangularity of an ITER-FEAT AT equilibrium has on scrape-off layer flux geometry and the resulting power loading near the top of the vacuum vessel. We surmise that the maximum triangularity for ITER FEAT AT is significantly reduced by wall power loading near the top of the vessel.

5.1. RADIATING MANTLE SOLUTION FOR AT

We first consider the prospects of reducing the power flowing into the scrape-off layer (SOL) by radiating a significant fraction of the heating power from inside the main plasma. This method is commonly referred to as a "radiating mantle" solution to excessive power loading of the divertor structure. Three recycling impurities are often considered as radiating agents: argon, krypton, or xenon. In considering a case of an ITER FEAT AT plasma described below, we assume $n_{He}/n_e = 0.04$ and $n_{Be}/n_e = 0.02$. For this study, we assume the density and temperature profiles given in Ref. [19] and we also

assume that the spatial profile of the impurity densities mirror that of the electron profile (i.e., n_{imp}/n_e is constant). We then vary the argon, krypton, and xenon concentrations to match the three Z_{eff} cases shown in Table VII.

TABLE VII
A CASE FOR Q=5 STEADY-STATE OPERATION WITH REVERSED SHEAR [19] IS DESCRIBED

R/a (m/m)	6.6.1.6
B_T (T)	4.98
I_p (MA)	7.8
$\langle n_e \rangle$ (10^{20} m^{-3})	0.78
β_N	3.17
$P_{\_} + P_{aux}$ (MW)	121
$Q = P_{fus}/P_{aux}$	5.2
Z_{eff}	1.77
I_{CD}/I_p (%)	46.4
Ibs/Ip (%)	53.6
q_{95}	4.1
HH (98y,2)	1.49

We would expect that the method of raising the level of radiated power from the core plasma by "seeding" would not be as effective in the AT cases as we found previously in the ITER-FEAT reference cases. For the (nominal) Z_{eff} =1.66 case, krypton seeding yields the highest total core radiated power (i.e., ≈21 MW). Even so, the core radiated power is still not playing a major role in the power balance in this AT case, since the ratio of the radiated power to that of the total heating power (i.e., ≈121 MW, including alpha heating power) remains less than 0.2. Doubling the fraction of the seeded impurities without changing the helium and beryllium concentrations (resulting in a $Z_{eff} \approx 2.0$) raises the radiated power fraction to at best ≈0.3 (e.g., Kr case).

5.2. UPPER BOUND ESTIMATE OF THE PEAK DIVERTOR HEAT FLUX IN AT

To estimate the peak heat flux at the outboard divertor target $Q_\perp$ (Appendix A), we assume that the heat flux profile is peaked on the separatrix target and that the radiated power from the SOL and divertor make no appreciable contribution to reducing the divertor heat flux. Of course, this estimate would set the upper limit to $Q_\perp$. Table VIII shows that, regardless of which of the three radiating impurities was used, $Q_\perp \approx$ 12–13 MW/m^2 for the nominal Z_{eff} = 1.66 case. If the seeded impurity concentration in

the core plasma is doubled, the radiated power increases but only reduces $Q_\perp$ by ≈20% to ≈10 MW/m^2, as during krypton seeding. Thus, the sensitivity of peak heat flux reduction to seeding the main plasma with impurity ions is not particularly strong for the lower AT-like main plasma densities and the range in impurity concentrations considered here. For the "steady state" AT scenario, the upper bound for peak heat flux (e.g., $Q_\perp \approx$ 10 MW/m^2 for the krypton case) may still be too high, even allowing for the likelihood of additional reductions in heat flux due to radiative processes in the divertor. Unless the impurity concentration can be raised still further (i.e., $Z_{eff} > 2$), the prospects of relying on core radiation alone appears inadequate to the AT task. However, raising the impurity concentration significantly above Z_{eff} of about 2 (in order to increase the radiating fraction) might present drawbacks of its own (e.g., reducing the bootstrap current as collisionality increases).

TABLE VIII
THE RATIO OF THE SEEDED IMPURITY TO THE ELECTRON DENSITY, THE POWER PRODUCED IN THE CORE PLASMA BY THAT SEEDED IMPURITY, THE TOTAL RADIATED POWER PRODUCED BY THE SEEDED IMPURITY PLUS SPECIFIED AMOUNTS OF HELIUM ($n_{He}/n_e \approx 0.04$) AND BERYLLIUM ($n_{Be}/n_e \approx 0.02$), AND THE RESULTING PEAK HEAT FLUX AT THE OUTBOARD DIVERTOR TARGET ARE SHOWN FOR THREE SEEDED IMPURITIES (Argon, Krypton, and Xenon) AT THREE VALUES OF Z_{eff}. THE MIDPLANE HEAT FLUX SCRAPE-OFF WIDTH IS 1.3 cm (based on estimates derived from Ref. [21]). THE FRACTION OF THE POWER FLOW TO THE OUTBOARD DIVERTOR TO THAT FLOWING TO BOTH DIVERTORS IS 0.6. THE GEOMETRY OF THE DIVERTOR ARE BASED ON FIGURES SHOWN IN REF. [22].

Z_{eff}	1.66	1.80	2.00
$P_{rad,He}$	1.2	1.2	1.2
$P_{rad,Be}$	2.7	2.7	2.7
f_{Ar}	1.1×10^{-3}	1.6×10^{-3}	2.2×10^{-3}
$P_{rad,Ar}$ (MW)	9.4	13.6	18.9
$P_{rad,total}$ (MW)	13.3	17.5	22.8
$Q_\perp$ (MW/m^2)	12.9	12.4	11.8
f_{Kr}	2.7×10^{-4}	3.8×10^{-4}	5.4×10^{-4}
$P_{rad,Kr}$ (MW)	16.7	25.4	33.4
$P_{rad,total}$ (MW)	20.6	29.3	37.3
$Q_\perp$ (MW/m^2)	12.1	11.0	10.1
f_{Xe}	5.1×10^{-5}	7.2×10^{-5}	1.0×10^{-5}
$P_{rad,Xe}$ (MW)	9.6	13.6	19.4
$P_{rad,total}$ (MW)	13.5	17.5	23.2
$Q_\perp$ (MW/m^2)	12.9	12.4	11.8

5.3. UPSTREAM DENSITY AND TEMPERATURE AT DETACHMENT FOR A SPECIFIED POWER FLOW INTO THE SOL

A detached divertor state also lowers the peak power loading at divertor targets. To date, little detailed analysis of the SOL and divertor for the ITER-FEAT AT using 2-D transport modeling has been reported. Some modeling of the ITER-FEAT using B2-EIRENE transport code seem promising for the AT version of ITER-FEAT [19]. For example, operating in the detached mode (according to published divertor modeling for a ITER-FEAT device [19]) can result in a peak heat loading in the 5–10 MW range. Operating deeper into the detached divertor mode regime can lower peak heat flux a little bit more, but at a problematic cost to "AT" features, such as degraded bootstrap current or current drive. In this analysis we estimate the separatrix density and temperature at detachment. Separate "pedestal" calculations examining the consistency of these midplane separatrix density and temperature at detachment with "AT" performance are examined in Section 3.3.

From the "Two-Point" modeling approach, we estimate the "upstream" density at the time of detachment $n_{U,DET}$ from Ref. [20]:

$$n_{U,DET} = 4.2\times10^{15}\times\frac{\left(P_{SOL}\right)^{0.71}\times\left(1-f_R\right)^{0.64}}{\left(\chi_\perp\right)^{0.36}\times\left(a\times R\right)^{0.71}} \quad , \tag{1}$$

where P_{SOL} is the power flowing into the scrape-off layer from the main plasma, L is the distance from the stagnation point to the divertor target following a magnetic field line, f_R is the fraction of radiated power in the scrape-off layer and divertor, $\chi_\perp$ is the energy diffusivity, a is the minor radius, and R is the major radius.

"Pure" 1-D analysis is likely to be inadequate due to the complexities of divertor and SOL physics. To improve things we "normalize" to existing full 2-D modeling [B2-EIRENE] on an ITER-FEAT design [21].

For the P_{SOL} = 121 MW, 2-D modeling $\Rightarrow$ $n_{U,DET} = 0.34\times10^{20}$ m^{-3}.

$$n_{U,DET}\left(m^{-3}\right) = C_1\times\left[P_{SOL}\,(MW)\right]^{0.71} \quad , \tag{2}$$

where $C_1 = \approx 1.14\times10^{20}$

Then, for each P_{SOL} value, substitute $n_{U,DET}$ into the "Two-Point" equation for $T_{U,DET}$:

$$T_{U,DET}\,(eV) = 1.7\times10^{-7}\times\left[n_{U,DET}\times L(m)\right]^{0.40} \quad . \tag{3}$$

Figure 49 shows how P_{SOL} varies with $n_{U,DET}$ and $T_{U,DET}$.

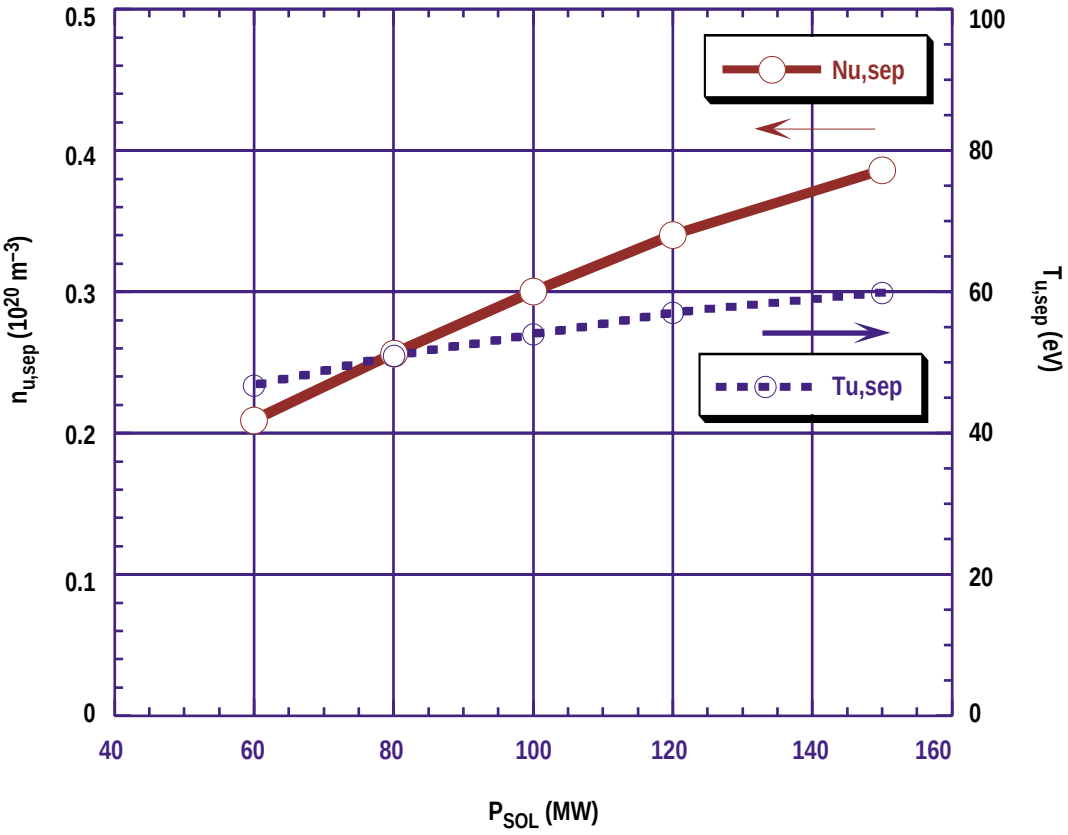

Fig. 49. Predicted upstream density and temperature at detachment are shown as a function of power flow into the scrape-off layer. These dependencies with P_{SOL} are normalized to a B2-EIRENE case for an ITER-FEAT design for the P_{SOL} = 120 MW case.

5.4. VARIATION IN HEAT FLUX TO THE TOP OF THE VESSEL AS TRIANGULARITY IS CHANGED

Two important considerations having a direct bearing on the economics of future tokamaks are adequate plasma confinement time,τ_E, for plasma ignition, and a sufficiently high volume-averaged toroidal beta, β_T, for fusion power production. Higher values of both τ_E and β_T are more readily obtained as the plasma shape becomes increasingly "triangular." Hence, it is likely that the highest performance for ITER-FEAT AT would occur by maximizing the triangularity in both upper and lower regions of the plasma. Because the ITER-FEAT AT divertor largely fixes the lower triangularity (i.e., $\langle q_{DOWN,95} \rangle \approx 0.47$ and $\langle q_{DOWN,SEP} \rangle \approx 0.63$). Any maximization of the overall triangularity (i.e., average of upper and lower plasma triangularity) must result from maximizing the upper plasma triangularity. One drawback to maximizing the triangularity of the upper plasma, however, is the likelihood that flux surfaces in the far

scrape-off layer (SOL) would be "peeled off" and intersect the wall at a non-divertor location, specifically near this less protected upper inboard wall location. To quantify this "peeling off" effect, we define the quantity dR_{sep} which is the radial distance between the upper divertor separatrix and the lower divertor separatrix, as determined at the outboard midplane.

In the following, we first estimate what the maximum upper triangularity can be without losing the "lower single-null" shape (i.e., maintain $dR_{SEP} > 0$). We then estimate the power loading "penalty" we pay in achieving this triangularity. For this study, we use more "realistic" ITER-FEAT AT equilibria, where pedestal pressure is finite (Section 1). Previous work with AT equilibria used a zero edge pressure boundary condition. Figure 50 shows two equilibria from this study for (1) "base case" triangularity (standard AT shape) and (2) high triangularity. The methodology used to evaluate the heat flux and power loading is based on the geometry of the intersection of scrape-off layer flux surfaces with the top of the vessel; the main parameters are given in the caption to Fig. 51.

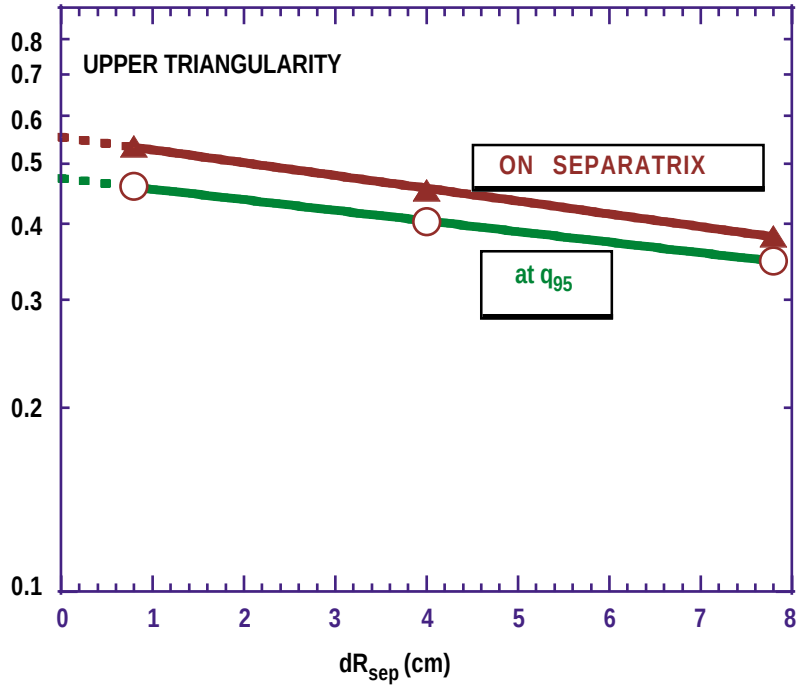

Fig. 50. The AT-equilibria for the base case (a) and for the high triangularity case (b) are shown. Both equilibria have "reverse shear" with pronounced edge pressure pedestal. The curves outside the separatrix are stacked at 1-cm intervals, as measured from the outboard midplane.

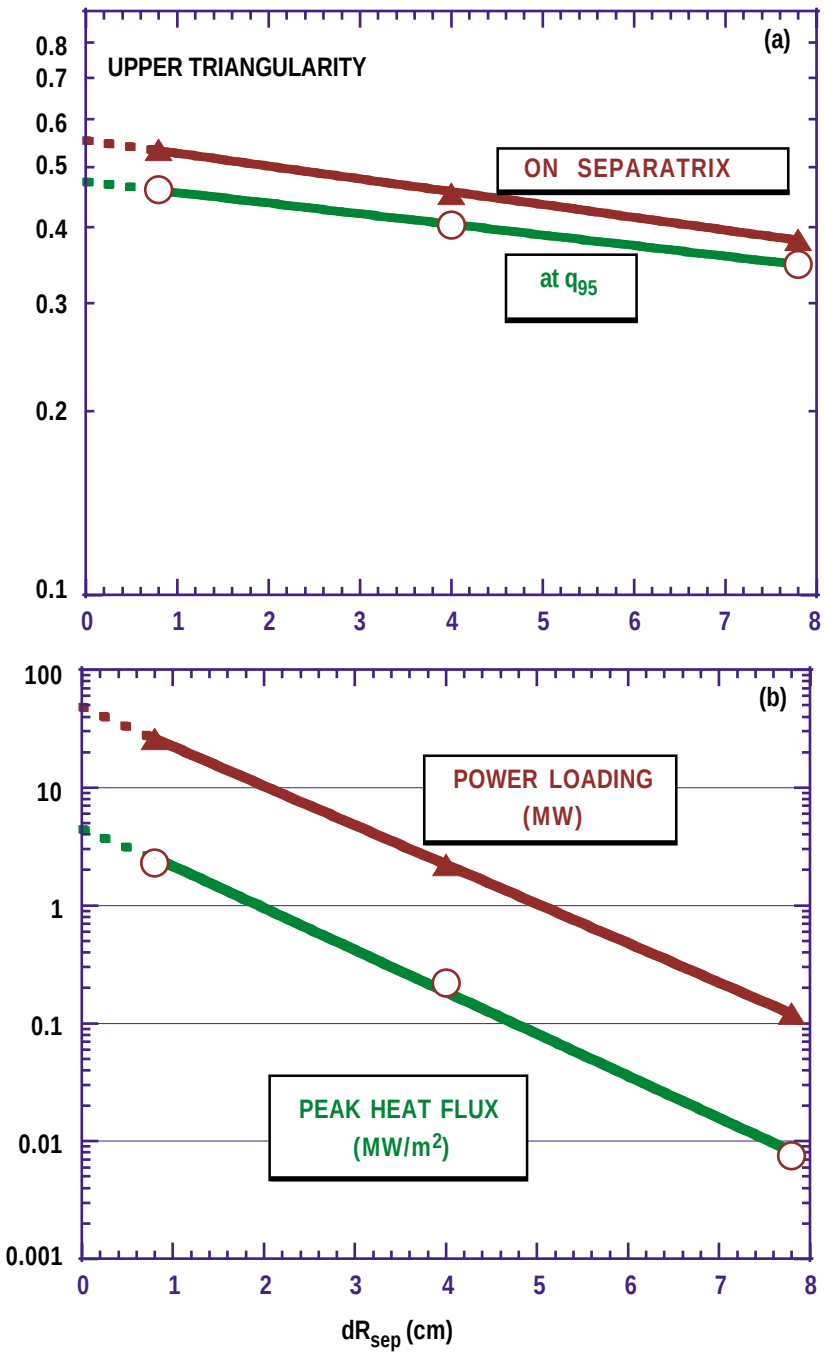

Fig. 51. (a) Upper triangularity for the q_{95} flux surface and for the separatrix are shown as a function of dR_{sep} for a ITER-FEAT AT case. The lower plasma triangularities are relatively unchanged, i.e., $\langle q_{DOWN,95}\rangle \approx 0.47$ and $\langle q_{DOWN,SEP}\rangle \approx 0.63$. (b) The peak heat flux and the total power loading at the top of the vacuum vessel are plotted versus dR_{sep}. The dashed lines are extrapolations to the double-null shape. The main parameters are: $f^{OUTBOARD/TOTAL} \approx 0.8$, $f^{GRAD\ B/TOTAL} \approx 0.5$, $f^{RAD} \approx 0.2$, $a \approx 45\text{-}60\infty$, $R^{S} \approx 4.8$ m, $f^{exp} \approx 15\text{-}20$, and $lp \approx 1.3$ cm.

5.4.1. Standard ITER-FEAT AT Equilibrium Case

The triangularity for the upper plasma on the q_{95} surface ($\delta_{UP,95}$) for the "standard" triangularity ITER-FEAT AT case was found to be 0.347; see Fig. 1(a) Direct heating of the wall near the top of the vessel (opposite the divertor) is possible if the secondary X-point lies at or inside the vessel boundary, as it does in the "base case" AT equilibrium [Fig. 1(a)]. The SOL flux surfaces for the base case show a well-defined lower single-null shape ($dR_{SEP} \approx 7.8$ cm). Hence, for this case, the peak heat flux and the total power loading on the top of the vessel are rather small, i.e., 7.5×10^{-3} MW/m^2 and 0.12 MW, respectively (Table VI).

5.4.2. Intermediate Triangularity for an ITER-FEAT AT Equilibrium Case

The triangularity $\delta_{UP,95}$ for the "intermediate triangularity" AT case was 0.402; see Fig. 1(b). The SOL flux surfaces for the intermediate case still define a lower single-null shape ($dR_{SEP} \approx 4.0$ cm). We found that for this ITER-FEAT AT case the peak particle heat flux the power loading at the top of the vessel were 0.22 MW/m^2 and ≈2.2 MW, respectively. These values can also probably be handled without much engineering difficulty.

5.4.3. High Triangularity for an ITER-FEAT AT Equilibrium Case

We found that $\delta_{UP,95}$ for the "highest triangularity" AT case was 0.459; see Fig. 1(c). The SOL flux surfaces for the base case show a near double-null shape ($dR_{SEP} \approx 0.8$ cm). We found that for this ITER-FEAT AT case the peak particle heat flux the power loading at the top of the vessel were 2.3 MW/m^2 and ≈26 MW, respectively. These values peak heat flux and power loading at the top of the vessel require thermal analysis, if the operating triangularity near $\delta_{UP,95} \approx 0.46$.

The "high" triangularity case is close to a double-null configuration. We estimate the triangularity and power loading results for a double-null ($dR_{SEP} = 0$) by extrapolating the results of the three previous cases and using an exponential fit function [i.e., Fig. 2(a,b). These results are included in Table IX.

TABLE IX
THE PEAK HEAT FLUX INCREASES WITH TRIANGULARITY

	dR_{SEP} (cm)	$\delta_{UP,SEP}$	$\delta_{UP,95}$	$Q_{\perp,TOP}$ (MW/m^2)	P_{TOP} (MW)
Base case	7.8	0.381	0.347	7.5×10^{-3}	0.12
Intermediate δ_{TRI}	4.0	0.453	0.402	0.22	2.2
High δ_{TRI}	0.8	0.534	0.459	2.3	25
Est. highest δ_{TRI}	0.0	0.55	0.47	5.3	48

5.4.4. Summary of Triangularity and Power Loading Study

We found that for the standard ITER-FEAT AT equilibria (with a pedestal edge current), the peak particle heat flux at the top of the vessel was ≤0.1 MW/m^2 and the total power flowing to the top of the vessel ≤1 MW. At an intermediate upper triangularity ($\delta_{UP,95} \approx 0.40$), roughly midway between standard $\delta_{UP,95}$ and estimated highest $\delta_{UP,95}$ for ITER-FEAT AT, power loading at the top of the vessel is still modest. These values can probably be handled without much engineering difficulty. However, at the highest triangularity case ($\delta_{UP,SEP} \approx 0.55$), the peak heat flux (and power loading) is much more problematical. The above result is consistent with previous analyses of DIII-D data, where we found that significant power can be directed to unprotected vessel wall areas if dR_{SEP} is 1–2 scrape-off widths of the parallel heat flux.

We point out that the location and flux geometry in the lower divertor were essentially unchanged as the upper triangularity was varied. It is interesting to point out that the peak heat flux at the lower outer divertor does decrease somewhat as dR_{SEP}. changes from lower single-null toward the double-null shape. In recent DIII-D magnetic balance experiments, this reduction in the peak heat flux at the lower outer divertor target was ≈30%. We believe that changes in the scrape-off properties of the parallel heat flux may be at least partially responsible for this behavior.

5.4.5. ELM-Related Concerns

Although the "AT" core energy confinement is used in ITER-FEAT, it is not clear whether the plasma "edge" region will necessarily be "H-mode" or "L-mode." If an H-mode edge forms during the evolution of the discharge or during the "steady state" phase, then ELMs (i.e., edge localized modes) are possible. If so, the resulting ELM-induced particle pulses can lead to a high rate of material erosion or related damage to the surrounding vessel. ELM pulses can spread well into the scrape-off layer, e.g., ≈4 cm in DIII-D . This would suggest that ELM-related damage can be of concern to upper vessel

integrity at higher triangularity (e.g., $dR_{SEP} < 4$ cm). Further study of this ELM issue is clearly warranted.

5.5. APPENDIX A: ESTIMATE OF THE PEAK HEAT FLUX

The peak heat flux on the divertor surfaces is estimated by assuming that the radial heat flux distribution is toroidally symmetric and has an exponential form, i.e.,

$$Q_{\mathrm{div}} = Q_{\mathrm{div},0} \times \exp\left[-\frac{\left(R - R_{\mathrm{s}}\right)}{f_{\mathrm{exp}}\, x\lambda_{\mathrm{p}}} \right] \quad ,$$

where Q_{div} is the radial heat flux distribution,$Q_{\mathrm{div},0}$ is the peak heat flux at the divertor strike point, R_{S} is the major radius of the divertor strike point, $R \geq R_{\mathrm{S}}$, λ_{p} is the midplane heat flux scrape-off length, f_{exp} is the flux expansion at the divertor target.

The total amount of power P_{div} that flows into a divertor can be written as:

$$P_{\mathrm{div}} \approx P_{\mathrm{input}} \times \left(1 - f_{\mathrm{rad}}\right) \times f_{\mathrm{outboard/total}} \times f_{\nabla \mathrm{B/total}} \times \left(1 - f_{\mathrm{pfr}}\right) \ ,$$

where P_{input} is the total input power, f_{rad} is the ratio of total radiated power to total input power, $f_{\mathrm{outboard/total}}$ is the ratio of power flowing into the outboard SOL to the power flowing into both inboard and outboard SOL,$f_{\nabla \mathrm{B/total}}$ is the ratio of power striking the outboard divertor in the ∇B direction to the power striking both upper and lower outboard divertors, f_{pfr} is the fraction of power flowing into the private flux region.

We can then write $Q_{\mathrm{div},0}$ as:

$$Q_{\mathrm{div},0} = \frac{P_{\mathrm{input}} \times \left(1 - f_{\mathrm{rad}}\right) \times f_{\mathrm{outboard/total}} \times f_{\nabla \mathrm{B/total}} \times \left(1 - f_{\mathrm{pfr}}\right) \times \sin(\alpha)}{2\pi \times R_{\mathrm{s}} \times f_{\mathrm{exp}} \times \lambda_{\mathrm{p}} \times \left(1 + \dfrac{f_{\mathrm{exp}} \times \lambda_{\mathrm{p}}}{R_{\mathrm{s}}}\right)} \quad ,$$

where α is the angle between the divertor incline and the separatrix.

REFERENCES

[1] J. Leuer, "ITER-FEAT Reference Equilibrium and Global Energy Balance Analysis," Engineering Physics Memo: D3DJAL001220a, December 21, 2000.

[2] V.S. Chan, et al., "ITER-FEAT Physics Study Interim Report," CY00 IR&D Project 4437, GA-D23609, April 2001.

[3] D.J. Campbell, "The Physics of ITER-FEAT," presented at the 42nd APS Division of Plasma Physics, Quebec City, Canada, October 23–27, 2000.

[4] Y. Gribov, "ITER Equilibrium Parameters — Scenario 4: AT Configuration at Burn," Personal communication, (Excel Spreadsheet: Scen.4=one_equilb._at_burn.xls), December 5, 2000.

[5] L.L. Lao, et al., "Rotational and Magnetic Shear Stabilization of Magnetohydrodynamic Modes and Turbulence in DIII-D High Performance Discharges," Phys. Plasmas **3**, (1996).

[6] ITER, "ITER-EDA Design Description Document, Poloidal Field Control WBS 4.7," Appendix D: Dynamic Simulation of Plasma Scenarios. June 12, 1998.

[7] D.A. Humphreys, A.G. Kellman, "Analytic Modeling of Axisymmetric Disruption Halo Currents," Phys. Plasmas **6**, 2742 (1999).

[8] D.A. Humphreys, and D.G. Whyte, "Classical Resistivity in a Post-Thermal Quench Disrupting Plasma," Phys. Plasmas **7**, 4057 (2000).

[9] Engineering Physics Memo EPM010918b, ITER WRS Equilibrium with DIII-D AT Profiles, September 18, 2001.

[10] ITER-FEAT Final Design Document 2001.

[11] D.A. Humphreys, A.G. Kellman, R.S. Granetz, R.R. Khayrutdinov, V.E. Lukash, Y. Neyatani, R. Yoshino, "Analytic Halo Current Models Applied to Disruptions in Present and Next-Generation Tokamaks," Bull. Am. Phys. Soc. **43**, 1875 (1998).

[12] ITER Final Design Report 1998.

[13] P.L. Taylor, A.G.Kellman, T.E. Evans, D.S. Gray, D.A. Humphreys, A.W. Hyatt, T.C. Jernigan, R.L. Lee, J.A. Leuer, S.C. Luckhardt, P.B. Parks, M.J. Schaffer, D.G. Whyte, and J. Zhang, "Disruption Mitigation Studies in DIII-D," Phys. Plasmas **6**, 1872 (1999).

[14] D. Campbell, "The Physics of ITER-FEAT," Bull. Am. Phys. Soc. **45**, 285 (2000).

[15] P.B. Snyder, H.R. Wilson, J.R. Ferron, et al., "Edge Localized Modes and the Pedestal: A Model Based on Coupled Peeling-Ballooning Modes," to be published in Phys. Plasmas (May 2002).

[16] H.R. Wilson, P.B. Snyder, G.T.A. Huysmans, and R.L. Miller, "Numerical Studies of Edge Localised Instabilities in Tokamaks," submitted to Phys. Plasmas (2001).

[17] M.S. Chu, private communication,11/28/01, see Section 3.4

[18] J.A. Leuer, L.L. Lao, DIII-D Engineering Physics Memo, D3DJAL010918b, October 5, 2001.

[19] Technical Basis for the ITER-FEAT Outline Design (G A0 RI 2 00-01-18 R1-0), Section I.2, page 29.

[20] P.C. Stangeby, "The Plasma Boundary of Magnetic Fusion Devices," Institute of Physics Publishing (2000).

[21] A. Loarte, S. Bosch, A. Chankin, et al., J. Nucl. Mater. **266-269**, 587 (1999).

[22] D.J. Campbell and members of the ITER Joint Central Team and Home Teams, "The Physics of ITER FEAT," presented at the 42nd APS-DPP/ICPP-2000, Quebec City, October 23–27, 2000.